


<b>Title</b>	Design, fabrication and characterization of resonant waveguide grating based optical biosensors
<b>Author(s)</b>	Hossain, Md Nazmul
<b>Publication date</b>	2015
<b>Original citation</b>	Hossain, M.N, 2015. Design, fabrication and characterization of resonant waveguide grating based optical biosensors. PhD Thesis, University College Cork.
<b>Type of publication</b>	Doctoral thesis
<b>Rights</b>	© 2015, Md N. Hossain. <a href="http://creativecommons.org/licenses/by-nc-nd/3.0/">http://creativecommons.org/licenses/by-nc-nd/3.0/</a> 
<b>Embargo information</b>	No embargo required
<b>Item downloaded from</b>	<a href="http://hdl.handle.net/10468/2489">http://hdl.handle.net/10468/2489</a>

Downloaded on 2017-02-12T06:47:34Z



**UCC**

University College Cork, Ireland  
Coláiste na hOllscoile Corcaigh

# **Design, Fabrication and Characterization of Resonant Waveguide Grating based Optical Biosensors**

by  
**Md Nazmul Hossain**

Thesis Submitted to  
The National University of Ireland, Cork



for the degree of  
**Doctor of Philosophy**



Tyndall National Institute  
The Department of Electrical and Electronics Engineering  
University College Cork  
**July 2015**

Supervisors: Dr. Brian Corbett  
Prof. Peter Parbrook  
Head of Department/School: Prof. Nabeel A. Riza

I, Md Nazmul Hossain, certify that this thesis is my own work and I have not obtained a degree in this university or elsewhere on the basis of the work submitted in this thesis.

---

*Md Nazmul Hossain*

To all my well-wishers and loved ones

## Acknowledgements

First and foremost, I would like to thank my supervisor, Dr. Brian Corbett, for providing me with endless support, encouragement and mentoring. I could not possibly have asked for a more amiable and enthusiastic supervisor. I look forward to have that fantastic support from him in the next stage of my career outside the Tyndall National Institute to bring forth more exciting collaborative research works.

I must also thank my co-supervisor, Dr. Peter Parbrook, for providing me helpful feedback and aiding me interfacing with the university.

I would like to thank Tyndall National Institute as a whole for providing and maintaining the lab facilities in which this research work was conducted, and I would like to thank European Union for funding this research by EU FP7-ICT PHAST-ID project under grant agreement 258238 and also Science Foundation Ireland for funding this research under the IPIC project (12/RC/2276).

Among my colleagues, I would like to thank John Justice for helping me getting trained on the instruments necessary for my research and providing me with helpful information in all aspect of my work.

I would also like to thank the various current and former members of my group, III-V materials and devices group and of Tyndall National Institute for providing me assistance, encouragement and advice. I could not but mention few names from the long list. Thanks Brendan Rycroft, Pleun Maaskant, Donagh O'Mahony, Farzan Gity, Mahbub Akhter, Umar Khan, Muhammad Sadiq, James O'Callaghan, Alan O'Riordan, Pierre Lovera, Micki Mitchell and many more. I also can not ignore the huge support from my Postgraduate room mates: Shahab Norouzian, Niall O Cuilleainain, Rosemary O'Keeffe, Daniel Jones, Carola Schopf and many others.

I also like to take this opportunity to thank Prof. Michael Turner, Pompei Hazarika and Marion Wrackmeyer from Manchester University (UK), Karppinen Mikko and Petäjä Jarno from VTT (Finland), and Klaus Wiehler from Sierra Sensors (Germany) and acknowledge their corresponding contributions in this research work.

Finally, many thanks go to my family specially my mother, wife and sisters for raising me up with so much love and care and providing me the purpose and encouragement to reach this stage of my career.

## Abstracts

The absence of rapid, low cost and highly sensitive biodetection platform has hindered the implementation of next generation cheap and early stage clinical or home based point-of-care diagnostics. Label-free optical biosensing with high sensitivity, throughput, compactness, and low cost, plays an important role to resolve these diagnostic challenges and pushes the detection limit down to single molecule. Optical nanostructures, specifically the resonant waveguide grating (RWG) and nano-ribbon cavity based bio-detection are promising in this context.

The main element of this dissertation is design, fabrication and characterization of RWG sensors for different spectral regions (e.g. visible, near infrared) for use in label-free optical biosensing and also to explore different RWG parameters to maximize sensitivity and increase detection accuracy. Design and fabrication of the waveguide embedded resonant nano-cavity are also studied. Multi-parametric analyses were done using customized optical simulator to understand the operational principle of these sensors and more important the relationship between the physical design parameters and sensor sensitivities.

Silicon nitride ( $\text{Si}_x\text{N}_y$ ) is a useful waveguide material because of its wide transparency across the whole infrared, visible and part of UV spectrum, and comparatively higher refractive index than glass substrate.  $\text{Si}_x\text{N}_y$  based RWGs on glass substrate are designed and fabricated applying both electron beam lithography and low cost nano-imprint lithography techniques. A Chromium hard mask aided nano-fabrication technique is developed for making very high aspect ratio optical nano-structure on glass substrate. An aspect ratio of 10 for very narrow (~60 nm wide) grating lines is achieved which is the highest presented so far. The fabricated RWG sensors are characterized for both bulk (183.3 nm/RIU) and surface sensitivity (0.21nm/nm-layer), and then used for successful detection of Immunoglobulin-G (IgG) antibodies and antigen (~1 $\mu\text{g/ml}$ ) both in buffer and serum.

Widely used optical biosensors like surface plasmon resonance and optical microcavities are limited in the separation of bulk response from the surface binding events which is crucial for ultralow biosensing application with thermal or other perturbations. A RWG

based dual resonance approach is proposed and verified by controlled experiments for separating the response of bulk and surface sensitivity. The dual resonance approach gives sensitivity ratio of 9.4 whereas the competitive polarization based approach can offer only 2.5. The improved performance of the dual resonance approach would help reducing probability of false reading in precise bio-assay experiments where thermal variations are probable like portable diagnostics.



# Table of contents

Acknowledgements.....	iv
Abstracts .....	vi
Table of contents.....	viii
List of Figures.....	xii
List of symbols .....	xxi
Abbreviations.....	xxiv
<b>1 INTRODUCTION TO OPTICAL BIOSENSOR .....</b>	<b>1</b>
1.1 Optical Biosensors .....	2
1.2 Refractive Index based Label-free Optical Biosensing .....	3
1.2.1 Surface Plasmon Resonance (SPR) based Sensors.....	4
1.2.2 Resonant Waveguide Grating based Sensing .....	7
1.2.3 Photonic Crystal Cavity Biosensors .....	8
1.2.4 Whispering Gallery Mode (WGM) based Resonant Optical Microcavity .....	11
1.3 Commercialization of Optical Biosensors .....	12
1.4 Motivation of this Thesis Work.....	14
1.5 Outline of the Thesis.....	16
References.....	18
<b>2 DESIGN OF RESONANT WAVEGUIDE GRATING BASED SENSOR.....</b>	<b>24</b>
2.1 Introduction.....	25
2.1.1 Historical Background of RWG .....	25
2.2 Physical Basis of RWG Reflectance spectra .....	27
2.3 Numerical Model for Design and Analysis .....	29
2.3.1 Solver Physics .....	29
2.4 RWG Simulation using FDTD .....	31
2.4.1 Multi-order multimode RWG.....	33
2.5 RWG Design Procedure .....	35
2.5.1 Role of FF and $h_{\text{etch}}$ on RWG Spectral Linewidth.....	37

2.5.2 Parameters of the Optimized RWG .....	38
2.6 Sensor Sensitivity .....	40
2.6.1 Bulk Sensitivity .....	40
2.6.2 Surface Sensitivity .....	42
2.7 Conclusions.....	45
Reference .....	47
<b>3 FABRICATION OF OPTICAL NANO-STRUCTURE .....</b>	<b>49</b>
3.1 Introduction.....	50
3.1.1 Photolithography .....	51
3.1.2 Focused ion beam lithography (FIB).....	52
3.1.3 Electron beam lithography.....	53
3.1.4 Nano-imprint lithography .....	54
3.2 Fabrication schemes to make the sensor chips .....	57
3.2.1 Flow chart and schematic of the nano-fabrication process steps.....	58
3.3 Development of $\text{Si}_x\text{N}_y$ Material.....	59
3.3.1 $\text{Si}_x\text{N}_y$ deposition techniques.....	60
3.3.2 Silicon-dioxide as an optical isolation.....	60
3.3.3 LPCVD $\text{Si}_x\text{N}_y$ .....	61
3.3.4 PECVD $\text{Si}_x\text{N}_y$ .....	62
3.3.5 Deposition.....	62
3.3.6 Waveguide loss characterization .....	64
3.3.7 Surface roughness measurement .....	67
3.3.8 Refractive index measurement .....	68
3.4 EBL patterning processes .....	69
3.4.1 Cr on top acting as both the charge dissipating layer during EBL and hard mask for successive etching .....	70
3.4.2 Sample preparation and EBL Process steps.....	70
3.5 Nano-imprint patterning process steps .....	72
3.6 Chrome etching process development by Inductively Coupled Plasma (ICP).....	75
3.6.1 Loading effect.....	78
3.7 Pattern transfer .....	79
3.7.1 Sidewall quality .....	81

3.8	Alignment mark and dicing .....	82
3.9	High aspect ratio nanostructure .....	85
3.10	Summary.....	86
	References.....	88
<b>4</b>	<b>BIO-CHARACTERIZATION OF RWG SENSOR .....</b>	<b>92</b>
4.1	Introduction.....	93
4.2	Characterization setup.....	94
4.2.1	Fiber based Characterization.....	94
4.2.2	Bio-characterization Setup.....	95
4.3	Characterization of RWG sensor .....	96
4.3.1	Bulk sensitivity .....	96
4.4	Surface Sensitivity .....	97
4.4.1	Bio-assay experiment.....	97
4.5	Summary .....	101
	References.....	104
<b>5</b>	<b>DUAL RESONANCE APPROACH FOR BETTER SENSING .....</b>	<b>105</b>
5.1	Introduction.....	106
5.2	Design .....	108
5.2.1	Dual resonance RWG .....	108
5.3	Fabrication of dual resonance RWG.....	111
5.4	Decoupling bulk and surface contribution.....	111
5.4.1	Controlled experiment .....	113
5.4.2	Comparison with the polarization based approach .....	115
5.5	Summary.....	116
	References.....	117
<b>6</b>	<b>RESONANT NANO-RIBBON CAVITY .....</b>	<b>119</b>
6.1	Introduction.....	120
6.2	Design of the nano-ribbon cavity .....	120
6.2.1	Calculation of the Quality factor (Q).....	124
6.2.2	Effect of Bragg mirror strength on Q-factor.....	125

6.2.3 Effect of cavity length on the Q-factor.....	126
6.2.4 Effect of $L_c$ on Q-factor .....	127
6.2.5 Bulk and surface sensitivity of the designed nano-ribbon cavity .....	130
6.3 Design of the Grating coupler.....	131
6.4 Fabrication of Nano-ribbon cavity and grating couplers .....	135
6.4.1 Investigation of the pattern transfer during the nano-imprint steps.....	136
6.4.2 Pattern transfer from nano-imprinted resist to $Si_xN_y$ .....	139
6.5 Summary.....	141
References.....	142
<b>7 CONCLUSIONS AND FURTHER DEVELOPMENT.....</b>	<b>144</b>
7.1 Summary and Conclusions .....	145
7.2 Future work and directions .....	148
7.2.1 Smartphone based Bio-detection .....	148
<b>PUBLICATIONS .....</b>	<b>151</b>

## List of Figures

Figure 1.2-1 Schematic of operational principle of prism coupled SPR based bio-sensing technique. The receptor antibody is coupled to the surface of the gold layer. The incident light is directed by the prism. The reflection spectrum shows notch which represent the Plasmon resonance wavelength. When the target molecule binds to the immobilized receptors the resonance wavelength shifts. ....	4
Figure 1.2-2 Schematic drawing of the RWG sensor showing the operational principle of surface bound bio-molecular sensing for both TE and TM polarized light. The wavelength of the resonance notch in the transmission spectrum shifts because of the surface attachment of the bio-molecules. ....	7
Figure 1.2-3 PhC (2D) biosensor with point defect made by increasing the size of the central hole and then removing the first layer of surrounding holes demonstrated by Lee and Fauchet et al [26]. Light is injected to the cavity by integrated optical waveguide...	9
Figure 1.2-4 Schematic 3D illustration of 1D PhC sensors (a) PhC cavity embedded into the feeding waveguide with grating coupler in both ends for in and out coupling of light (Chapter 6), (b) PhC cavity section is placed separately adjacent to the bus waveguide [55]. ....	10
Figure 1.2-5 (a) Schematically presented biomolecular binding event on a ring resonator and corresponding resonance wavelength shift in the transmission spectrum, (b) SEM image of the SOI micro-ring resonator seen through an annular opening of polymeric cladding. Image adapted from ref. [62], (c) a microsphere of diameter $d \approx 80 \mu\text{m}$ is melted from an optical fiber used for monitoring single-molecule nucleic acid interactions, and (d) Silica microtoroid optical resonator of $80 \mu\text{m}$ diameter fabricated on a silicon wafer using planar lithography and reflowed using a CO <sub>2</sub> laser. Figure c&d are adapted from ref. [63]&[64] respectively. ....	11

Figure 2.1-1 Diffraction spectra (of a continuous light source) by metallic grating at ten different angles obtained by Wood [1]. The wavelengths are indicated at the top of the figure in  $\times 10$  nm unit, and the angles of incidence at the left. .... 26

Figure 2.2-1 Basic single layer waveguide grating (a) Low spatial frequency grating where both zero<sup>th</sup> and higher order diffracted light is present, and (b) High spatial frequency grating where only zero<sup>th</sup> order diffracted light sustains and rest of the orders are evanescent. .... 28

Figure 2.4-1 RWG simulation setup in the FDTD graphical user interface. The larger orange rectangle is the simulation window (for unit cell of RWG) with PML in top and bottom, and periodic boundary condition at left and right side. The Si<sub>x</sub>N<sub>y</sub> grating on glass substrate is set to be covered with buffer solution in the simulation. TE polarized planewave light source is applied from top of the grating and two monitors are at the top and bottom for calculating the RWG reflection and transmission spectra respectively. 31

Figure 2.4-2 Reflection and transmission spectra of a single layer RWG for both TE and TM polarization..... 32

Figure 2.4-3 Model of the device under study denoting thicknesses of the waveguide layer ( $h_{\text{wav}}$ ) and refractive indices ( $n$ ) of the various regions as well as the period ( $\Lambda$ ) of the grating. .... 33

Figure 2.4-4 Calculated transmission spectra of the RWG with different waveguide layer thickness,  $h_{\text{wav}} = 400, 600, 1000$  nm which excites 2, 3 and 4 resonance modes respectively. .... 34

Figure 2.5-1 Flow-chart schematically shows the design procedure of the RWG targeting specific resonance wavelength, linewidth and sensitivity. .... 36

Figure 2.5-2 Transmittance of the RWG for (a) Varying filling fraction (FF), and (b) Etching depth ( $h_{\text{etch}}$ ). .... 38

Figure 2.5-3 Transmittance of visible RWG with parameters listed in Table 2.5-1, shows dual resonances. Simulation of the electric field at the resonance wavelengths (left: 633 nm, and right: 760 nm) of the RWG sensor are presented.....	39
Figure 2.6-1 Bulk sensitivity mapping using simulations. The refractive index of the medium ( $n_c$ ) on top of RWG is varied and the corresponding resonance transmittance spectra are mapped.....	41
Figure 2.6-2 Electric field distribution of the resonant mode of the RWG with marked biomolecular detection region.....	43
Figure 2.6-3 Transmittance spectra of the optimized RWG at different stages of the bio-molecular detection. The E-field distribution of the resonant mode is presented inset. .	45
Figure 3.2-1 Flow chart of the nano-fabrication process steps. ....	58
Figure 3.2-2 The starting quartz wafer has Cr deposited on $Si_xN_y$ (a) ebeam/ nanoimprint resist is spun on (b) EBL pattern is written in resist, (c) pattern is transferred to the Cr layer by ICP dry etching, (d) removal of the resist, € transfer of the pattern into the $Si_xN_y$ layer by ICP dry etching and (f) removal of the Cr. ....	59
Figure 3.3-1 Leakage of optical mode to the Si substrate while propagating. Electric field distribution of the propagating mode optically isolated by $SiO_2$ layer of thickness (a) 300 nm, and (b) $2\mu m$ . Decay of the $ E $ field along the dashed line (center of the waveguide) for $SiO_2$ thickness of (a) 300 nm, and (b) $2\mu m$ . ....	61
Figure 3.3-2 PECVD system at the Tyndall's III-V cleanroom.....	62
Figure 3.3-3 Setup for estimation of $Si_xN_y$ film optical loss. ....	64
Figure 3.3-4 Propagation length of $Si_xN_y$ thin film waveguide deposited by (a) Mixed Frequency PECVD, (b) single frequency PECVD, and (c) LPCVD. ....	65
Figure 3.3-5 The guided light (Figure 3.3-4a&b) decays exponentially at different rate for mixed and single frequency PECVD $Si_xN_y$ films. ....	66

Figure 3.3-6 Surface roughness measurements by AFM (a) RMS roughness = 3 nm for PECVD (Mixed Frequency), (b) 0.5 nm for single frequency PECVD and (c) 0.3 nm for LPCVD Si <sub>3</sub> N <sub>4</sub> depositions. ....	67
Figure 3.3-7 Ellipsometer used to characterize optical properties of the developed Si <sub>x</sub> N <sub>y</sub> film. ....	68
Figure 3.3-8 Measured refractive index of PECVD Si <sub>x</sub> N <sub>y</sub> . ....	69
Figure 3.4-1 Full wafer ebeam pattern consisting of 33 sensor chips of 1.5cm by 1cm size on a 100mm diameter wafer. Each chip has four RWG sensor of size 500μm × 500μm. ....	71
Figure 3.4-2 SEM image of stitching error during EBL writing. ....	72
Figure 3.5-1 Basic process scheme of the used UV-based nanoimprint lithography (drawing by Micro Resist Technology GmbH). Note: Mould means the same as stamp, which is the word used in this report (elsewhere also ‘template’ used sometimes), and polymer means the nano-imprint resist here. ....	73
Figure 3.5-2 Procedure to make intermediate stamps from the master stamp (drawing by Micro Resist Technology). ....	74
Figure 3.5-3 Photographs of nano-imprinted resist layers patterned with the RWG on 4” wafers: left) Resist patterned on glass wafer that have Si <sub>x</sub> N <sub>y</sub> and Cr layers; right) Resist patterned on bare Si wafer. ....	75
Figure 3.6-1 Cr/ZEP resist etch selectivity due to variation in (a) chamber pressure, (b) platen power, (c) oxygen concentration ratio (O <sub>2</sub> /(O <sub>2</sub> +Cl <sub>2</sub> )) and (d) coil power. ....	77
Figure 3.6-2 SEM images of the Si <sub>x</sub> N <sub>y</sub> nano-grating after Cr and Si <sub>x</sub> N <sub>y</sub> etching: (a) Cr etched for 1 min, (b) & (c) Cr etched for 2 min but dot-shaped residues remain at the edge of the nano-grating and (d) cleaner edge of the nano-grating when Cr is etched for 3 min. ....	79



Figure 3.7-1 Snapshot of the processed full wafer after SixNy etching. ....	81
Figure 3.7-2 Cross-sectional image of the RWG sensor for sloped sidewall angle measurement. ....	82
Figure 3.8-1 Detail of the final sensor chip (1.5cm × 1cm) with alignment marks. ....	83
Figure 3.8-2 SEM image of the fabricated RWG sensor shows period of 430 nm and filling fraction of (250/430) = 58.1%. ....	84
Figure 3.9-1 SEM images of the fabricated high aspect ratio nanostructures in Si <sub>x</sub> N <sub>y</sub> on glass substrates: ~60 nm wide (surface measurement - s) and 675 ± 5 nm deep (cross-sectional measurement - cs) grating line with (a) 1.1 μm spacing and (b) 490 nm spacing. ....	86
Figure 4.2-1 Characterization setup in reflection mode uses a bifurcated fiber to get the broadband light in and reflected light (from RWG) out. Fiber tip is aligned to the RWG sensor hold by the microfluidic chamber. Reflected light is analysed by the portable ‘Ocean Optics’ spectrometer. ....	94
Figure 4.2-2 Schematic representation of the transmission spectrum measurement setup with high resolution spectrometer for RWG sensor based biodetection. ....	95
Figure 4.3-1 Transmission spectrum of the RWG sensor for different sensing liquids to measure the bulk sensitivity. ....	96
Figure 4.4-1 Transmittance spectra of the modeled (considering fabricated parameters) RWG sensor for bio-molecular attachment. Simulation shows that 20 nm thin conformal layer of biomolecule added on the sensor surface shifts the resonance wavelength 1.8 nm. ....	97
Figure 4.4-2 Contact angle measurement of the fabricated (by Nano-imprint) RWG sensor ready for bio-assay experiment. ....	98

Figure 4.4-3 Adsorption based bio-assay experiment with RWG sensor. 1.3 nm of resonance wavelength shift was observed for 4 $\mu$ g/ml of C1q antigen immobilization. . 99

Figure 4.4-4 EDC coupled bio-assay experiment showed a total of 0.7 nm (0.5 nm for Ab and 0.2 nm for Ag) of resonance wavelength shift for 7 $\mu$ g/ml and 1 $\mu$ g/ml of C3 antibody and antigen attachment respectively. There was no shift for C1q incubation which showed the selectivity of the sensor. .... 101

Figure 5.1-1 Schematic of a RWG sensor system. The collimated beam from a broadband source is incident on the sensor at normal incidence. The reflected spectral response is monitored in real time with an optical spectrum analyzer. As binding events occur at the sensor surface, the resonance peak shift is tracked. .... 107

Figure 5.2-1 Transmission spectra map showing the resonance wavelengths (blue colored regions shows resonance dips) for different etch depths. Inset shows the transmission spectrum for an etching depth of 190nm..... 109

Figure 5.2-2 E-field distribution of PhC unit cell with an etching depth of 190 nm resonating at wavelengths ( $\lambda$ ) of 619 nm and 736 nm. .... 111

Figure 5.4-1 Schematic of the PhC biosensor where  $\Lambda$  = period of the grating,  $h_{\text{etch}}$  = etching depth,  $h_{\text{wav}}$  = Si<sub>3</sub>N<sub>4</sub> waveguide layer thickness. The buffer solution on top contains the bioanalytes. (The antibody-antigen complexes shown in the schematic are not at the same scale as the grating ..... 112

Figure 5.4-2 Map of the transmission spectrum of the PhC sensor for (a) different added layer thickness,  $\Delta d$  and (b) RI of bulk medium,  $n$ . .... 113

Figure 5.4-3 Resonance wavelengths shift when the bulk solution is changed from DI water to IPA along with a thin added layer (16 nm) on the sensor surface. Inset shows the SEM image of the sensor grating. .... 114

Figure 6.2-1 Schematic of nano-ribbon PhC cavity with in and out-coupling grating at two sides (a) 1-D PhC cavity with Bragg mirrors at both ends, (b) PhC cavity integrated with

tapered waveguide and coupling grating, and (c) grating coupler with tapered waveguide. .....	121
Figure 6.2-2 Schematic of the simulation setup of the nano-ribbon cavity with Bragg mirror at two sides and linearly tapered line of air holes placed face to face in the cavity. In simulations, a waveguide mode is injected from left end and a monitor is placed at the right side to measure the transmissivity. Three point monitors are included at the cavity section to measure the decay rate of the resonant mode for calculating the Q-factor. .	122
Figure 6.2-3 Transverse E-field distribution (fundamental mode) of the nano-ribbon waveguide sitting on glass (AF32) substrate. The height (h) and width (w) of the Si <sub>x</sub> N <sub>y</sub> waveguide are 400 nm and 300 nm respectively. The waveguide is considered to be submerged in water for biosensing application.....	123
Figure 6.2-4 Transmission spectra of the resonant nano-ribbon waveguide for different number (N) of air holes in the Bragg mirror. At resonance the transmissivity decreases with the increase in air hole number. ....	125
Figure 6.2-5 Q-factor and transmissivity vs number of air holes (N) in Bragg mirror. Q-factor increases but the transmissivity decreases with increase in Bragg mirror strength. .....	126
Figure 6.2-6 Resonance spectra of the nano-ribbon cavity for different number of air holes in the tapered mirror (N <sub>t</sub> ) inside the cavity. The Q-factor increases with cavity length ( $\propto$ N <sub>t</sub> )......	127
Figure 6.2-7 Quality factor as a function of the central separation length L <sub>c</sub> for the nano-ribbon cavity characterized by the period = 260 nm, hole diameter = 220 nm (max) ~ 130 nm (min)......	128
Figure 6.2-8 Transmission spectrum of the designed PhC nano-ribbon cavity with N = 17, N <sub>t</sub> = 7 and L <sub>c</sub> = 150 nm. ....	129

Figure 6.2-9 (a) Refractive index distribution of the tapered nano-ribbon cavity, (b) E-field distribution obtained from FDTD simulation, and (c) E-field value along the dashed line in (b). ..... 130

Figure 6.2-10 Shift in resonance wavelength (a) when the background changes from buffer solution (RI=1.33) to isopropanol (RI=1.378). Resonant shift of about 8nm corresponds to bulk sensitivity of 175 nm/RIU, (b) when 20 nm thin layer of bio-molecule (RI=1.45) is attached on the surface. .... 131

Figure 6.3-1 Schematic of the coupling scheme from fiber to the waveguide based on grating principle. .... 132

Figure 6.3-2 FDTD simulation setup for the grating coupler design. .... 133

Figure 6.3-3 Schematic of the  $\text{Si}_x\text{N}_y$  grating coupler on glass wafer where  $\Lambda$  denotes the period,  $h_{\text{waveguide}}$  is the  $\text{Si}_x\text{N}_y$  waveguide thickness, and  $h_{\text{etch}}$  is the etching depth of the grating. .... 133

Figure 6.3-4 Optimized grating coupler's (Table 6.3-1) coupling efficiency vs wavelength for both TE and TM polarized light. .... 135

Figure 6.4-1 Schematic of the nano-ribbon cavity with in and out grating coupler. .... 136

Figure 6.4-2 SEM images of nano-ribbon cavity on a) *master* stamp, b) intermediate stamp and c) patterned resist..... 137

Figure 6.4-3 SEM image of the holes in the nano-ribbon cavity from *master* stamp: (a) top view and (b) tilted side view. The targeted diameter was ~220 nm. .... 137

Figure 6.4-4 SEM images from the coupling grating. Upper image is taken from the top and lower one is the FIB milled cross section..... 138

Figure 6.4-5 SEM pictures of the FIB milled cross sections of the *master* (below) and *Ormostamp* copy of *master* (top). .... 139

Figure 6.4-6 SEM image of part of a fully processed photonic crystal nano-ribbon cavity fabricated by nano-imprint technology. .... 139

Figure 6.4-7 SEM image of a portion of the grating coupler after pattern transfer. .... 140

Figure 7.2-1 Initial prototype of smartphone based optical bio-detection platform. (a) 3D printed add-on is attached to the smartphone camera to make a spectrometer, the spectrum of fluorescent tube is captured using this spectrometer but the resolution was not great (~5 nm), and (b) The commercially available (Public lab store) add-on device is composed of narrow slit, 3D printed plastic case and diffraction grating. .... 149

## List of symbols

$\vec{D}$	Displacement vector
$\vec{E}$	Electric field vector
$\vec{H}$	Magnetic field vector
$\epsilon_r(\omega)$	Frequency dependent relative permittivity
$\theta_n$	The angle of the diffracted light
$\Delta\lambda$	Wavelength shift
$c$	Speed of light in a vacuum
$\text{Cl}_2$	Chlorine
$\text{CrCl}_2\text{O}_2$	Chromium oxy-chloride
DI	Deionized
$d_{\text{max}}$	Maximum air-hole diameter
$d_{\text{min}}$	Minimum air-hole diameter
$f$	Optical overlap integral
FF	Filling fraction
$f_r$	Resonant frequency
$h_{\text{etch}}$	Etching depth of the grating
$h_w/h_{\text{wav}}$	Waveguide layer thickness of resonant waveguide grating
I	Intensity after length L
$I_0$	Initial intensity
kHz	Kilo Hertz
L	Length light travelled
$L_c$	Air-hole separation length at the center of the cavity
MHz	Mega Hertz
N	Number of holes in cavity Bragg mirror in each side
$n_c$	Refractive index of cladding
$n_{\text{eff}}$	Effective refractive index
$\text{NH}_3$	Ammonia gas

Ni	Nickel
$n_{\text{liquid}}$	Refractive index of analyte liquid
$n_s$	Refractive index of substrate
$N_t$	Number of tapered holes in nano-ribbon cavity
$n_w$	Refractive index of waveguide
p	Period in nano-ribbon cavity
$R(\lambda)$	Reflection spectra
RAM	Random access memory
S	Bulk sensitivity
S1828	Positive photo-resist
sccm	Standard cubic centimeters per minute
$\text{SiCl}_2\text{H}_2$	Dichlorosilane
$\text{SiH}_4$	Silane gas
$\text{SiO}_2$	Silicon-dioxide
$\text{Si}_x\text{N}_y$	Silicon nitride
$\text{Si}_x\text{N}_y$	Silicon nitride
$T(\lambda)$	Transmission spectra
$T_{\text{sim}}$	Simulation time
$\Lambda$	The period of the grating groove
ZEDN50	Resist developer
ZEP	Name of electron beam lithography resist
$\alpha$	Waveguide loss in $\text{cm}^{-1}$
$\beta$	Wave vector
$\Delta d$	Added layer thickness on sensor
$\Delta n_b$	Bulk index change
$\epsilon_d$	Permittivity of a dielectric material
$\epsilon_m$	Permittivity of a metal
$\lambda_{\text{res}}$	Resonance wavelength
$\omega$	Angular frequency
$\omega_r$	Resonant angular frequency
M	Number of supported modes

$m$	The order of the diffraction
$\theta$	The incident angle
$\lambda$	Wavelength



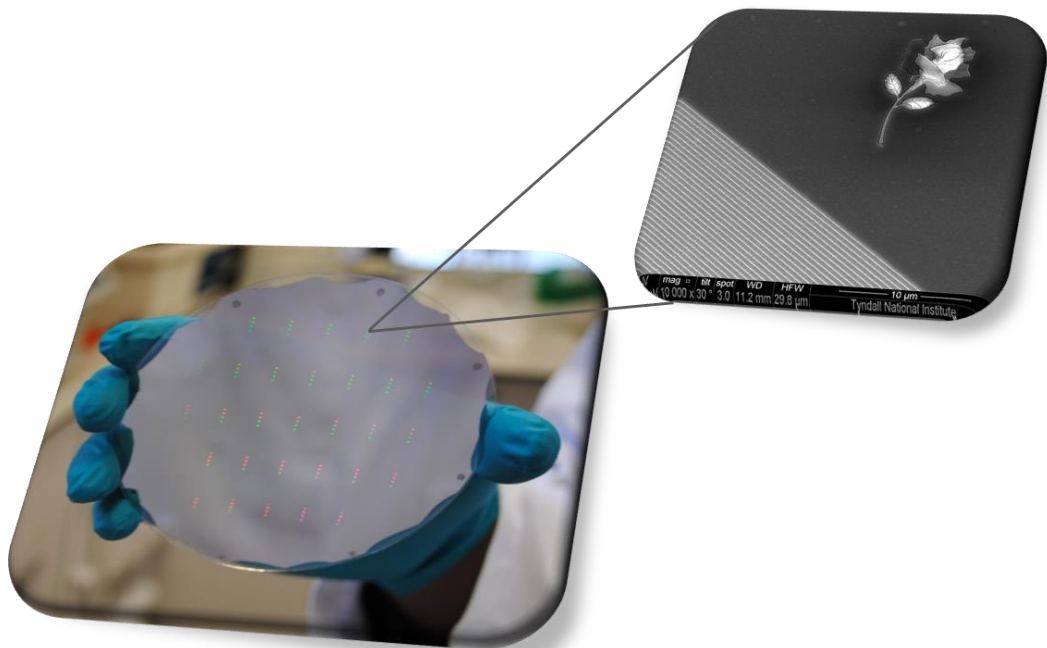
## Abbreviations

1D	One dimensional
2D	Two-dimensional
Ab	Antibody
AR	Anti-reflection
C1q	Complement 1q
C3	Complement 3
Cr	Chromium
D	Detection region
DI	Deionized Water
EBL	Electron beam lithography
EDC	1-Ethyl-3-(3-dimethylaminopropyl)carbodiimide
EM	Electromagnetic
FDTD	Finite difference time domain
FEM	Finite element method
FF	Filling fraction of gratings
FIB	Focused ion beam
FWHM	Full width half maximum
GC	Grating coupler
GMR	Guided mode resonance
HMDS	Hexamethyldisilazane (Adhesion promoter)
HTS	High throughput screening
IC	Integrated circuits
ICP	Inductively coupled plasma
$I_D$	Intensity overlap of resonant mode field
IgG	Immunoglobulin-G
IPA	Isopropanol
IR	Infrared
LED	Light emitting diode
LPCVD	Low Pressure Chemical Vapour Deposition

LPFG	Long-period fiber grating
LSPs	Localized surface plasmons
MHDA	Mercaptohexadecanoic acid
NHS	N-hydroxysuccinimide
NIL	Nano-imprint lithography
PBS	Phosphate-buffered saline
PDMS	Polydimethylsiloxane
PECVD	Plasma enhanced chemical vapour deposition
PhC	Photonic crystal
PML	Perfectly matched layer
PSO	Particle Swarm Optimization
Q	Quality factor
RI	Refractive index
RIE	Reactive ion etching
RIU	Refractive index unit
RW	Resonance wavelength
RWG	Resonant waveguide grating
RWV	Resonance wavelength value
SAM	Single assembled monolayer
scFV	Single-chain variable fragment
SEM	Scanning electron microscope
SPPs	Surface plasmon polaritons
SPR	Surface plasmon resonance
TM	Transverse-magnetic
UV	Ultraviolet
WGM	Whispering-gallery modes

# Chapter 1

## Introduction to Optical Biosensor



**R**ecent progress in nanoscale optical bio-detection technologies has paved the way to the sensitive, label-free and low cost detection of bio-molecules such as virus, DNA and proteins, which are particularly important for implementing next generation clinical diagnostic assays. Such assays implemented on chip scale bio-sensor (lab-on-a-chip) will replace the current labour intensive, time consuming and expensive lab based bio-chemical diagnosis. This chapter gives a brief overview of different types of label-free optical biosensors, their pros and cons, and commercial availability in Section 1.1-1.3. The motivation and context of this thesis work is presented in Section 1.4. Following that, Section 1.5 has provided the outline of this thesis.

## 1.1 Optical Biosensors

Optical biosensors comprise of an optical transducer that converts a biological response into a quantifiable and processable signal, similar to other types of conventional biosensors that utilize electrochemical [1], acoustic [2], or magnetic [3] transducer. The primary advantages of optical techniques over analogous mechanical or electrical label-free methods are: high specification, sensitivity, small size, cost effectiveness and the broad range of applications they can be used for. Typically, in an optical biosensor, a biorecognition layer (i.e., biological probe) is placed in contact with the surface of the sensor. The biorecognition layer is either biomaterial like ligands, functional proteins, or antibodies, or a biological system e.g., living cells, bacteria, or tissues. The interaction between a target analyte and the biorecognition layer produces a change in optical properties of the system which is detected by the optical transducer and used to directly quantify the binding of the target molecules in a sample.

Generally, two detection protocols are used in optical biosensing: fluorescence based detection [4, 5] and label-free detection [6, 7]. In fluorescence based detection either the target molecule or the biorecognition molecule is labeled with tags e.g., fluorescence dye. The intensity of fluorescent signal determines quantitatively the presence of target molecule or the interaction strength in between the probe and target molecule. The

fluorescence based detection is very sensitive and can detect down to single molecule [8], but the process of tagging is not only laborious and costly but also alters the natural functionality of the tagged molecule. Precise quantitative analysis in fluorescence based detection is also challenging because of the fluorescence signal-bias as the number of attached fluorophore in each molecule can not be fully controlled [9]. On the other hand, Label-free detection is also easy to perform, cheap, and allows quantitative and kinetic measurements. In label-free detection, the target molecule is not labeled and the functionality is not altered so that it can interact naturally. As label-free sensing is normally based on a refractive index (RI) change instead of the total sample mass, the detection signal does not scale with sample volume. In contrast, in fluorescence based detection, the signal depends on total number of analyte in the detection volume. So, label-free detection is advantageous over fluorescence based detection for diagnosis where ultrasmall (ng/ml or fg/ml) detection volume is involved.

## **1.2 Refractive Index based Label-free Optical Biosensing**

In the category of label-free optical detection, there exist mainly two types of detection methods: RI based detection and Raman spectroscopic detection. Raman spectroscopic detection [10, 11] is label-free in a sense that it does not require labeling of biomolecule with tags, but it uses scattered Raman light for sensing similar to fluorescence based detection. However, the scope of this thesis is limited to RI based label-free detection only.

Label-free RI sensors [12, 13] based on optical resonance techniques have already drawn huge interest because of the need to develop a simple, low-cost, high throughput detection technology for application like label-free bio-diagnosis. This sensing paradigm will facilitate real-time detection and minimal sample preparation with no requirement of fluorescent tagging of bio-molecule. Examples of optical RI sensors technology include surface plasmon resonance (SPR) [14-17], resonant waveguide grating (RWG) [12, 18-20], 1D [21-24] and 2-D photonic crystal structure [25, 26], long-period fiber grating (LPFG) [27, 28], and ring resonators [29, 30].

### 1.2.1 Surface Plasmon Resonance (SPR) based Sensors

SPR is nothing but oscillating charges at the interface of two media with dielectric constants of opposite signs such as metal (Gold or Silver) and a dielectric [14]. When polarized light containing a range of incident angles, falls on an electrically conducting metallic film (*e.g.*, gold), the incident light is totally reflected but generates an evanescent field penetrating into the metal layer. At a certain resonance angle and wavelength the propagation constant of the evanescent field matches that of the oscillating charge wave at the metal dielectric interface. The evanescent field interacts with and is absorbed by the free electron cloud in the metal generating surface plasmon resonance which results reduction in the intensity of the reflected light at the resonant incident angle and wavelength.

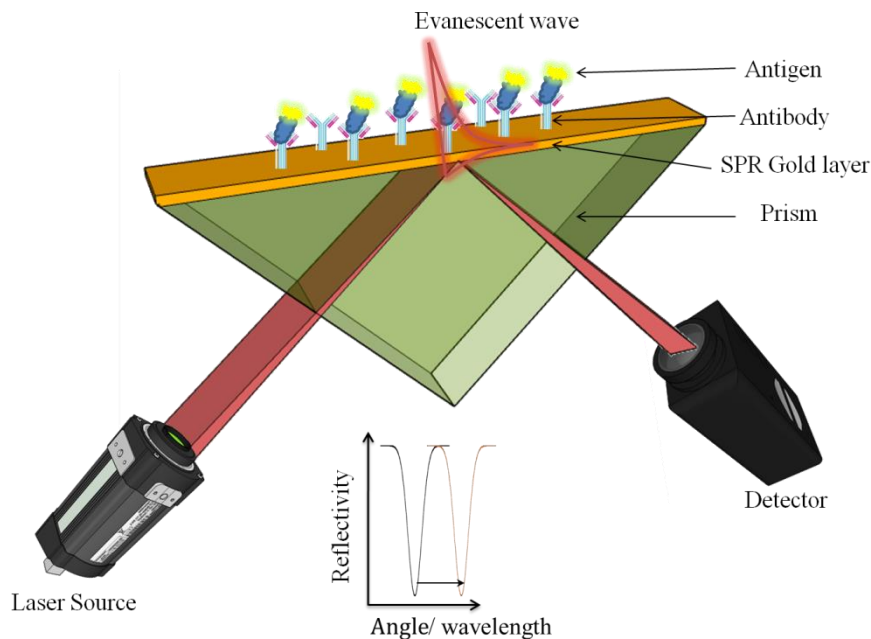


**Figure 1.2-1 Schematic of operational principle of prism coupled SPR based bio-sensing technique. The receptor antibody is coupled to the surface of the gold layer. The incident light is directed by the prism. The reflection spectrum shows notch which represent the Plasmon resonance wavelength. When the target molecule binds to the immobilized receptors the resonance wavelength shifts.**

However, surface plasmons are of two distinct types; localized surface plasmons (LSPs) and surface plasmon polaritons (SPPs). LSPs occur when surface plasmon is excited and

confined in metallic nano-structures of size smaller than the shone wavelength of light. For most noble metals (Gold, Silver etc.) this occurs in visible wavelength. The electric field enhances near the surface of the nanoparticle and then decreases quickly with distance from the surface. This enhanced resonant evanescent wave near the surface is exploited for sensing. On the other hand, SPPs can be excited on flat metal surfaces travelling along the metal-dielectric or metal-air interfaces until its energy is lost by metal absorption or scattering. This SPP based sensing scheme on flat metal surface is traditionally called as SPR which had been first demonstrated back in 1968 by Otto [31] but was not commercialized for bio-sensing until the fall of 1990 by Biacore® [32], whereas LSP based sensing with nanostructured metal is more recent. The important differences between the LSP and SPP or SPR are in their bulk sensitivity and the evanescent decay length (electric field penetration depth) to the sensing medium. The extraordinary spectral sensitivity of SPR sensors is commonly attributed to the unique dispersion of surface plasmons or the multi-mode nature of the sensing scheme [33]. Though the bulk sensitivity of the SPR is few orders of magnitude higher than that of the LSP [34], in terms of biomolecular detection (surface sensitivity) they are comparable in performance because of very short decay length (15-20 nm) of LSP with intensified electric field than the long decay length of SPR (200-300 nm) with comparatively low electric field distribution [34].

The dispersion relation of an SPP can be expressed by Drude model which essentially correlates the relationship between the wave vector ( $\beta$ ) along the interface and the angular frequency ( $\omega$ ) as shown in Eq. (1.1).

$$\beta = \frac{\omega}{c} \sqrt{\frac{\epsilon_m + \epsilon_d}{\epsilon_m \epsilon_d}} \quad (1.1)$$

where  $c$  is the speed of light in a vacuum, while  $\epsilon_m$  and  $\epsilon_d$  are the permittivity of a metal and a dielectric material, respectively. The real part of Eq. (1.1) determines the SPP wavelength, while the imaginary part determines the propagation length of the SPP along the interface.

An SPP is a transverse-magnetic wave i.e., magnetic vector is parallel to the plane of interface. The Electromagnetic (EM) field of the SPP decays evanescently in both the dielectric and the metallic media but, because of low damping in dielectric medium, the major portion of the evanescent EM field is present in the top dielectric medium as shown in Figure 1.2-1. As a result, the real part of the dispersion function is very sensitive and changes proportionally to changes in the refractive index [16]. The principle of SPR, however, only occurs when the light's wave vector component parallel to the metal surface matches that of the SPP. This condition is only satisfied at distinct angles of incidence and wavelength of light, appearing as a drop in the reflectivity of incident light at that wavelength (Figure 1.2-1).

The SPR sensors [14, 18, 35] exploits the evanescent wave at the metal-dielectric interface to characterize the molecular interaction or alteration in biomolecular layer at or near the sensor surface. As the resonance angle or wavelength, is a function of the RI of the solution close to the metal layer of the sensor, any local change due to the binding event causes shift in the resonance angle or wavelength or intensity. So, the detection and quantification of the biomolecular binding event can be accomplished either by measuring the shift in the resonance angle [36] or wavelength [37] or drop in intensity [38]. There are different methods of exciting SPR in the metal-dielectric interface e.g., prism coupling [39], waveguide coupling [40], fiber optic coupling [41], and grating coupling [42]. Prism coupling is the most convenient and common SPR configuration.

Since the first demonstration of SPR sensor in 1983 by Leidberg et al. [40], the technology has been extensively explored as a label-free tool for studying the interaction between the target and bio-recognition molecule. But, the low throughput and limit of the SPR system limits its use in rapid biodetection for application specially where very low volume of analyte solution is involved. Besides, the rebinding of the analyte seems to be a major factor affecting the accuracy of SPR-based kinetics for biomolecule (e.g. antibody) profiling [43].



### 1.2.2 Resonant Waveguide Grating based Sensing

The history of the resonant waveguide grating (RWG) started with a strange optical phenomenon observed by Wood in 1902 [44]. He found a sudden decrease in the diffracted light spectrum of a metallic grating which he was unable to explain and so, named it an “anomaly”. Later, Rayleigh [45], Fano [46], Hessel and Oliner [47], and many others tried to explain the anomaly for metallic grating. Nevertheless, it was not until 1980 when Mashev and Popov [48] demonstrated Wood’s anomaly in an all dielectric RWG instead of metallic RWG.

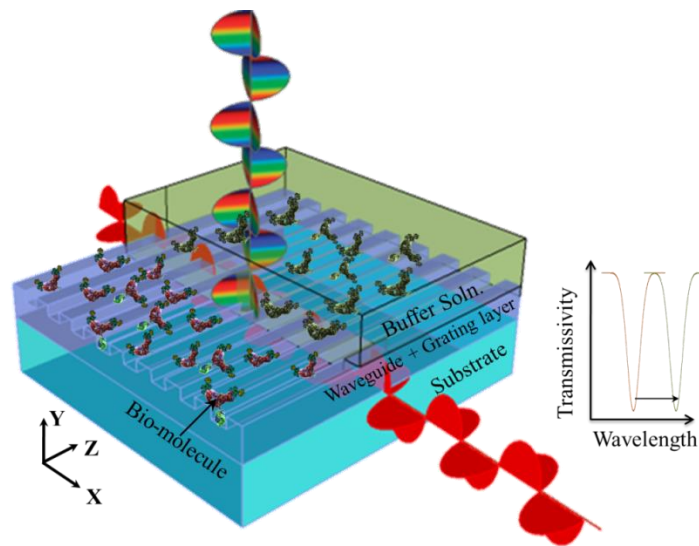


**Figure 1.2-2 Schematic drawing of the RWG sensor showing the operational principle of surface bound bio-molecular sensing for both TE and TM polarized light. The wavelength of the resonance notch in the transmission spectrum shifts because of the surface attachment of the bio-molecules.**

In RWG, when polarized light is incident upon the subwavelength grating (Figure 1.2-2), the higher order diffracted light is phase matched with the zeroth order of the reflected light for a narrow range of wavelengths and angles resulting a resonance and a reflection peaks (i.e., transmission notch) in the spectrum. The localized electric field gets intensified near the sensor surface and increase the light-matter interaction producing the RWG based sensing. An active layer of biological material e.g. functional protein or antibody, is immobilized on the biosensor surface to bind with the target biomolecule.

The interaction of the target biomolecule with the active biolayer on the sensor surface causes local change of RI and thus makes a shift in the resonance wavelength as shown in the transmissivity spectra in Figure 1.2-2.

The RI change also induces a change in resonance angle of incident light. So the binding event can also be interrogated by tracking the resonant angle. The amount of shift in the resonance wavelength or angle is used to quantify the concentration of the target biomolecule in the sample solution. The physical basis of RWG and its sensing mechanism are later discussed in detail in Chapter 2 and Chapter 4. However, Magnusson et al. [49, 50], Brian T. Cunningham et al. [51, 52] and others [20, 52, 53] had explored different materials and design procedures of the RWG for biosensing applications.

Though the history of RWG is comparatively older (started in 1902), the first ever use of RWG as a commercial biosensor is not earlier than 2006 by Corning Inc. with their high-throughput Epic® technology. Unlike SPR, the RWG technology normally measure equilibrium biomolecule binding affinity by microplate well based steady static analysis instead of flow based system. The temperature induced perturbation is still a factor in RWG sensing that is why a temperature control unit is always needed in RWG system which limits its use as a low cost portable biosensing platform. Though not explored that much in literature, RWG sensors can separate the bulk and surface sensitivity (see Chapter 5 for detail) which would be very helpful for ultra-low concentration (~pg/mL) analyte detection.

### 1.2.3 Photonic Crystal Cavity Biosensors

Photonic crystal (PhC) biosensors are another addition to the label-free optical biosensing platform, which has been presented in the literature [25, 26, 54, 55]. A PhC is nothing but periodic subwavelength structure to form photonic bandgap which restricts certain range of wavelength of light to propagate through the PhC and a wide bandgap emerges on the transmission (or reflection) spectrum. However, a local disturbance to the PhC's periodic structure either by missing or reshaping a single or few cells (air holes or pillar) causes photonic “defect” within the bandgap leading to the formation of the defect mode. The

light resonant with the defect mode can propagate in the PhC resulting a relatively sharp peak of the defect mode within the bandgap in the transmission 9optimize. The spectral position of the resonant defect mode is highly sensitive to the change in the local environment around the “defect”. The binding of biomolecules in the defect area causes local RI change and shifts the resonance wavelength which is used to quantify the analyte concentration.

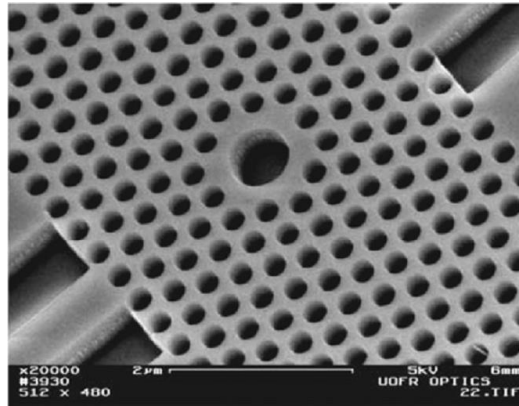


**Figure 1.2-3 PhC (2D) biosensor with point defect made by increasing the size of the central hole and then removing the first layer of surrounding holes demonstrated by Lee and Fauchet et al [26]. Light is injected to the cavity by integrated optical waveguide.**

A two-dimensional (2D) photonic crystal microcavity biosensor [26] is illustrated in Figure 1.2-3. The point defect can be formed by either by increasing or decreasing the central hole. Chow et al. demonstrated the detection of 0.002 ambient RI changes by a PhC cavity sensor with a Quality factor (Q) around 400 in 2004 [25]. Later in 2007, Lee and Fauchet for the first time demonstrated the monitoring of protein binding on the walls of the defect hole of a PhC cavity biosensor and quantitatively measuring the protein diameter [26].

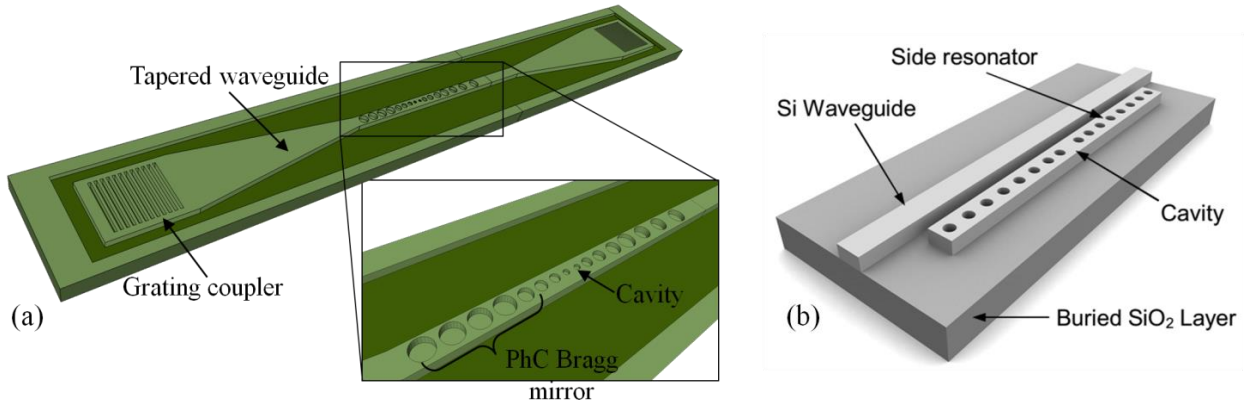


**Figure 1.2-4 Schematic 3D illustration of 1D PhC sensors (a) PhC cavity embedded into the feeding waveguide with grating coupler in both ends for in and out coupling of light (Chapter 6), (b) PhC cavity section is placed separately adjacent to the bus waveguide [56].**

1-D PhC cavity [22, 23, 56-58] has been demonstrated as a significant alternative to the 2D slab based PhC cavity. Here, the PhC cavity (line of air holes with defect at the center) is either embedded in the feeding waveguide (Figure 1.2-4a) or placed adjacent to the waveguide for evanescent coupling (Figure 1.2-4b). The cavity comprises two PhC Bragg mirrors placed face to face with a certain length of separation which acts as a cavity. The waveguide material, width of the waveguide, air hole filling fraction, cavity separation, Bragg mirror ending type (tapered or not) and mirror strength etc. all play important roles to the overall Q of the cavity. 1-D PhC cavities can achieve Q ( $\sim 80,000$  experimental value [23]) as high as those found in the slab based geometries but with much smaller footprint which is beneficial for small analyte detection. Furthermore, it has a naturally convenient geometry for integration with the optical waveguide. The in and out coupling of light from the feeding waveguide can be done either by grating coupler or by edge coupling as shown in Figure 1.2-4a&b respectively. The 1D PhC cavity has already found its application not only in bio-sensing [24, 59], but also in opto-mechanics [60], optical trapping [61] and opto-fluidics [62] etc.

## 1.2.4 Whispering Gallery Mode (WGM) based Resonant Optical Microcavity

Resonant optical microcavity is some sort of closed loop circular/spherical optical waveguide where coupled light propagates through the loop in the form of whispering-gallery modes (WGM) in such a way that constructive interference is generated in the multiple roundtrips over the circumference. The cavity is evanescently coupled by a tapered-fiber/waveguide for in and out coupling of the sustained resonant mode.

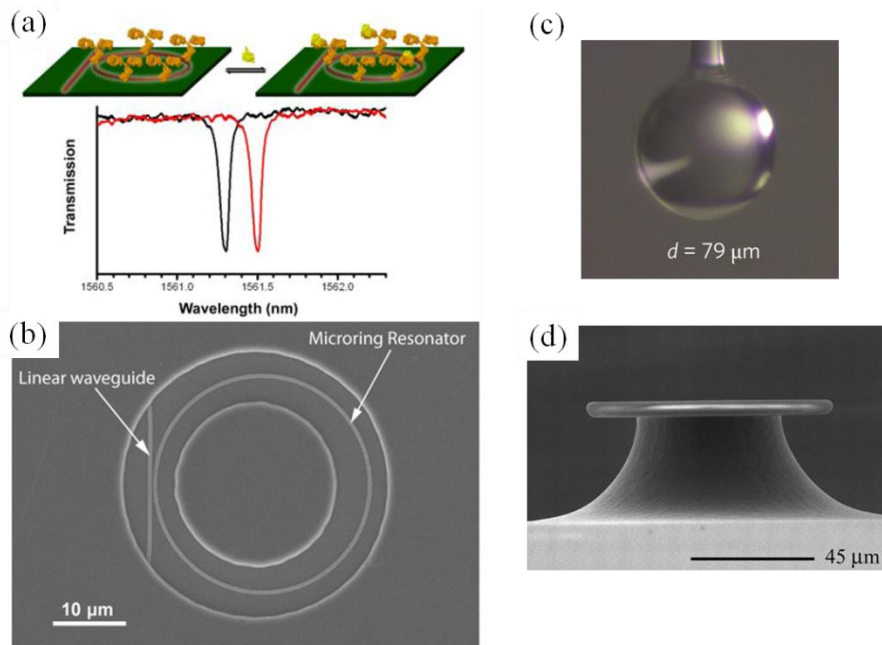


**Figure 1.2-5 (a) Schematically presented biomolecular binding event on a ring resonator and corresponding resonance wavelength shift in the transmission spectrum, (b) SEM image of the SOI micro-ring resonator seen through an annular opening of polymeric cladding. Image adapted from ref. [63], (c) a microsphere of diameter  $d \approx 80 \mu\text{m}$  is melted from an optical fiber used for monitoring single-molecule nucleic acid interactions, and (d) Silica microtoroid optical resonator of  $80 \mu\text{m}$  diameter fabricated on a silicon wafer using planar lithography and reflowed using a CO<sub>2</sub> laser. Figure c&d are adapted from ref. [64]&[65] respectively.**

$$M\lambda = 2\pi r n_{\text{eff}} \quad (1.2)$$

where  $m$  is an integer,  $\lambda$  is the wavelength of light,  $r$  is the radius of the cavity, and  $n_{eff}$  is the effective refractive index of the waveguide mode.

Specific wavelengths of light followed by Eq. (1.2) are supported in a resonant microcavity which emerges as notches in transmission spectrum. Any local change of RI induced by biomolecular binding event is quantified by the amount of shift in the resonant wavelength.

The example of WGM based non-planar resonant optical micro-cavities are microsphere (formed by melting a fiber tip [64] or by polystyrene microspheres in solution [66] or by silica preforms in a hydrogen-oxygen flame [67]), and microcapillary [68] cavity which have already been reported to have tremendously low detection limit, occasionally down to the level of resolving single molecule binding events. Nonetheless, these devices are not readily fabricated in a chip-based format and optical interrogation of such cavities is not trivial (often requiring positioning of extruded optical fibers with nanometer precision and alignment). In contrast, planar micro-ring resonators [29, 30, 69] with chip-integrated linear access waveguides have emerged as promising candidates for scalable and multiplexable biosensing.

Though, theoretically, the resonance peaks of a ring resonator can become spectrally very narrow because of very high Q, practically, the Q-factor is highly dependent on the fabrication precision of the ring, and the sidewalls and surface roughness. The bulk sensitivity of the ring resonator is not very high ( $\sim 200$  nm/RIU for slotted ring resonator [70]), but the narrow peaks facilitate resolution of small shifts in the spectral position of the resonance, nevertheless, the actual detection limit of the sensor is practically dependent on the spectrometer resolution.

### 1.3 Commercialization of Optical Biosensors

Biacore, a Swedish company, launched world's first SPR based analytical instrument for studying biomolecular interactions in 1990. Since the launch of the first product named BIAcore®, the company had been improving the product performance and features by launching semi-automated (Biacore® X) to fully automated (Biacore® 3000) system. In 2006, Biacore was acquired by GE Healthcare. The latest addition to the product line is

Biacore S200 which delivers affinity, kinetics, or fragment-screening data from a 384-well microplate. Several other manufactures like IBIS Tech. have also attempted to expand the ability of SPR imaging based detection by an array of multiplexed system to speed up research by saving sample, labour and sensors. IBIS-MX96 tool claims analyzing 96 biomolecular interactions simultaneously using only 100  $\mu$ l of sample volume overnight.

**Table 1.3-1** categories commercially available major optical biosensor platforms dedicated to drug discovery, proteomics, and clinical diagnostics.

**Table 1.3-1 Optical biosensor technology, their manufacturer, corresponding product name and manufacturer's website.**

Technology	Manufacturer	Instrument	Throughput	Website
SPR	GE Healthcare (Initially Biacore®)	BIACORE	Low	<a href="http://www.biacore.com">www.biacore.com</a>
	IBIS Technologies (Hengelo, Netherleand)	IBIS I and II	Medium	<a href="http://www.ibis-spr.nl">www.ibis-spr.nl</a>
	Sierrasensors, Germany	SPR-2	Low	<a href="http://www.sierrasensors.com/">www.sierrasensors.com/</a>
RWG	Corning Inc., NY	Epic	High	<a href="http://www.corning.com/lifeSciences">www.corning.com/lifeSciences</a>
	MicroVacuum, Hungary	OWLS	Low	<a href="http://www.owls-sensors.com/">http://www.owls-sensors.com/</a>
Interferometer	Farfield, UK	AnaLight	Low	<a href="http://www.farfield-group.com">http://www.farfield-group.com</a>
Ring resonator	ForteBio (Menlo Park, CA)	Octet System	Low	<a href="http://www.fortebio.com">www.fortebio.com</a>
	Genalyte, USA	Maverick	Medium	<a href="http://www.genalyte.com/">www.genalyte.com/</a>

Corning Inc. also moved into the optical bio-detection market by developing a RWG based Epic® technology in 2006, the first label-free screening technology for high throughput screening (HTS) for both cell-based and biochemical assays. The Corning Epic™ system uses RWG sensors in a temperature-controlled environment. A detection fiber bundled with the broadband illumination fiber collects the reflected light and then spectrally measure the ligand-induced wavelength shift for analysis. A series of detection/illumination heads are arranged in a linear fashion in the same column so that they can collect reflected light from multiple wells of a 384-well microplate at once which makes it a very high throughput system (HTS). This optical reader scans the whole microplate enabling up to 40,000 wells to be read in an 8 hour period only. MicroVacuum Inc. also launched their latest grating coupler based label-free detection system: OWLS 210. The basic principle of the OWLS method is waveguide grating coupler where linearly polarized light (He-Ne laser) is coupled by a diffraction grating into the waveguide layer, provided that the incoupling condition is fulfilled. The incoupling is a resonance phenomenon that occurs at a precise angle of incidence, which depends on the refractive indices of the medium covering the surface of the waveguide. The light is guided by total internal reflection to the ends of the waveguide layer where it is detected by photodiodes. By varying the angle of incidence of the light the resonance condition can be obtained from which the effective refractive indices are calculated for both the TE and TM polarized modes. The analyte under investigation is in a cuvette fixed over the optical grating coupler waveguide sensor chip. This assembly is mounted on a precision goniometer, which adjusts the angle of incidence of the external laser beam. However, as the OWLS technology has not been engineered for multiplexed system yet, the throughput of the system is very low feasible for low volume users. Farfield Inc. from UK and ForteBio Inc. from USA also brought up interferometry and ring resonator based low throughput AnaLight and Octet® K2 System respectively targeting low volume users.

### **1.4 Motivation of this Thesis Work**

Although RI sensors are widely used for surface affinity based bio-molecular detection, the information obtained by the present resonance technique is limited [71]. In these



sensors, the resonance wavelength (RW) of the sensor is tuned by a change in the optical density of the medium lying within the range of the evanescent wave. The evanescent wave is an electromagnetic wave at the interface of the sensor surface and analyte solution. The wave extends approximately a few hundreds of nanometer. Any change in RI probed by the resonant mode within the penetration depth causes a corresponding wavelength shift of the optical resonance of the sensor. In addition to refractive index (RI) changes associated with the surface-bound target biomolecular material which is altogether few tens of nanometer thin, thermal induced RI changes of the bulk liquid medium within the range of the penetration depth (hundreds of nm) on top of the bio-layer will also induce a shift in the RW [71]. This could be a significant problem in portable diagnostic applications [72] where thermal variations are likely. The suppression of this unwanted noise will be especially important for applications requiring the detection of smaller size bio-molecules or ultralow analyte concentrations (<ng/ml).

To date, many of the label-free RI sensors including 1D and 2D photonic crystal cavity, some RWG sensors and ring resonator devices operate at infrared (IR) telecom wavelengths associated with the transparency of high index material like Silicon [21, 26, 30, 73], Germanium [73], Gallium Arsenide [69, 74] and Indium Phosphide [75, 76]. There is great interest in extending these devices into the ultraviolet (UV), visible and near IR (~850 nm) wavelengths for bio-sensing applications. Specifically, the wavelength of 850 nm is in a spectral region which is free of overtone absorption resonance in bio-media and low in biological auto-fluorescence. So, sensors operating around 850 nm would improve signal to noise and thus increase sensitivity of the sensor platform. Silicon nitride ( $\text{Si}_x\text{N}_y$ ) is a useful waveguide material in this case due to its relatively large index and transparency across the whole infrared, visible and part of the UV spectrum [77]. Thus, it would be of huge interest to fabricate the  $\text{Si}_x\text{N}_y$  based RI sensor for near IR and visible light spectral region.

Optical nano-structured biosensor like PhC cavity, subwavelength RWG etc. are normally fabricated using electron beam lithography (EBL) on CMOS compatible Si substrate, but Si is not transparent in the visible and near infrared wavelength ( $\lambda < 1000$  nm). Transparent

glass substrate can benefit from illumination through the back of the sensor substrate while the active sensor surface on top is immersed in liquid with the species to be detected.  $\text{Si}_x\text{N}_y$ -based bio-sensing is prospective because the  $\text{Si}_x\text{N}_y$  material is not only optically viable for sensor at the near infrared or visible wavelength but also bio-compatible for the bio-assay experiments.

Pattern writing on glass substrates using EBL is a challenge because of charging effect and corresponding drift during long-time writing on a 4-inch glass wafer. A conductive thin layer on top of the  $\text{Si}_x\text{N}_y$  may solve the charging problem but the nano-fabrication process including that conductive metal etching recipe, pattern transfer recipe etc. should be developed for this purpose. Besides, EBL is very costly and the throughput is very low as it is a serial pattern writing technology. Whereas, using nano-imprint lithography technology will increase the fabrication throughput but it would be challenging to maintain the accuracy of the nano-pattern across the whole wafer. It is of great interest to fabricate the  $\text{Si}_x\text{N}_y$  based RI sensor on transparent glass substrates such as Pyrex or Borosilicate glass with low cost nano-imprint technology.

### 1.5 Outline of the Thesis

This thesis explores the potential of optical nanostructures specifically the resonant waveguide grating and nano-ribbon cavity (1D PhC) for use in label free, real time optical sensing of biomolecules e.g., Immunoglobulin G (IgG) proteins. This chapter has provided the motivation and context of this thesis work, and a brief survey of ongoing research into the field of label free optical bio-sensing has been introduced in terms of its operating principle, commercial availability, and pros and cons. An overview of the resonant waveguide grating, its design principles for use in label free biosensor and selection of the sensor material will be detailed in chapter 2. Chapter 2 will also cover the development of a fully customizable finite difference time domain (FDTD) model for simulating the sensing response of the resonant waveguide grating. The sensor is designed for resonance wavelength at both around 633 nm and 850 nm. At the infrared 850 nm of wavelength, the overtone absorption of the bio media is very low which gives less noise in time of bio-characterization. Whereas with the high power He-Ne laser at the visible

633 nm of wavelength, the sensor characterization is easier than that of infrared wavelength. In chapter 3, the process steps of fabricating the optical nano-structures using electron beam lithography and nano-imprint lithography will be presented. Developing low loss  $\text{Si}_x\text{N}_y$  waveguide material using Plasma enhanced chemical vapour deposition (PECVD) will be detailed. The use of Chromium (Cr) as a hard mask on the non-conductive glass substrate for reducing charging effect in the nano-fabrication processes by EBL will be introduced. The fabrication of very high aspect ratio (1:10) nano-structure on glass will also be demonstrated in chapter 3. The fabricated sensors were characterized for both bulk (detection of liquid based on their bulk refractive index) and surface (quantification of biomolecular binding events) sensitivity, and these results will be summed up in chapter 4. Successful detection of Immunoglobulin-G (IgG) antibodies and antigen confirms that the developed sensors are suitable for bio-molecular diagnosis. For separating the response of bulk sensitivity from the surface binding events, a dual resonance approach will be proposed and verified in chapter 5. Chapter 6 will present the design and fabrication of the resonant nano-ribbon cavity for sensing application. Finally, in “Conclusions and Further Work,” the achievements and experiences will be summed up and a road map for future research will be set out.

## References

- [1] D. Grieshaber, R. MacKenzie, J. Vörös, and E. Reimhult, "Electrochemical Biosensors - Sensor Principles and Architectures," *Sensors*, vol. 8, pp. 1400-1458, 2008.
- [2] M. Saitakis and E. Gizeli, "Acoustic sensors as a biophysical tool for probing cell attachment and cell/surface interactions," *Cellular and Molecular Life Sciences*, vol. 69, pp. 357-371, 2011.
- [3] D. L. Graham, H. A. Ferreira, and P. P. Freitas, "Magnetoresistive-based biosensors and biochips," *Trends in Biotechnology*, vol. 22, pp. 455-462, 2004.
- [4] C. R. Taitt, G. P. Anderson, and F. S. Ligler, "Evanescent wave fluorescence biosensors," *Biosens Bioelectron*, vol. 20, pp. 2470-87, Jun 15 2005.
- [5] H. Mukundan, A. S. Anderson, W. K. Grace, K. M. Grace, N. Hartman, J. S. Martinez, *et al.*, "Waveguide-Based Biosensors for Pathogen Detection," *Sensors*, vol. 9, pp. 5783-5809, 2009.
- [6] X. D. Fan, I. M. White, S. I. Shopova, H. Y. Zhu, J. D. Suter, and Y. Z. Sun, "Sensitive optical biosensors for unlabeled targets: A review," *Analytica Chimica Acta*, vol. 620, pp. 8-26, Jul 14 2008.
- [7] M. Citartan, S. C. B. Gopinath, J. Tominaga, and T. H. Tang, "Label-free methods of reporting biomolecular interactions by optical biosensors," *Analyst*, vol. 138, pp. 3576-3592, 2013.
- [8] W. E. Moerner, "New directions in single-molecule imaging and analysis," *Proceedings of the National Academy of Sciences*, vol. 104, pp. 12596-12602, 2007.
- [9] W. G. Cox and V. L. Singer, "Fluorescent DNA hybridization probe preparation using amine modification and reactive dye coupling," *Biotechniques*, vol. 36, pp. 114-22, Jan 2004.
- [10] I. Notingher, "Raman Spectroscopy Cell-based Biosensors," *Sensors*, vol. 7, pp. 1343-1358, 2007.
- [11] R. A. Tripp, R. A. Dluhy, and Y. Zhao, "Novel nanostructures for SERS biosensing," *Nano Today*, vol. 3, pp. 31-37, 2008.
- [12] I. M. White and X. D. Fan, "On the performance quantification of resonant refractive index sensors," *Optics Express*, vol. 16, pp. 1020-1028, Jan 21 2008.
- [13] X. Fan, I. M. White, S. I. Shopova, H. Zhu, J. D. Suter, and Y. Sun, "Sensitive optical biosensors for unlabeled targets: A review," *Analytica Chimica Acta*, vol. 620, pp. 8-26, 2008.
- [14] J. Homola, S. S. Yee, and G. Gauglitz, "Surface plasmon resonance sensors: review," *Sensors and Actuators B-Chemical*, vol. 54, pp. 3-15, Jan 25 1999.

- [15] E. Zeidan, C. L. Kepley, C. Sayes, and M. G. Sandros, "Surface plasmon resonance: a label-free tool for cellular analysis," *Nanomedicine*, vol. 10, pp. 1833-1846, 2015.
- [16] J. Homola, "Present and future of surface plasmon resonance biosensors," *Analytical and Bioanalytical Chemistry*, vol. 377, pp. 528-539, 2003.
- [17] Y. Yanase, T. Hiragun, K. Ishii, T. Kawaguchi, T. Yanase, M. Kawai, *et al.*, "Surface Plasmon Resonance for Cell-Based Clinical Diagnosis," *Sensors*, vol. 14, pp. 4948-4959, 2014.
- [18] H. N. Daghestani and B. W. Day, "Theory and Applications of Surface Plasmon Resonance, Resonant Mirror, Resonant Waveguide Grating, and Dual Polarization Interferometry Biosensors," *Sensors*, vol. 10, pp. 9630-9646, 2010.
- [19] Y. Fang, A. M. Ferrie, N. H. Fontaine, J. Mauro, and J. Balakrishnan, "Resonant Waveguide Grating Biosensor for Living Cell Sensing," *Biophysical Journal*, vol. 91, pp. 1925-1940, 2006.
- [20] P. Karvinen, "Applications of resonant waveguide gratings," Diss, Joensuu, 2010.
- [21] Y. Chen, W. S. Fegadolli, W. M. Jones, A. Scherer, and M. Li, "Ultrasensitive Gas-Phase Chemical Sensing Based on Functionalized Photonic Crystal Nanobeam Cavities," *Acs Nano*, vol. 8, pp. 522-527, Jan 2014.
- [22] G. C. M. Grande, V. Petruzzelli, and A. D'Orazio "High-Q photonic crystal nanobeam cavity based on a silicon nitride membrane incorporating fabrication imperfections and a low-index material layer," *Progress In Electromagnetics Research B*, vol. 37, pp. 191-204, 2012.
- [23] Q. M. Quan, P. B. Deotare, and M. Loncar, "Photonic crystal nanobeam cavity strongly coupled to the feeding waveguide," *Applied Physics Letters*, vol. 96, May 17 2010.
- [24] G. Shambat, S. R. Kothapalli, J. Provine, T. Sarmiento, J. Harris, S. S. Gambhir, *et al.*, "Single-Cell Photonic Nanocavity Probes," *Nano Letters*, vol. 13, pp. 4999-5005, Nov 2013.
- [25] E. Chow, A. Grot, L. W. Mirkarimi, M. Sigalas, and G. Girolami, "Ultra-compact biochemical sensor built with two-dimensional photonic crystal microcavity," *Optics Letters*, vol. 29, pp. 1093-1095, May 15 2004.
- [26] M. Lee and P. M. Fauchet, "Two-dimensional silicon photonic crystal based biosensing platform for protein detection," *Optics Express*, vol. 15, pp. 4530-4535, Apr 16 2007.
- [27] L. Rindorf, J. B. Jensen, M. Dufva, L. H. Pedersen, P. E. Hoiby, and O. Bang, "Photonic crystal fiber long-period gratings for biochemical sensing," *Optics Express*, vol. 14, pp. 8224-8231, Sep 4 2006.
- [28] R. B. Queiros, C. Gouveia, J. R. A. Fernandes, and F. A. S. Jorge, "Evanescent wave DNA-aptamer biosensor based on long period gratings for the specific recognition of E. coli outer membrane proteins," *Biosensors & Bioelectronics*, vol. 62, pp. 227-233, Dec 15 2014.

- [29] A. Ksendzov and Y. Lin, "Integrated optics ring-resonator sensors for protein detection," *Optics Letters*, vol. 30, pp. 3344-3346, Dec 15 2005.
- [30] T. Baehr-Jones, M. Hochberg, C. Walker, and A. Scherer, "High-Q ring resonators in thin silicon-on-insulator," *Applied Physics Letters*, vol. 85, pp. 3346-3347, Oct 18 2004.
- [31] A. Otto, "Excitation of nonradiative surface plasma waves in silver by the method of frustrated total reflection," *Zeitschrift fr Physik*, vol. 216, pp. 398-410, 1968.
- [32] V. Owen, "Real-time optical immunosensors — A commercial reality," *Biosensors and Bioelectronics*, vol. 12, pp. i-ii, 1997.
- [33] Z. Yu and S. Fan, "Extraordinarily high spectral sensitivity in refractive index sensors using multiple optical modes," *Opt Express*, vol. 19, pp. 10029-40, May 23 2011.
- [34] A. J. Haes and R. P. Van Duyne, "A unified view of propagating and localized surface plasmon resonance biosensors," *Analytical and Bioanalytical Chemistry*, vol. 379, pp. 920-930, 2004.
- [35] J. Homola, "Surface Plasmon Resonance Sensors for Detection of Chemical and Biological Species," *Chemical Reviews*, vol. 108, pp. 462-493, 2008.
- [36] M. Manuel, B. Vidal, R. Lopez, S. Alegret, J. Alonsochamarro, I. Garces, *et al.*, "Determination of Probable Alcohol Yield in Musts by Means of an Spr Optical Sensor," *Sensors and Actuators B-Chemical*, vol. 11, pp. 455-459, Mar 1 1993.
- [37] J. Dostalek, J. Ctyroky, J. Homola, E. Brynda, M. Skalsky, P. Nekvindova, *et al.*, "Surface plasmon resonance biosensor based on integrated optical waveguide," *Sensors and Actuators B-Chemical*, vol. 76, pp. 8-12, Jun 1 2001.
- [38] C. Mouvet, R. D. Harris, C. Maciag, B. J. Luff, J. S. Wilkinson, J. Piehler, *et al.*, "Determination of simazine in water samples by waveguide surface plasmon resonance," *Analytica Chimica Acta*, vol. 338, pp. 109-117, Feb 10 1997.
- [39] K. Matsubara, S. Kawata, and S. Minami, "Optical Chemical Sensor Based on Surface-Plasmon Measurement," *Applied Optics*, vol. 27, pp. 1160-1163, Mar 15 1988.
- [40] B. Liedberg, C. Nylander, and I. Lundstrom, "Surface-Plasmon Resonance for Gas-Detection and Biosensing," *Sensors and Actuators*, vol. 4, pp. 299-304, 1983.
- [41] A. K. Sharma, R. Jha, and B. D. Gupta, "Fiber-optic sensors based on surface plasmon resonance: A comprehensive review," *Ieee Sensors Journal*, vol. 7, pp. 1118-1129, Jul-Aug 2007.
- [42] F. Yu, S. J. Tian, D. F. Yao, and W. Knoll, "Surface plasmon enhanced diffraction for label-free biosensing," *Analytical Chemistry*, vol. 76, pp. 3530-3535, Jul 1 2004.
- [43] D. Hu, S. Fry, J. Huang, X. Ding, L. Qiu, Y. Pan, *et al.*, "Comparison of Surface Plasmon Resonance, Resonant Waveguide Grating Biosensing and Enzyme Linked Immunosorbent Assay (ELISA) in the Evaluation of a Dengue Virus Immunoassay," *Biosensors*, vol. 3, pp. 297-311, 2013.

- [44] R. W. Wood, "On a Remarkable Case of Uneven Distribution of Light in a Diffraction Grating Spectrum," *Proc. Phys. Soc. London*, p. 269, 1902.
- [45] L. Rayleigh, "III. Note on the remarkable case of diffraction spectra described by Prof. Wood," *Philosophical Magazine Series 6*, vol. 14, pp. 60-65, 1907.
- [46] U. Fano, "The Theory of Anomalous Diffraction Gratings and of Quasi-Stationary Waves on Metallic Surfaces," *Journal of the Optical Society of America*, vol. 31, pp. 213-222, 1941/03/01 1941.
- [47] A. Hessel and A. A. Oliner, "A New Theory of Wood's Anomalies on Optical Gratings," *Applied Optics*, vol. 4, p. 1275, 1965.
- [48] L. Mashev and E. Popov, "Zero order anomaly of dielectric coated gratings," *Optics Communications*, vol. 55, pp. 377-380, 1985.
- [49] R. Magnusson, "Wideband reflectors with zero-contrast gratings," *Optics Letters*, vol. 39, pp. 4337-4340, Aug 1 2014.
- [50] R. Magnusson and M. Shokoh-Saremi, "Physical basis for wideband resonant reflectors," *Optics Express*, vol. 16, pp. 3456-3462, Mar 3 2008.
- [51] B. T. Cunningham, "Photonic Crystal Surfaces as a General Purpose Platform for Label-Free and Fluorescent Assays," *Jala*, vol. 15, pp. 120-135, Apr 2010.
- [52] H. Shafiee, E. A. Lidstone, M. Jahangir, F. Inci, E. Hanhauser, T. J. Henrich, *et al.*, "Nanostructured Optical Photonic Crystal Biosensor for HIV Viral Load Measurement," *Scientific Reports*, vol. 4, 2014.
- [53] N. Orgovan, B. Kovacs, E. Farkas, B. Szabo, N. Zaytseva, Y. Fang, *et al.*, "Bulk and surface sensitivity of a resonant waveguide grating imager," *Applied Physics Letters*, vol. 104, Feb 24 2014.
- [54] E. Chow, A. Grot, L. W. Mirkarimi, M. Sigalas, and G. Girolami, "Ultracompact biochemical sensor built with two-dimensional photonic crystal microcavity," *Optics Letters*, vol. 29, p. 1093, 2004.
- [55] N. Skivesen, A. Têtu, M. Kristensen, J. Kjems, L. H. Frandsen, and P. I. Borel, "Photonic-crystal waveguide biosensor," *Optics Express*, vol. 15, p. 3169, 2007.
- [56] S. Mandal and D. Erickson, "Nanoscale optofluidic sensor arrays," *Optics Express*, vol. 16, p. 1623, 2008.
- [57] Q. M. Quan and M. Loncar, "Deterministic design of wavelength scale, ultra-high Q photonic crystal nanobeam cavities," *Optics Express*, vol. 19, pp. 18529-18542, Sep 12 2011.
- [58] C. Schriever, C. Bohley, and J. Schilling, "Designing the quality factor of infiltrated photonic wire slot microcavities," *Optics Express*, vol. 18, pp. 25217-25224, Nov 22 2010.

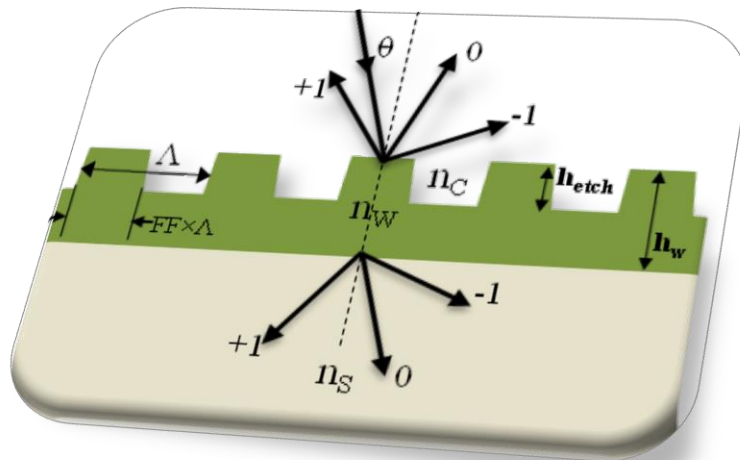
- [59] F. Liang, N. Clarke, P. Patel, M. Loncar, and Q. M. Quan, "Scalable photonic crystal chips for high sensitivity protein detection," *Optics Express*, vol. 21, pp. 32306-32312, Dec 30 2013.
- [60] M. Eichenfield, J. Chan, R. M. Camacho, K. J. Vahala, and O. Painter, "Optomechanical crystals," *Nature*, vol. 462, pp. 78-82, Nov 5 2009.
- [61] D. G. Grier, "A revolution in optical manipulation," *Nature*, vol. 424, pp. 810-816, Aug 14 2003.
- [62] D. Psaltis, S. R. Quake, and C. H. Yang, "Developing optofluidic technology through the fusion of microfluidics and optics," *Nature*, vol. 442, pp. 381-386, Jul 27 2006.
- [63] A. L. Washburn, L. C. Gunn, and R. C. Bailey, "Label-Free Quantitation of a Cancer Biomarker in Complex Media Using Silicon Photonic Microring Resonators," *Analytical Chemistry*, vol. 81, pp. 9499-9506, 2009.
- [64] M. D. Baaske, M. R. Foreman, and F. Vollmer, "Single-molecule nucleic acid interactions monitored on a label-free microcavity biosensor platform," *Nature Nanotechnology*, vol. 9, pp. 933-939, 2014.
- [65] A. M. Armani, R. P. Kulkarni, S. E. Fraser, R. C. Flagan, and K. J. Vahala, "Label-Free, Single-Molecule Detection with Optical Microcavities," *Science*, vol. 317, pp. 783-787, 2007.
- [66] J. Lutti, W. Langbein, and P. Borri, "A monolithic optical sensor based on whispering-gallery modes in polystyrene microspheres," *Applied Physics Letters*, vol. 93, p. 151103, 2008.
- [67] V. S. Ilchenko, X. S. Yao, and L. Maleki, "Pigtailing the high-Q microsphere cavity: a simple fiber coupler for optical whispering-gallery modes," *Optics Letters*, vol. 24, p. 723, 1999.
- [68] I. M. White, H. Oveys, and X. Fan, "Liquid-core optical ring-resonator sensors," *Optics Letters*, vol. 31, p. 1319, 2006.
- [69] A. Koitmäe, C. Bausch, D. Diedrich, E. Stava, H. Vu, and R. H. Blick, "Optical Sensing of Axons in GaAs Ring Resonators," *Biophysical Journal*, vol. 104, p. 162a, 2013.
- [70] C. A. Barrios, "Optical Slot-Waveguide Based Biochemical Sensors," *Sensors*, vol. 9, pp. 4751-4765, 2009.
- [71] R. Magnusson, D. Wawro, S. Zimmerman, and Y. Ding, "Resonant photonic biosensors with polarization-based multiparametric discrimination in each channel," *Sensors (Basel)*, vol. 11, pp. 1476-88, 2011.
- [72] D. Gallegos, K. D. Long, H. J. Yu, P. P. Clark, Y. X. Lin, S. George, *et al.*, "Label-free biodetection using a smartphone," *Lab on a Chip*, vol. 13, pp. 2124-2132, 2013.
- [73] J. Ma and D. Zhang, "Ultra-sensitive bio-sensor based on GMR in self-suspended-membrane-type germanium grating," *Journal of Optics*, vol. 14, p. 085002, 2012.



- [74] S. Combrié, A. De Rossi, Q. V. Tran, and H. Benisty, "GaAs photonic crystal cavity with ultrahigh Q: microwatt nonlinearity at 1.55  $\mu\text{m}$ ," *Optics Letters*, vol. 33, p. 1908, 2008.
- [75] A. L. D. Moreau, R. Janissen, C. A. Santos, L. A. Peroni, D. R. Stach-Machado, A. A. de Souza, *et al.*, "Highly-sensitive and label-free indium phosphide biosensor for early phytopathogen diagnosis," *Biosensors and Bioelectronics*, vol. 36, pp. 62-68, 2012.
- [76] K. Watanabe, Y. Kishi, S. Hachuda, T. Watanabe, M. Sakemoto, Y. Nishijima, *et al.*, "Simultaneous detection of refractive index and surface charges in nanolaser biosensors," *Applied Physics Letters*, vol. 106, p. 021106, 2015.
- [77] S. Romero-Garcia, F. Merget, F. Zhong, H. Finkelstein, and J. Witzens, "Silicon nitride CMOS-compatible platform for integrated photonics applications at visible wavelengths," *Optics Express*, vol. 21, pp. 14036-14046, Jun 17 2013.

# Chapter 2

## Design of Resonant Waveguide Grating based Sensor



## 2.1 Introduction

This chapter presents a brief history of the resonant waveguide grating (RWG) (Section 2.1.1), its physical basis of operation (Section 2.2) and then introduces a numerical solver for designing and analyzing the RWG (Sections 2.3 and 2.4). A simple design procedure of RWG sensor is presented in Section 2.5 based on the findings from the multi-parameter analysis of the RWG. Two different types of bio-sensor sensitivity (bulk and surface) are defined and RWG's sensitivities are analysed by varying its physical parameters (Section 2.6).

### 2.1.1 Historical Background of RWG

In 1902, while observing the spectra of a continuous light source diffracted by a metallic grating, instead of having a continuous spectra, Wood noticed a strange phenomenon: “I was astounded to find that under certain conditions, the drop from maximum illumination to minimum, a drop certainly of from 10 to 1, occurred within a range of wavelengths not greater than the distance between the sodium lines” [44]. He did mention that the incident is related to the polarization of the light: “It occurred to me that polarization might prove to be the key to the explanation of the very singular behavior of the grating of which I am writing” [44]. Wood was unable to explain the finding (Figure 2.1-1) and hence, called it as “singular anomalies”. He also concluded the problem as “one of the most interesting that I have ever met with”.

Rayleigh proposed the 1<sup>st</sup> explanation [45] of Wood's anomalies in the grating spectra relating them as the emergence of the new higher order of diffraction and the passing of the spectra. In another words, the anomaly occurring at a wavelength corresponds to the diffracted wave which emerges tangentially to the gating surface and so, are missing in the spectra. The Rayleigh conjecture proposed the now familiar grating Eq. (2.1) which became a valuable tool for prediction of Wood's anomaly.

$$\sin (\theta_n) = \sin (\theta) + \frac{m\lambda}{\Lambda} \quad (2.1)$$

where  $\theta_n$  is the angle of the diffracted light,  $\theta$  is the incident angle,  $\lambda$  refers to the wavelength,  $\Lambda$  denotes the period of the grating groove and  $m$  is the order of the diffraction.

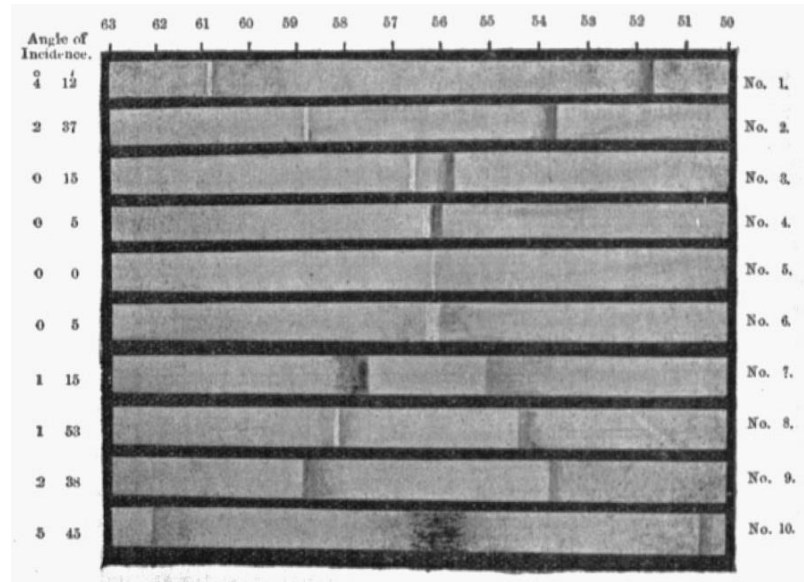


**Figure 2.1-1** Diffraction spectra (of a continuous light source) by metallic grating at ten different angles obtained by Wood [44]. The wavelengths are indicated at the top of the figure in  $\times 10$  nm unit, and the angles of incidence at the left.

Though there was some mismatch between the Wood’s experimental anomaly wavelength values and Rayleigh prediction, the deviation was assumed to be in the range of experimental error.

A few decades later, Fano made a breakthrough by pointing out two types of anomalies [46] (see Figure 2.1-1):

- Sharp anomaly: a sharp edge of intensity drop in the spectrum defined by the Rayleigh diffraction equation
- Diffuse anomaly: it consists of a dark and bright band (minimum and maximum of intensity) which normally occurs at higher wavelength than that of sharp anomaly.

Fano explained the diffuse anomaly by “a forced resonance” related to the “leaky waves supportable by the grating”.

However, in 1965 Hessel and Oliner [47] were led to the same conclusion as stated by Fano [46]. They presented a numerical tool which showed two types of resonances: Rayleigh type which is related to the emergence of the new grating order and the resonance type that emerges from the guided complex wave supportable by the grating. Nevertheless, it was not until 1980 when Mashev and Popov [48] demonstrated the incident of Wood's anomaly in an all dielectric diffraction grating instead of metallic grating showing a rapid increase in zeroth order reflection efficiency from 0 to 100 percent. Because of the possible applications as a tunable, highly efficient, CMOS compatible narrowband spectral filter, further studies were carried out by Magnusson et al. [49, 50, 78-80] using rigorous coupled-wave theory mostly for telecom applications and by Brian T. Cunningham for biosensor applications [51, 52]. Throughout its history, this type of structure has been named differently i.e., 'Guided mode resonance' [49, 50, 78-80], 'Resonant waveguide grating' [20, 53, 81], 'Resonant 1D photonic crystal' [51, 52] etc. In this thesis, it will be termed as the 'Resonant waveguide grating' (RWG).

## 2.2 Physical Basis of RWG Reflectance spectra

Though the history of RWG started back in 1902, the explanation of the physical basis of this optical component is still a topic of study and debate as claimed in [82]. RWG is a periodic subwavelength grating structure with single or multilayer optical waveguide beneath. Figure 2.2-1a shows diffraction grating with period  $\Lambda$ , filling fraction FF, waveguide layer thickness  $h_w$ , and etching depth  $h_{etch}$ . The refractive indices (RI) of the cladding, waveguide and substrate are  $n_c$ ,  $n_w$ , and  $n_s$  respectively in Figure 2.2-1. The resonance in the RWG refers to a sharp peak in the reflection spectrum (or a sharp notch in the transmission spectrum in the same spectral location) for a certain polarization of light. When the polarized light is incident (at angle of  $\theta$ ) upon single/ multi-layer diffraction grating, the zero<sup>th</sup> order of the diffracted light follows the Snell's law of reflection and refraction while the higher order diffracted light either forms forward and backward waves or becomes evanescent mainly depending on the spatial frequency of the grating. Figure 2.2-1a shows that for grating period much larger than the wavelength of light, both zero<sup>th</sup> and higher order ( $\pm 1$ ) diffracted forward wave (top of the grating) and backward waves (back of the grating) are sustained. For subwavelength gratings (period

sufficiently smaller than the wavelength of light) as shown in Figure 2.2-1b only zero<sup>th</sup> order propagates (far field) and all the higher order waves are evanescent (i.e. starts propagating along the waveguide but shortly decays away). Here, the evanescent wave is defined as an electromagnetic wave that propagates along the surface of a grating, and its field amplitudes decay away from the surface exponentially [83].

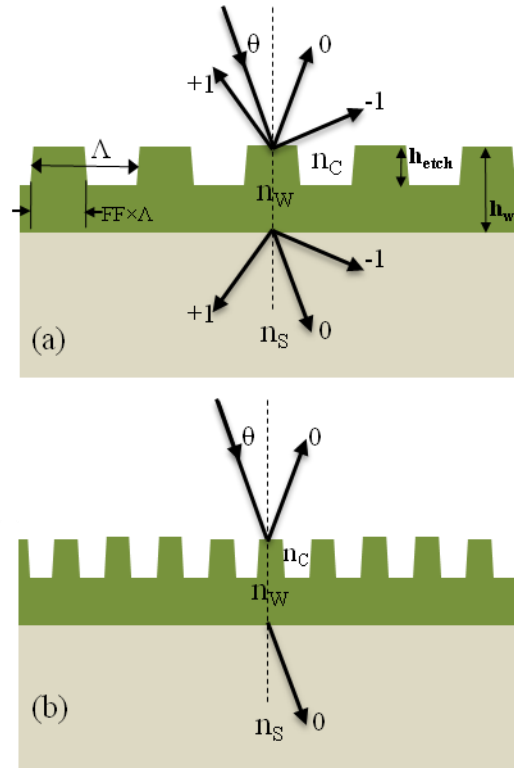


**Figure 2.2-1 Basic single layer waveguide grating (a) Low spatial frequency grating where both zero<sup>th</sup> and higher order diffracted light is present, and (b) High spatial frequency grating where only zero<sup>th</sup> order diffracted light sustains and rest of the orders are evanescent.**

When the subwavelength gratings are in resonance, the strong coupling between the external propagating waves (zero<sup>th</sup> order) and the adjacent evanescent waves (higher order) occurs which produces rapid increase in the reflectance by constructive interference and concomitant decrease in transmittance by destructive interference. So, complete energy exchange between the forward and backward propagating zero-order waves occur. This resonance occurs when one of the diffracted waves generated by the grating element is phase-matched to a leaky mode admitted by the waveguide structure. This happens only for a narrow range of wavelength. The single-layer waveguide grating structures

consisting of gratings and homogeneous layer of same material beneath (i.e. the grating is partially/ fully etched) exhibit a guided mode resonance (GMR) effect as long as the structure functions as a waveguide ( $n_c < n_{\text{eff}}$  &  $n_s < n_{\text{eff}}$ ) and grating layer acts as a phase matching element. The periodic element can provide the necessary phase matching even at normal incidence.

## 2.3 Numerical Model for Design and Analysis

The numerical methods normally used for designing and analyzing photonic structure like RWG, PhC cavity and grating coupler include time-based approach called the finite-difference time-domain (FDTD) method, rigorous coupled wave analysis (RCWA), and finite element method (FEM) etc.

The Finite-Difference Time-Domain (FDTD) method [84] is a common method for solving time and space solution of complex computational electrodynamics (e.g. optical geometries) by Maxwell's equations. As it is a time domain method, FDTD can cover a broad frequency range in single simulation run which is a distinct advantage of FDTD over FEM. In addition, by exploiting Fourier transforms, FDTD can also obtain the frequency solution which can calculate the complex Poynting vector and thus frequency specific electric and magnetic field distribution across the geometry. A commercially available FDTD simulator [85] is interfaced with MATLAB® to run customized script for this thesis work.

### 2.3.1 Solver Physics

This section will introduce the basic mathematical formalism behind the FDTD algorithm. FDTD solves Maxwell's curl equations in non-magnetic materials:

$$\frac{\partial \vec{D}}{\partial t} = \nabla \times \vec{H} \quad (2.2)$$

$$\vec{D}(\omega) = \epsilon_0 \epsilon_r(\omega) \vec{E}(\omega) \quad (2.3)$$

$$\frac{\partial \vec{H}}{\partial t} = -\frac{1}{\mu_0} \nabla \times \vec{E} \quad (2.4)$$

where  $\vec{H}$ ,  $\vec{E}$ , and  $\vec{D}$  are the magnetic, electric, and displacement fields respectively. And,  $\epsilon_r(\omega) = n^2$ , is the complex relative dielectric constant with  $n$  as the refractive index. If we assume that the geometry is independent in  $z$  dimension (i.e. infinite in  $z$  direction) then

$$\epsilon_r(\omega, x, y, z) = \epsilon_r(\omega, x, y) \quad (2.5)$$

$$\frac{\partial \vec{E}}{\partial z} = \frac{\partial \vec{H}}{\partial z} = 0 \quad (2.6)$$

So, the Maxwell's equations can be split into two sets of equations each of which deals with three vectors which can be solved in  $x$ - $y$  plane. These two sets of equations are termed as TE (transverse electric) and TM (transverse magnetic) equations. For TM case, the Maxwell's equations reduce to:

$$\frac{\partial D_z}{\partial t} = \frac{\partial H_y}{\partial x} - \frac{\partial H_x}{\partial y} \quad (2.7)$$

$$D_z(\omega) = \epsilon_0 \epsilon_r(\omega) E_z(\omega) \quad (2.8)$$

$$\frac{\partial H_x}{\partial t} = -\frac{1}{\mu_0} \frac{\partial E_z}{\partial y} \quad (2.9)$$

The FDTD method solves these equations on a discrete spatial and temporal grid/mesh to get the  $E$  and  $H$  fields of that grid. FDTD solver uses a rectangular, Cartesian style mesh. Smaller the mesh size more precise the geometrical representation would be but it would substantially increase the memory and processing power usages. To speed up simulations, a conformal meshing [86] is used with lower memory requirement. In addition, smaller meshing is used in high index material to have constant number of mesh points per wavelength across the geometry which ensures the accuracy of the simulator. In some cases, it was necessary to manually impose additional meshing constraints i.e. to force the mesh to be smaller near complex structures (often for metallic material and sharp bending) where the fields are changing very rapidly. However, the fundamental simulation quantities (material properties and geometrical information, electric and magnetic fields)



are calculated at each mesh point. The simulation evolves the E and H fields forward in time.

Dispersive materials with experimental tabulated data in (n,k) format were incorporated into the model by fitting this data with a multi-coefficient material model (e.g. Drude, Debye or Lorentz model).

## 2.4 RWG Simulation using FDTD

The simulations are done on a unit cell (size of one period of the grating) bounded by orange colored box as shown in Figure 2.4-1. Periodic boundary conditions are applied in  $\pm X$  axis boundaries whereas perfectly matched layer (PML) is applied in the  $\pm Y$  boundaries. PML is an absorbing boundary condition which uses the mathematical method of attenuating any signal travelling to that boundary and thus, deletes any back reflections coming from the boundary to the computational domain.

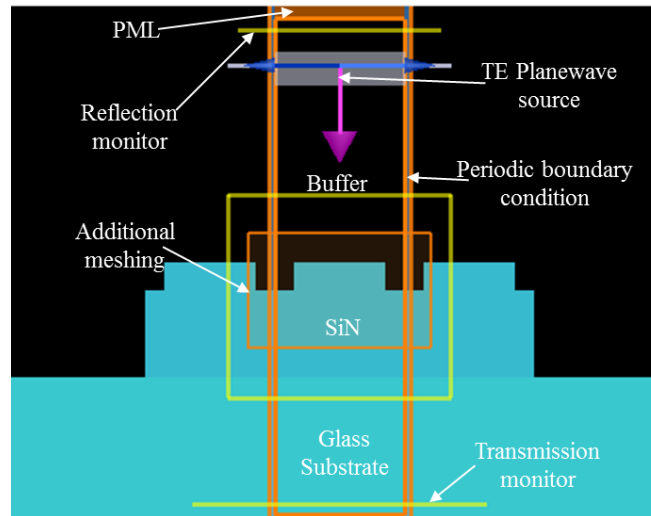


**Figure 2.4-1 RWG simulation setup in the FDTD graphical user interface. The larger orange rectangle is the simulation window (for unit cell of RWG) with PML in top and bottom, and periodic boundary condition at left and right side. The  $\text{Si}_x\text{N}_y$  grating on glass substrate is set to be covered with buffer solution in the simulation. TE polarized planewave light source is applied from top of the grating and two monitors are at the top and bottom for calculating the RWG reflection and transmission spectra respectively.**

This work considered a partially etched Silicon nitride ( $\text{Si}_x\text{N}_y$ ) grating on a Borosilicate glass substrate as the RWG platform. The period ( $\Lambda$ ),  $\text{Si}_x\text{N}_y$  waveguide layer thickness

( $h_w$ ), etching depth ( $h_{\text{etch}}$ ), and filling fraction (FF) are initially set as 450 nm, 400 nm, 150 nm, and 50% respectively. A planewave TM polarized light source is placed on top of the grating covered by buffer solution (RI=1.332) and a monitor is placed under the substrate to measure the transmittance of the RWG (Figure 2.4-1). The reflection and transmission spectra for both TE and TM polarization for the abovementioned RWG geometry is presented in Figure 2.4-2.

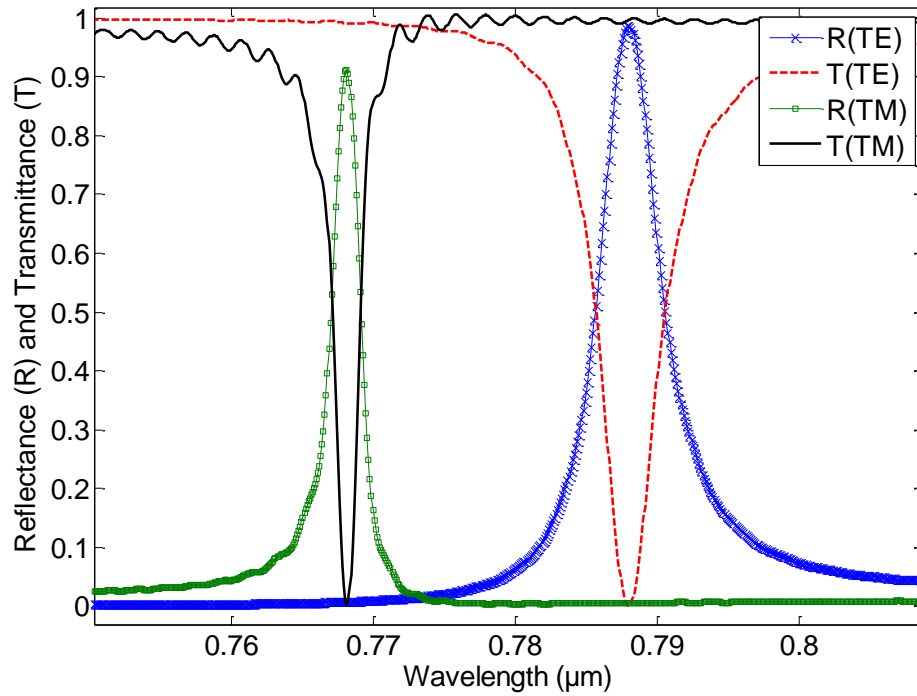


**Figure 2.4-2 Reflection and transmission spectra of a single layer RWG for both TE and TM polarization.**

The resonance wavelengths for TE and TM polarizations are 788 nm and 768 nm of wavelength respectively which are separated by 20 nm in this case.

As there is no analytical expression for resonance linewidth and RWG sensor sensitivity dependence on the physical parameters of the structure, the numerical study is necessary.

### 2.4.1 Multi-order multimode RWG

Much past research on RWG devices has focused on a thin waveguide layer which supports only a single leaky mode. In contrast, Liu and Magnusson explored properties of multi-order multimode RWG elements to design wideband and multi-wavelength filters [87]. Using a dielectric thin-film structure consisting of a coupling grating placed on top of an adjacent waveguide, guided-mode resonance filters exhibiting multiple reflection peaks within a specified wavelength range can be obtained. These peaks originate in the resonant waveguide modes that are excited by the diffracted waves dispersed by the grating. Subsequently, Boonruang et al. designed multiline RWG (also known as GMR) filters using two-dimensional (2D) grating structures with rectangular and hexagonal grids. They implemented spectral location control by inducing leaky modes into specific directions on these grids [88]. Greenwell et al. designed 1D multi-wavelength GMR filters based on multimode waveguides with particular emphasis on resonance separation control [89].

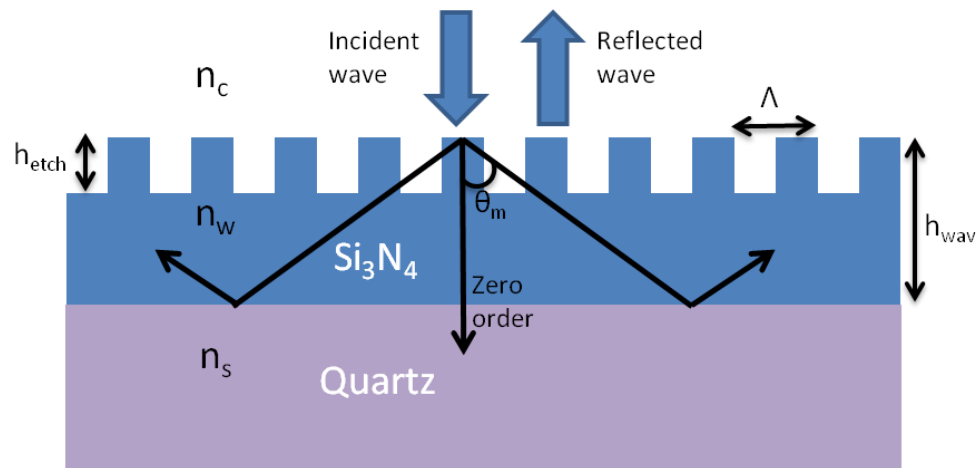


**Figure 2.4-3 Model of the device under study denoting thicknesses of the waveguide layer ( $h_{\text{wav}}$ ) and refractive indices ( $n$ ) of the various regions as well as the period ( $\Lambda$ ) of the grating.**

The RWG device under study is composed of a partially etched subwavelength grating in a single  $\text{Si}_3\text{N}_4$  layer on top of transparent Quartz substrate as shown in Figure 2.4-3. The  $m^{\text{th}}$  diffraction order indicated in Figure 2.4-3 excites a leaky waveguide mode at a particular wavelength. Under variation of the wavelength, the allowed modes will be

sequentially excited with a guided-mode resonance arising for each mode. The mode angle satisfies:

$$\sin(\theta_m) = \frac{m\lambda}{(\Lambda \times n_w)} \quad (2.10)$$

with  $\lambda$  being the free-space wavelength,  $\Lambda$  the period,  $m$  the diffraction order and  $n_w$  the refractive index of the waveguide. Multiple resonance modes from the same diffraction order can be generated by increasing the thickness of the waveguide layer and optimizing the etching depth for that corresponding layer thickness. Figure 2.4-3 shows the FDTD simulated transmission spectrum of a RWG with  $\Lambda = 440$  nm,  $h_{\text{etch}} = 160$  nm, filling fraction = 60% and different waveguide layer thickness ( $h_{\text{wav}}$ ) = 400, 600, 1000 nm. Inserting these RWG parameters in Eq. (2.10), it is found that only 1<sup>st</sup> order diffraction can contribute to the resonances. However, the spectral density of the RWG peaks in this device is controlled by the thickness  $h_{\text{wav}}$  because it determines the number of modes sustained by the waveguide. The thicker the waveguide, the higher the number of modes available in the waveguide.

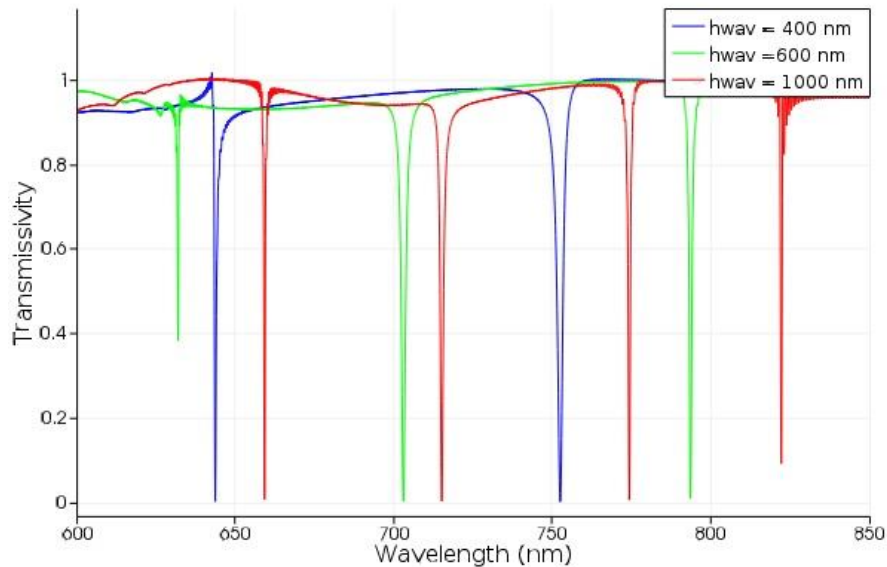


**Figure 2.4-4** Calculated transmission spectra of the RWG with different waveguide layer thickness,  $h_{\text{wav}} = 400, 600, 1000$  nm which excites 2, 3 and 4 resonance modes respectively.

Figure 2.4-4 shows all the resonance modes available within a wavelength range of 600 nm to 850 nm for different waveguide thickness. For TE polarization of light incident upon the RWG two degenerate resonance modes arise for a thin waveguide layer thickness of 400 nm whereas for waveguide thickness of 600 nm and 1000 nm, 3 and 4 resonance modes at different phase matched wavelength arise. The formula for the appropriate number of modes supported by a homogeneous dielectric waveguide is defined as [90]

$$M \sim \frac{2h_{wav}}{\lambda} \sqrt{n_w^2 - n_c^2} \quad (2.11)$$

For  $h_{wav} = 1000$  nm,  $n_w = 1.9$  ( $\text{Si}_3\text{N}_4$ ) and  $n_c = 1$  (air),  $M$  is found  $\sim 4$  at a wavelength of 750 nm from Eq. (2.11). The FDTD simulated results as shown in Figure 2.4-4 also verifies the four guided mode resonances for  $h_{wav} = 1000$  nm.

## 2.5 RWG Design Procedure

The design procedure of RWG starts by choosing the initial grating material, substrate, light incidence angle, period, waveguide thickness and filling fraction of the grating targeting a given wavelength, linewidth and sensitivity (see Section 2.6) of the RWG sensor in resonance. It can be a single-layer, double-layer, or multilayer structure. For normal incidence, the initial grating period is estimated from [91]

$$\Lambda = \frac{\lambda_{res}}{n_{eff}} \quad (2.12)$$

where  $\lambda_{res}$  and  $n_{eff}$  are the resonance wavelength and effective refractive index of the grating waveguide layer. The trial filling factor is usually chosen to be 0.5, which gives the largest linewidth of the resonance spectrum (Section 2.5.1).

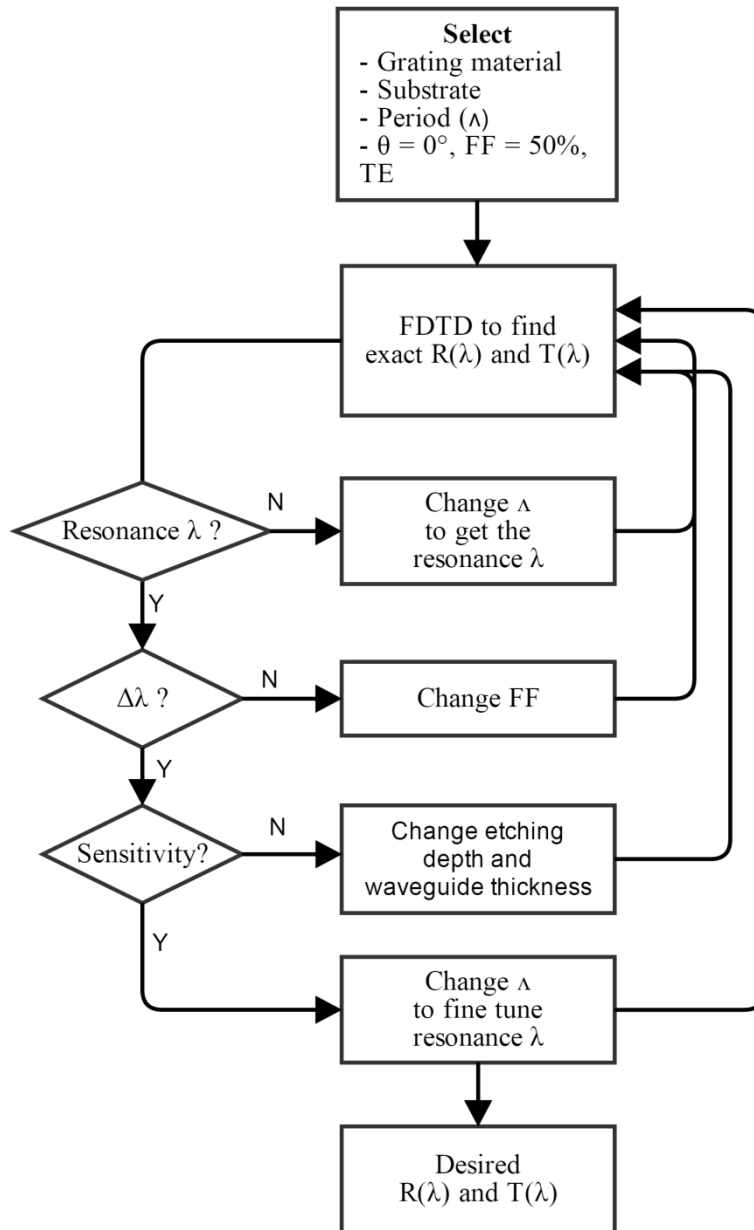


**Figure 2.5-1** Flow-chart schematically shows the design procedure of the RWG targeting specific resonance wavelength, linewidth and sensitivity.

The waveguide layer thickness defines the single and multi-resonance property of the RWG and so, set accordingly (see Section 2.4.1 for multi-resonance property). Next, the FDTD simulator is employed to find the appropriate reflection ( $R(\lambda)$ ) and transmission

( $T(\lambda)$ ) spectra and locate the  $\lambda_{\text{res}}$ . The resonance wavelength can be further tuned by the period as  $\lambda_{\text{res}}$  is directly proportional to the period as shown in Eq. (2.12). The spectral response of the trial RWG structure is then examined to assess the linewidth and sensitivity (see Section 2.6). If the sensitivity requirement is not fulfilled, changing the waveguide layer thickness and etching depth of the grating would help changing the electromagnetic field overlap integral (see Section 2.5.1 and 2.5.2) and change sensitivity. The linewidth can be reduced to meet the requirement of Q-factor by either increasing or decreasing the filling factor from 0.5 or by etching more of the grating (i.e. increasing the  $h_{\text{etch}}$ ) as shown in Section 2.5.1. When the sensitivity and linewidth requirements are fulfilled, the resonance wavelength can be fine tuned by adjusting the period of the grating. The design procedure presented here is a simple numerical approach for designing RWG of specific resonance wavelength, Q-factor ( $\sim 1/\text{linewidth}$ ) and sensitivity. Alternatively, the RWG sensor can be designed using a global optimization method such as the Particle Swarm Optimization (PSO) technique [92].

### 2.5.1 Role of FF and $h_{\text{etch}}$ on RWG Spectral Linewidth

The filling fraction (FF) and etching depth ( $h_{\text{etch}}$ ) of the grating were varied to investigate their role in the RWG transmittance spectra. Figure 2.5-2a and Figure 2.5-2b show the transmittance mapping of the RWG for different FF and  $h_{\text{etch}}$  respectively. The linewidth of the resonance is very much dependent on both the FF and  $h_{\text{etch}}$ . The maximum linewidth is found for FF=0.5 and the linewidth decreases to zero when FF approaches from 0.5 to either 0 or 1 (no grating). This behavior can be attributed to the coupling efficiency of the grating which is proportional to  $\sin(\pi \times \text{FF})$ . The local maximum value of  $\sin(\pi \times \text{FF})$  is for FF=0.5 and its value approaches to 0 when FF goes from 0.5 to 0 or 1.

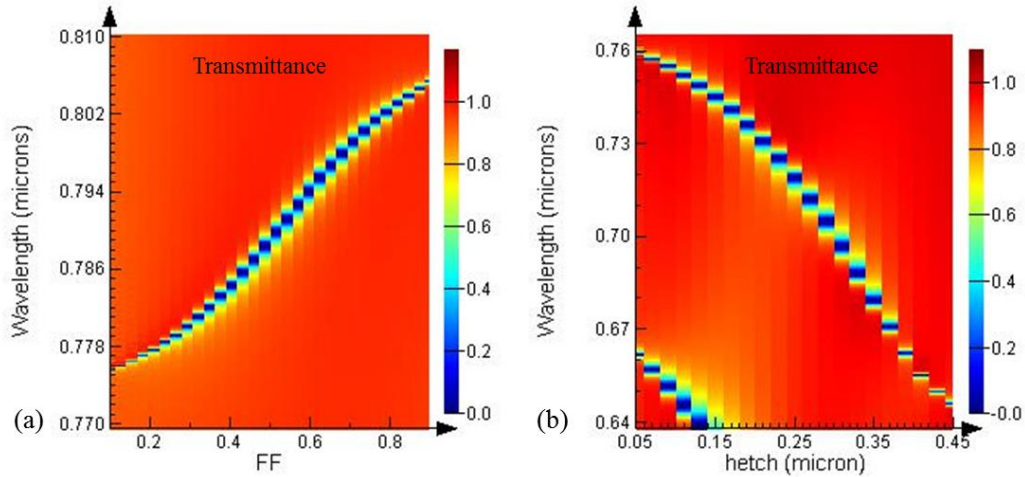


**Figure 2.5-2** Transmittance of the RWG for (a) Varying filling fraction (FF), and (b) Etching depth ( $h_{etch}$ ).

### 2.5.2 Parameters of the Optimized RWG

Simulations were carried out to find optimized structure parameters for a RWG working with wavelengths of 850 nm and 633 nm. The 850 nm wavelength was chosen because the bio-overtone absorption noise is low at this wavelength and also low cost VCSEL source is available at this wavelength. The wavelength of 633 nm was also selected because common optics (sources, detectors) are more sensitive and readily available at this wavelength. The optimized parameters for the two designs are reported in Table 2.5-1.

**Table 2.5-1** Designed parameters of the RWG for visible and infrared wavelength.

Sensor Type	Targeted Resonance wavelength	Parameters	Design
Visible RWG (Dual resonance)	633 nm and 760 nm	Filling fraction	60%
		Period	440 nm
		Etch depth	200 nm
Infrared RWG	850 nm	Filling fraction	45%
		Period	510 nm
		Etch depth	250 nm



Figure 2.5-3 shows the transmission spectrum (in buffer) obtained with the optimized parameters for the visible RWG along with the electric field profile at the two resonance wavelengths. As can be seen, two resonance peaks are obtained, one is located at 633 nm and a second one at 760 nm.

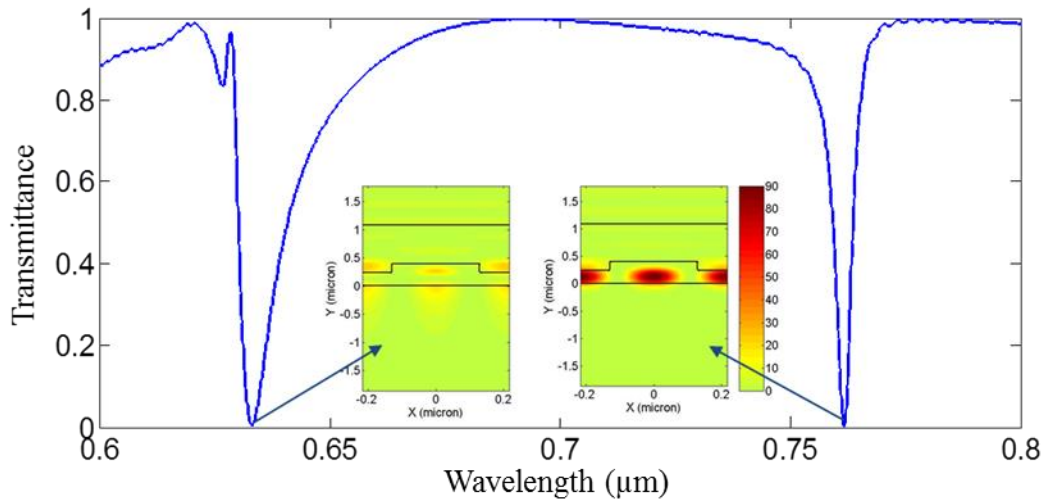


**Figure 2.5-3** Transmittance of visible RWG with parameters listed in Table 2.5-1, shows dual resonances. Simulation of the electric field at the resonance wavelengths (left: 633 nm, and right: 760 nm) of the RWG sensor are presented.

As shown in Figure 2.5-3 the first resonance has a sideband at the left side and also the shape is not fully symmetrical whereas the second resonance is almost symmetrical with no sideband. Reduction of the sideband and improvement of the shape can be done by adding anti-reflection (AR) layers beneath the RWG layer and furthermore independent controlling of these layer thicknesses [93]. The symmetry of the resonance peak shape and the sideband values are closely related because the symmetry of the peak is also influenced by the antireflection mechanism. Inclusion of multiple layers (3, 5 etc.) for antireflection mechanism along with the independent control of these layer thicknesses to minimize the sideband for two completely different spectral resonance modes would make the design and fabrication of the sensor complicated. So, it was intended to use single layer waveguide for easy fabrication of RWG though there is nominal sideband present at the 1<sup>st</sup> resonance as found in Figure 2.5-3.

## 2.6 Sensor Sensitivity

The sensing mechanism in the RWG is the detected spectral shift of the resonance induced either by RI change of the medium surrounding the RWG or by local RI change for the attachment of biolayer on the RWG surface. The former is termed as ‘Bulk’ sensitivity whereas the later is known as ‘Surface’ sensitivity.

### 2.6.1 Bulk Sensitivity

The relationship between the small change in the bulk RI and the corresponding spectral shift of resonance can be quantified by the ‘Optical overlap integral’,  $f$  (Eq. 2.13), which describes the ratio of the electric field energy of the guided mode existing outside the dielectric structure (i.e. in the region covered by the liquid) with the total energy of the resonance mode.

$$f = \frac{\int_{V_{liquid}} \epsilon |\vec{E}|^2 dr^3}{\int_{V_{liquid+dielectric}} \epsilon |\vec{E}|^2 dr^3} \quad \begin{matrix} liquid \\ liquid+dielectric \end{matrix} \quad (2.13)$$

So, the bulk sensitivity ( $S$ ) can be defined as [94]:

$$S = \frac{\Delta\lambda}{\Delta n_{liquid}} = f \frac{\lambda_{res}}{n_{eff}} \left( \frac{nm}{RIU} \right) \quad (2.14)$$

where  $\lambda_{res}$ ,  $n_{eff}$ , and  $f$  are the resonance wavelength, effective refractive index of the dielectric RWG waveguide, and optical overlap integral respectively. From Eqs. (2.13) and (2.14), it is recognizable that the large value of  $f$  means large portion of total electric field available for interacting with the change of RI of the liquid medium, and so increase the bulk sensitivity,  $S$ . The spectral location of the resonance wavelength and the material of the grating are also important in achieving high sensitivity, but all these three

parameters are interlinked to one another. So, a numerical study is essential for studying the bulk sensitivity.

It can be seen from the electric field intensity distribution in Figure 2.5-3 that the field at 633 nm penetrates deeper into the superstrate (in this case buffer solution on top of grating) while the electric field at 760nm stays confined to the interface. So, it can be deduced that the first resonance would act as a bulk sensor (*i.e.* capable of monitoring change of refractive index “away” from the surface) whereas the second resonance would act more likely as a surface sensor. See Chapter 5 for detail of the proposed dual resonance approach of RWG exploiting the different behavior of these two resonances.

To calculate the bulk sensitivity of the 1<sup>st</sup> resonance (around 633 nm) of the sensor, resonance mapping with variation in the background refractive index of the medium on top of the grating is done as shown in Figure 2.6-1. The slope ( $\frac{\partial \lambda}{\partial n_c}$ ) of the envisaged blue curve (*i.e.* resonance tracking line) in Figure 2.6-1 gives the bulk sensitivity value in nm/RIU unit.

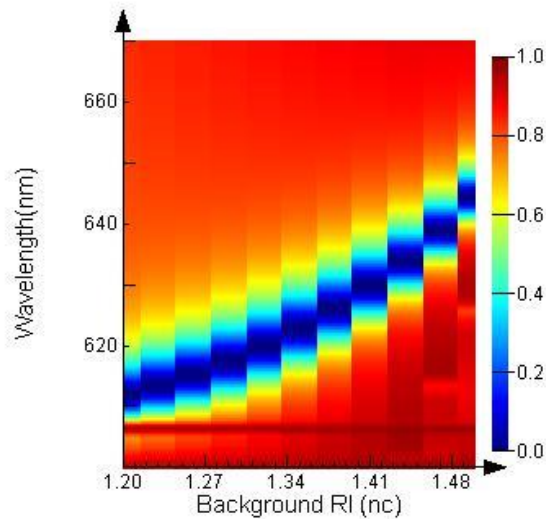


**Figure 2.6-1 Bulk sensitivity mapping using simulations. The refractive index of the medium ( $n_c$ ) on top of RWG is varied and the corresponding resonance transmittance spectra are mapped.**

The slope  $(\frac{\partial\lambda}{\partial n_c})$  changes with the background RI ( $n_c$ ). The maximum value of bulk sensitivity is found 183.33 nm/RIU

### 2.6.2 Surface Sensitivity

The surface sensitivity refers to the spectral shift of the resonance due to the attachment of a thin layer (<30 nm) of bio-molecule on the RWG sensor surface which causes change in the effective RI ( $n_{eff}$ ) of the waveguide layer and so to the resonance wavelength following Eq. (2.12).

The effective RI ( $n_{eff}$ ) of the waveguide layer can be defined as the weighted average of the electric field intensity [91]:

$$n_{eff}^2 = \frac{\iint_{-\infty,0}^{\infty,\Lambda} \epsilon(x,y) |E(x,y)|^2 dx dy}{\iint_{-\infty,0}^{\infty,\Lambda} |E(x,y)|^2 dx dy} \quad (2.15)$$

The shift in the resonance wavelength can be calculated by

$$\Delta\lambda = \Delta n_{eff} \Lambda \quad (2.16)$$

Any change of RI in the superstrate ( $n_c$  in Figure 2.2-1) or the increase in dielectric permittivity due to the adsorption of biomolecules will change the  $n_{eff}$ . Here, for the measurement of the surface sensitivity, it is assumed that there is no change in bulk medium and the only change is from the bio-molecular attachment.

Since the  $n_{eff}$  is weighted by the normalized resonant E-field intensity at any given point, a computational model was developed which gives the electromagnetic field distribution across the RWG geometry as a function of material and geometric parameters to understand how to optimize RWG sensing performance.

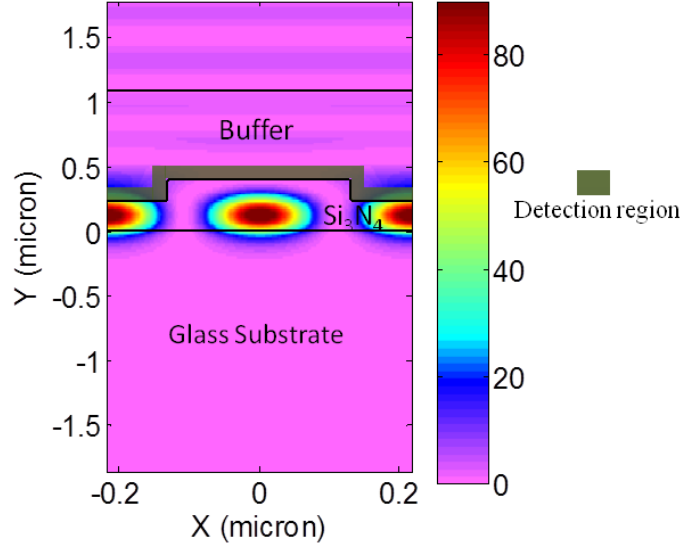


**Figure 2.6-2 Electric field distribution of the resonant mode of the RWG with marked biomolecular detection region.**

The computational window is divided into two regions: Detection region (marked as green in Figure 2.6-2) and the constant region (rest of the region). The change in  $n_{eff}$  can be written as

$$\Delta n_{eff} = \sqrt{\epsilon_c + I_D \epsilon_{D2}} - \sqrt{\epsilon_c + I_D \epsilon_{D1}} \quad (2.17)$$

where the contribution to the dielectric constant ( $\epsilon$ ) is divided into two parts: superscript ‘c’ denotes for the contribution from the constant region whereas ‘D’ refers to the detection region.  $\epsilon_{D1}$  and  $\epsilon_{D2}$  are the initial and final dielectric permittivity in the detection zone. The contribution from the detection zone is given by the product of the permittivity in that region and the resonant mode’s field intensity overlap ( $I_D$ ) with the biomolecular detection zone. So,  $I_D$  is defined as

$$I_D = \frac{\iint_D |E(x,y)|^2 dx dy}{\iint_{-\infty,0}^{\infty,\Lambda} |E(x,y)|^2 dx dy} \quad (2.18)$$

Eqs. (2.16-2.18) reveals three key parameters to increase the surface sensitivity of RWG. From Eq. (2.16) it seems evident that the larger the period ( $\Lambda$ ), the more the sensitivity, but this is not always true because the E-field distribution changes with period and

concomitantly changes  $\Delta n_{eff}$ . Eq. (2.17) reveals that the low value of dielectric permittivity of the constant region ( $\epsilon_c$ ) i.e. the low RI grating material would yield more effective index tuning for a given index change in the detection region. The last but perhaps the most important parameter is the resonance mode E-field overlap integral with the detection region,  $I_D$  which can be used as an indicator of RWG's surface sensitivity. The maximum sensitivity would be achieved for  $I_D=1$  which corresponds to the ideal case of complete overlap of the mode's field with the detection region. So, maximization of  $I_D$  value is done by varying RWG parameters in simulations. While the thickness of the detection region will vary from application to application, for IgG protein sensing application I have considered the detection region of 20 nm of thickness.

The  $I_D$  value has been calculated for different FF and then, with the FF value which gives local maximum of  $I_D$ ,  $h_w$  is varied to get the overall maximum value.

**Table 2.6-1 Calculated  $I_D$  values from resonant mode E-field distribution for (a) Different FF values, and (b) Different values of grating waveguide thickness ( $h_w$ )**

(a)		(b)	
FF(%)	$I_D$ (%)	$h_w$ (nm)	$I_D$ (%)
35	11.2	200	9.5
40	15.9	250	12.1
<b>45</b>	<b>16.1</b>	300	13.6
50	15.1	400	14.8
55	8	450	17.3
		<b>500</b>	<b>18.2</b>
		550	18.2,16.1
		600	7.3,16.4
		650	10.9,7.9
		700	17.7,12.6

Further simulations of RWG with parameters of FF=45%,  $h_w=500$  nm,  $h_{etch}=500$  nm, period=440 nm revealed that an attachment of 20 nm (~7 nm of Antibody + 13 nm of Antigen) of bio-molecule (refractive index estimated to be 1.45) on the RWG surface induces a redshift of the resonance wavelength by 4.8 nm, see Figure 2.6-3. This structure shows a sensitivity of 0.32 nm per nm of bio-molecule attachment.

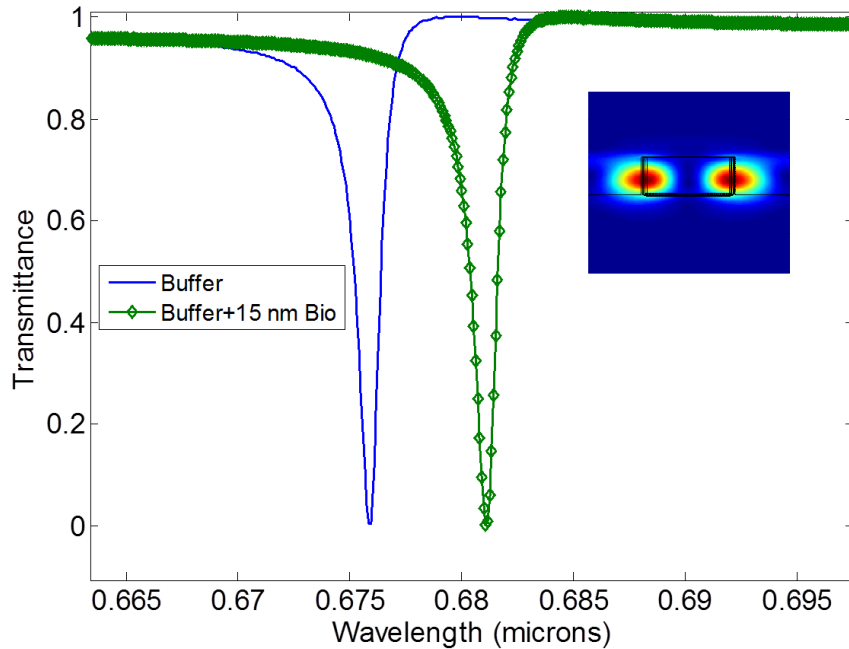


**Figure 2.6-3** Transmittance spectra of the optimized RWG at different stages of the bio-molecular detection. The E-field distribution of the resonant mode is presented inset.

## 2.7 Conclusions

The physical basis of operation of RWG is presented. A customized numerical FDTD simulator tool is developed to study and analyse the RWG as function of its physical parameters like period, filling fraction, etching depth etc. Though RWG has quite a number of parameters that it is dependent on, based on the findings from the numerical tool and understanding of how resonance is related to the RWG parameters, a simple design procedure is presented for a systemic way of designing RWG of required wavelength, sensitivity and linewidth. Sensitivity of RWG is studied in detail and categorized into bulk and surface sensitivity though the commercial sensors do not define the sensitivity in that detail. Both of these sensitivities are mostly dependent on the electromagnetic field overlap integral in the region of interest. In addition, further analytical and numerical study reveals that the bulk sensitivity is dependent on period, resonance wavelength and the effective waveguide refractive index whereas the surface sensitivity is dependent mostly on RWG etching depth, filling fraction and waveguide layer which effectively redistribute the E-field of the resonance mode across the geometry

and change the overlap integral. Considering all these finding the best RWG sensor in our context shows a bulk sensitivity of 183.3 nm/RIU and surface sensitivity of 0.32 nm shift per nm of bio-molecular attachment. As the surface sensitivity is very much defined by the presence of percentage of E-field in the detection region (~20 nm of thickness for single layer of protein biomolecule), termed as  $I_D$  in this chapter, tactical engineering of the RWG including multi-layer RWG, inclusion of metal/nanoparticle for subwavelength plasmonics confining etc. would increase the  $I_D$  value and so the surface sensitivity.



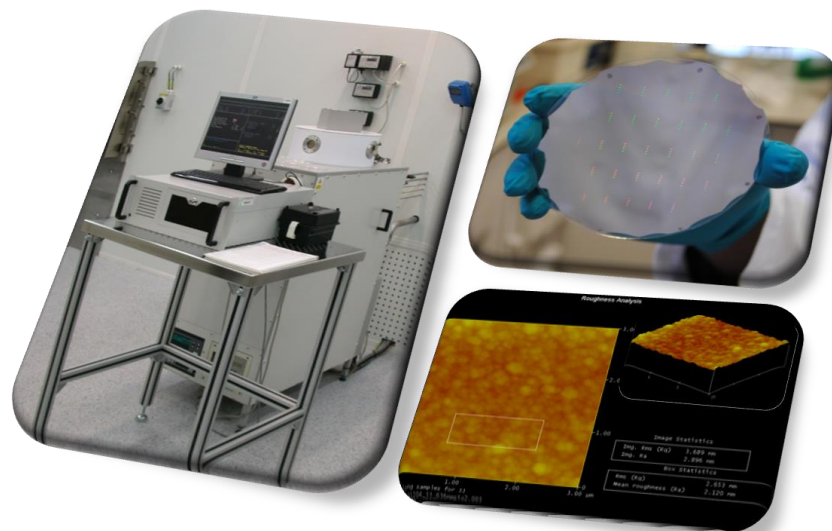
## Reference

- [1] R. W. Wood, "On a Remarkable Case of Uneven Distribution of Light in a Diffraction Grating Spectrum," *Proc. Phys. Soc. London*, p. 269, 1902.
- [2] L. Rayleigh, "III. Note on the remarkable case of diffraction spectra described by Prof. Wood," *Philosophical Magazine Series 6*, vol. 14, pp. 60-65, 1907.
- [3] U. Fano, "The Theory of Anomalous Diffraction Gratings and of Quasi-Stationary Waves on Metallic Surfaces," *Journal of the Optical Society of America*, vol. 31, pp. 213-222, 1941/03/01 1941.
- [4] A. Hessel and A. A. Oliner, "A New Theory of Wood's Anomalies on Optical Gratings," *Applied Optics*, vol. 4, p. 1275, 1965.
- [5] L. Mashev and E. Popov, "Zero order anomaly of dielectric coated gratings," *Optics Communications*, vol. 55, pp. 377-380, 1985.
- [6] S. S. Wang and R. Magnusson, "Theory and applications of guided-mode resonance filters," *Applied Optics*, vol. 32, p. 2606, 1993.
- [7] S. S. Wang, R. Magnusson, J. S. Bagby, and M. G. Moharam, "Guided-mode resonances in planar dielectric-layer diffraction gratings," *Journal of the Optical Society of America A*, vol. 7, p. 1470, 1990.
- [8] S. S. Wang and R. Magnusson, "Multilayer waveguide-grating filters," *Applied Optics*, vol. 34, p. 2414, 1995.
- [9] R. Magnusson and M. Shokooh-Saremi, "Physical basis for wideband resonant reflectors," *Optics Express*, vol. 16, pp. 3456-3462, Mar 3 2008.
- [10] R. Magnusson, "Wideband reflectors with zero-contrast gratings," *Optics Letters*, vol. 39, pp. 4337-4340, Aug 1 2014.
- [11] B. T. Cunningham, "Photonic Crystal Surfaces as a General Purpose Platform for Label-Free and Fluorescent Assays," *Jala*, vol. 15, pp. 120-135, Apr 2010.
- [12] H. Shafiee, E. A. Lidstone, M. Jahangir, F. Inci, E. Hanhauser, T. J. Henrich, *et al.*, "Nanostructured Optical Photonic Crystal Biosensor for HIV Viral Load Measurement," *Scientific Reports*, vol. 4, Feb 28 2014.
- [13] N. Orgovan, B. Kovacs, E. Farkas, B. Szabo, N. Zaytseva, Y. Fang, *et al.*, "Bulk and surface sensitivity of a resonant waveguide grating imager," *Applied Physics Letters*, vol. 104, Feb 24 2014.
- [14] D. Rosenblatt, A. Sharon, and A. A. Friesem, "Resonant grating waveguide structures," *Ieee Journal of Quantum Electronics*, vol. 33, pp. 2038-2059, Nov 1997.
- [15] P. Karvinen, "Applications of resonant waveguide gratings," Diss, Joensuu, 2010.

- [16] R. Magnusson, "Wideband reflectors with zero-contrast gratings," *Optics Letters*, vol. 39, p. 4337, 2014.
- [17] F. Deng, C. Du, and X. Luo, "Characteristic analysis of evanescent wave moiré fringes," *Journal of the Optical Society of America B*, vol. 25, p. 443, 2008.
- [18] D. M. Sullivan, "Electromagnetic Simulation Using the FDTD Method, 2nd Edition," 2013.
- [19] *Lumerical Solutions, Inc.* <http://www.lumerical.com/tcad-products/fdtd/>.
- [20] "Conformal FDTD Mesh Technology Delivers Subcell Accuracy. Retrieved from: [https://lumerical.com/support/whitepaper/fdtd\\_conformal\\_mesh\\_whitepaper.html](https://lumerical.com/support/whitepaper/fdtd_conformal_mesh_whitepaper.html)."
- [21] Z. S. Liu and R. Magnusson, "Concept of multiorder multimode resonant optical filters," *Ieee Photonics Technology Letters*, vol. 14, pp. 1091-1093, Aug 2002.
- [22] S. Boonruang, A. Greenwell, and M. G. Moharam, "Multiline two-dimensional guided-mode resonant filters," *Applied Optics*, vol. 45, pp. 5740-5747, Aug 1 2006.
- [23] A. Greenwell, S. Boonruang, and M. G. Moharam, "Control of resonance separation over a wide spectral range in multiwavelength resonant grating filters," *Applied Optics*, vol. 46, pp. 6355-6361, Sep 1 2007.
- [24] R. Magnusson, "Spectrally dense comb-like filters fashioned with thick guided-mode resonant gratings," *Optics Letters*, vol. 37, pp. 3792-3794, Sep 15 2012.
- [25] I. D. Block, N. Ganesh, M. Lu, and B. T. Cunningham, "A Sensitivity Model for Predicting Photonic Crystal Biosensor Performance," *IEEE Sensors Journal*, vol. 8, pp. 274-280, 2008.
- [26] J. Robinson and Y. Rahmat-Samii, "Particle swarm optimization in electromagnetics," *Ieee Transactions on Antennas and Propagation*, vol. 52, pp. 397-407, Feb 2004.
- [27] Z. Hegedus and R. Netterfield, "Low sideband guided-mode resonant filter," *Appl Opt*, vol. 39, pp. 1469-73, Apr 1 2000.
- [28] M. El Beheiry, V. Liu, S. Fan, and O. Levi, "Sensitivity enhancement in photonic crystal slab biosensors," *Optics Express*, vol. 18, p. 22702, 2010.

# Chapter 3

## Fabrication of Optical Nano-structure



## 3.1 Introduction

**F**or decades, micro- and nanolithography technology has been contributed to the manufacturing of integrated circuits (ICs) and microchips creating patterns with a feature size ranging from a few nanometers up to tens of millimeters. The term ‘micro-’ and ‘nano-fabrication’ were coined based on the achievable minimum feature size of the targeted layout pattern. As the feature size of all the proposed sensors presented in the previous chapter are submicron and densely packed, a nanolithography technique is developed and implemented for the specific device material and substrate of interest. In general, the nanolithography technique can be superficially divided into two categories based on its throughput. Photolithography, laser interference lithography and nano-imprint lithography would fall into the high throughput section because of their ‘do-at-once’ nature whereas E-beam lithography (EBL) and focused ion beam (FIB) lithography are likely to be in the low throughput part as they function in a serial fashion. The EBL technique allows an ultrahigh-resolution patterning of any arbitrary shapes with a minimum feature size as small as a few nanometers but the throughput of this type is limited by its slow serial nature which makes it inappropriate for mass production.

In this chapter at first different lithography techniques are introduced under Sections 3.1.1-3.1.4 with their pros and cons. A comparative study of the different techniques is tabulated in Table 3.1-1. The fabrication schemes chosen to make the sensor chips are discussed in Section 3.2. The development of low loss Silicon nitride ( $\text{Si}_x\text{N}_y$ ) waveguide material is detailed in Section 3.3. Specifically, Plasma enhanced chemical vapor deposition (PECVD) process parameters e.g., precursor gas composition, plasma frequency, pressure etc. are studied in detail in Section 3.3.5 to reduce the optical loss of the deposited  $\text{Si}_x\text{N}_y$  film. Surface roughness measurements of the developed films are presented in Section 3.3.7 and the waveguide loss measurement experiments are shown in Section 3.3.6. The refractive index measurement of the selected low loss  $\text{Si}_x\text{N}_y$  film is measured by Ellipsometry as shown in Section 3.3.8. However, both EBL and nano-imprint are exploited separately as nano-patterning techniques which are presented in detail in Section 3.4 and 3.5 respectively. The Cr dry-etching recipe is developed for

transferring the EBL and nano-imprinted pattern; corresponding results are discussed in Section 3.6. Then, the procedure of transferring the pattern and dicing of the wafer into the  $\text{Si}_x\text{N}_y$  sensor chips with alignment mark are shown in Section 3.7 and 3.8 respectively. The proposed nano-patterning technique using Cr as hard mask can achieve very high aspect ratio, tens of nanometer narrow lines on insulating substrate which is presented in Section 3.9. The chapter is then concluded discussing about the fabrication achievements and future prospects.

### 3.1.1 Photolithography

Photolithography is a process used in micro-fabrication for perfect replication of custom designed pattern in a thin film on a substrate. It is also termed as optical lithography or UV lithography. This branch of lithography utilizes templates, also known as photomasks, which has transparent and opaque areas done by patterning thin Chromium film on glass or Quartz plate. Based on the required resolution of the pattern, UV or deep UV light is shone through the photomask to the spin coated thin film of photo-sensitive resist on top of the substrate. The light exposed area of the photoresist transforms into soluble (positive photoresist) or non-soluble (negative photoresist) depending on the chemistry of the photoresist. The soluble portion is then washed away by using photoresist specific solvent called developer. Light replicates patterns from photomask to the photosensitive film which is then used as local mask for further steps taken to transfer the copied patterns to the substrate.

In the early 1970s, the required dimensions for the ICs were from 2  $\mu\text{m}$  to 5  $\mu\text{m}$ . Replication of these patterns was simply achieved by using mercury arc based UV-light and by bringing photomask and substrate in close proximity or into contact during the exposure. Systems based on this operating principle are still used today in microfabrication due to their simplicity, relatively low cost, high throughput and good process quality. These systems, called UV-contact mask aligner, can reach resolutions from a few micrometers to sub half micron level, depending on the exposure wavelength and the contact method. With fully automated systems the throughput can exceed 100 wafers per hour (wph) and reach an overlay accuracy of  $< 1 \mu\text{m}$  [95] [96].

However, more complex exposure systems are exploited for the increasing demand of lower pattern linewidth. Immersion lithography (i.e., using a liquid in the space between the lens and substrate in order to increase the numerical aperture), a recent innovation, has allowed the minimum feature size to be reduced to 32 nm in 2010 without the requirement for Extreme UV sources. The 32 nanometer (32 nm) node (average half pitch of a memory cell) was launched by Intel and AMD in 2010 following the 45 nanometer process in CMOS semiconductor device fabrication industry. Both of them produced commercial microchips using the 32 nanometer process in the early 2010s. Intel began selling its first 32 nm processors using the Westmere architecture on 7 January 2010. This was done by using deep-UV ArF-light sources operating at 193 nm wavelength and exposing patterns using immersion scanners, phase shift masks and double exposure schemes. Exposure was based on an image reduction technique that projected the photomask onto the substrate and simultaneously reduced the size of the patterns many times. This allowed the photomasks to be fabricated with looser tolerances than the final pattern. These systems were also very productive and able to pattern more than one hundred and fifty 300 mm wafers per hour [97]. The 32 nm process was superseded by commercial 22 nm technology in 2012 [98].

These photolithography systems capable of reaching 32 nm or even 22 nm linewidths, cost tens of millions of euros and thus make these instruments economically viable only for very high volume production. For these reasons such instruments can only be owned by large IC-manufacturers. As feature linewidths get smaller the cost of nanofabrication using optical lithography grows rapidly and hence, research and utilization of alternative techniques is tempting.

### **3.1.2 Focused ion beam lithography (FIB)**

Focused-ion beam lithography utilizes an accelerated ion beam (typically gallium ion) to directly punch a film on the substrate by removing material through ion bombardment [99]. This is possible due to the heavy mass of ions as compared to that of electrons. A focused ion beam can write patterns into a photoresist layer or directly onto the substrate.

Furthermore, focused ion beam systems are also employed for depositing materials such as tungsten, platinum, and carbon via ion beam induced deposition. When a precursor gas such as tungsten hexacarbonyl ( $W(CO)_6$ ) is added into the chamber, the precursor gas is hit by the focused-ion beam leading to gas decomposition which leaves a non-volatile component (tungsten) on the surface .

Its main limitation however, is the processing time involved to machine large structures: it is clear that the FIB deposition and etching rates are low. Dimensions up to some tens of micrometres are easily feasible, but above 100  $\mu m$ , the typical processing times become unacceptably high, and it is better to use other techniques.

Another limitation is the charging of the sample and drifting of the ion beam for insulating substrate. Of course, any work involving charged particle beams and electrically insulating materials in a vacuum is prone to the effects of charging and same happens to FIB patterning. Various means have been developed to alleviate the problem of charge-induced ion beam drift by supplying a source of negative charge, e.g. the electron flood gun, simultaneous electron and ion beam scanning [100].

FIB processes also induce some damage in the samples. The expected damage caused by the ion beam includes implantation of gallium ions, amorphization of crystalline structures and loss of fine structural detail.

### **3.1.3 Electron beam lithography**

Electron beam lithography (EBL) has been the main techniques for fabricating nanoscale patterns. Instead of Gallium ion bombardment used in FIB, EBL [101, 102] utilizes an accelerated electron beam focusing on an electron-sensitive resist [103, 104] to make an exposure. With couple of nanometer spot diameter, the focused electron beam scans dot by dot on the surface in sequence to create the pattern. A typical EBL system closely resembles a SEM. The main difference between a SEM and an EBL is that in SEM, the beam is raster scanned over the sample in order to collect secondary electrons to form an image while in an EBL the beam is scanned onto the sample according to the instructions coming from the pattern generator. In terms of specifications, the resolution of electron beam lithography techniques are of the order of 5 – 20 nm [105] due to ultra-short wavelengths of electron beams in the order of a few nanometers.

Though the intrinsic resolution of the electron beam writing in the resist is as small as 3 to 5 nm at high incident electron energy, practical resolution is limited by the development of the resist after exposure and by successive pattern transfer protocol. However, the lack of throughput limits their applications within research and mask fabrication.

At this point, it would be good to introduce few terms used in EBL lithography like ‘writing field’, ‘stitching’ and ‘exposure doses’. *Writing field* is the largest area exposed without the stage moving, with typical dimensions ranging from few tens of microns to few millimeters defined by the expected resolution of the system and EBL system configuration. *Stitching* happens when the pattern dimensions are such that the exposure needs more than one writing field. Then the fields are stitched together via stage movements. The accuracy of stitching depends on the quality of the stage, the stability of the system and its environment i.e., temperature, humidity and acoustic noise control, and also on the specific software implemented, which can compensate different types of drifts [105]. And, *Exposure dosage* is the amount of energy deposited per unit area. The dosage is actually measured in terms of current deposited per unit area,  $\mu\text{C cm}^{-2}$ . The dosage at which each exposure is run depends chiefly on the resist used, and the density and dimension of the pattern being written.

### 3.1.4 Nano-imprint lithography

The nano-imprint lithography (NIL) process is a mechanical replication process where surface reliefs from the template are embossed into a thin layer on the substrate by mechanical force. There are two versions of NIL: thermoplastic NIL in which thermoplastic polymers are thermally embossed and the other is based on UV-curable polymers known as photo NIL. In thermoplastic NIL, resist (thermoplastic polymer) is spin coated on sample substrate. The mold which has predefined topography is then mechanically pressed together with the sample substrate at a temperature higher than the glass transition temperature of the resist. So, the resist becomes soft and follows the surface topography of the mold. The resist takes inverse shape of the pre-patterned mold. The system is then cooled down and the mold is separated from the sample substrate and thus, the resist layer gets patterned by the mold. Reactive ion etching (RIE) or inductively coupled plasma (ICP) etching is normally used to transfer the pattern from the resist to



the material underneath. On the other hand, photo NIL utilizes UV curable liquid resist on the mold which is normally made of fused silica. While the mold and the substrate are being pressed together, the resist is cured in UV light through the transparent silica mold. Because of UV curing, the resist become solid and is shaped into inverse of the mold's surface topography. After mold separation, a similar pattern transfer process (RIE/ ICP etching) can be used to transfer the pattern in resist onto the underneath material. Please see Section 3.5 for detail of the photo NIL process.

In principle, NIL does not have any limitations in pattern geometry, therefore NIL can copy any patterns produced by EBL or by other techniques. The NIL process and imprint instrument are conceptually very simple, but allow extremely good resolution and a relatively fast replication process [95].

**Table 3.1-1 Specifications and applications of the major nano-lithography techniques [101].**

<b>Lithography Technique</b>	<b>Minimum Feature Size</b>	<b>Throughput</b>	<b>Applications</b>
Photolithography (contact & proximity printings)	2-3 $\mu\text{m}$ [102]	very high	typical patterning in laboratory level and production of various MEMS devices
Photolithography (projection printing)	a few tens of nanometers (37 nm) [106]	high – very high (60-80 wafers/hr) [107]	commercial products and advanced electronics including advanced Ics [107], CPU chips
Electron beam lithography	< 5 nm [105]	very low [107, 108] (8 hrs to write a chip pattern) [107]	Masks [108] and Ics production, patterning in R&D including photonic crystals, channels for nanofluidics [105]
Focused ion beam lithography	20 nm with a minimal lateral dimension of 5 nm in semiconductor substrate [106]	very low [108]	patterning in R&D including hole arrays [109, 110], bulls-eye structure [111], plasmonic lens [112]
Nanoimprint lithography	6-40 nm [113, 114]	high (> 5 wafers/hr) [107]	bio-sensors [115], bio-electronics [113], LOCs: nano channels, nano wires [116, 117]

## 3.2 Fabrication schemes to make the sensor chips

The resonant waveguide grating (RWG) sensor (proposed in previous chapter) is an array of subwavelength gratings of period 450 nm covering an sensing area of  $500\ \mu\text{m} \times 500\ \mu\text{m}$  each. A sensor chip of size  $1.5\ \text{cm} \times 1\ \text{cm}$  is designed to have 4 RWG sensors separated at fixed distances aligned with the micro-fluidic channel of the bio-characterization setup. Wafer scale sensor chips production was attempted with 100 mm diameter glass wafer. Each of the wafers was planned to contain 33 sensor chips each of which had 4 RWG sensors with proper alignment mark included for successive bio-characterization (photo deprotection for region specific biomolecular attachment).

Though the projection photolithography systems are capable of reaching 22 nm linewidths (**Table 3.1-1**) which is far better than the minimum feature size of the RWG sensor, it cost tens of millions of Euros and thus makes these instruments economically viable only for very high volume industry based production. Direct writing by FIB milling on a large area ( $500\ \mu\text{m} \times 500\ \mu\text{m}$  for the proposed sensor) is a bit challenging for insulating glass substrate. The charged Gallium ions get trapped while milling on the insulating  $\text{Si}_x\text{N}_y$  layer. So, the exposed area gets charged and repels the incoming ions which cause the drifting of the beam and distorts the pattern to be written. A thin conducting charge dissipating layer on top of the insulating substrate and grounding of the sample may facilitate patterning on insulating substrate. However, as FIB is a serial direct writing procedure, it takes long time for making the whole structure by deep etching of the pattern as desired for the proposed RWG sensor. So, the FIB lithography can be a candidate for making a single RWG sensor but not feasible at all for the 100 mm full wafer scale production where more than hundred of this sensors are to be written in each wafer.

EBL is also a serial process similar to FIB but it only patterns the ebeam resist instead of making the whole structure as done in FIB by time consuming direct milling into the material. In EBL only the pattern is written by electron beam and the full wafer etching is done by single step dry etching procedure. So, the throughput of EBL patterning is much higher than that of FIB in this case. On the other hand, nano-imprint lithography looks quite promising because of its very high throughput and low cost. So, the wafer scale

fabrication of the RWG sensor is studied for both EBL and nano-imprint lithography in Tyndall National Institute and VTT respectively. The flow chart shown below gives an idea of the process routes followed for fabricating RWG sensor chips in large numbers.

### 3.2.1 Flow chart and schematic of the nano-fabrication process steps

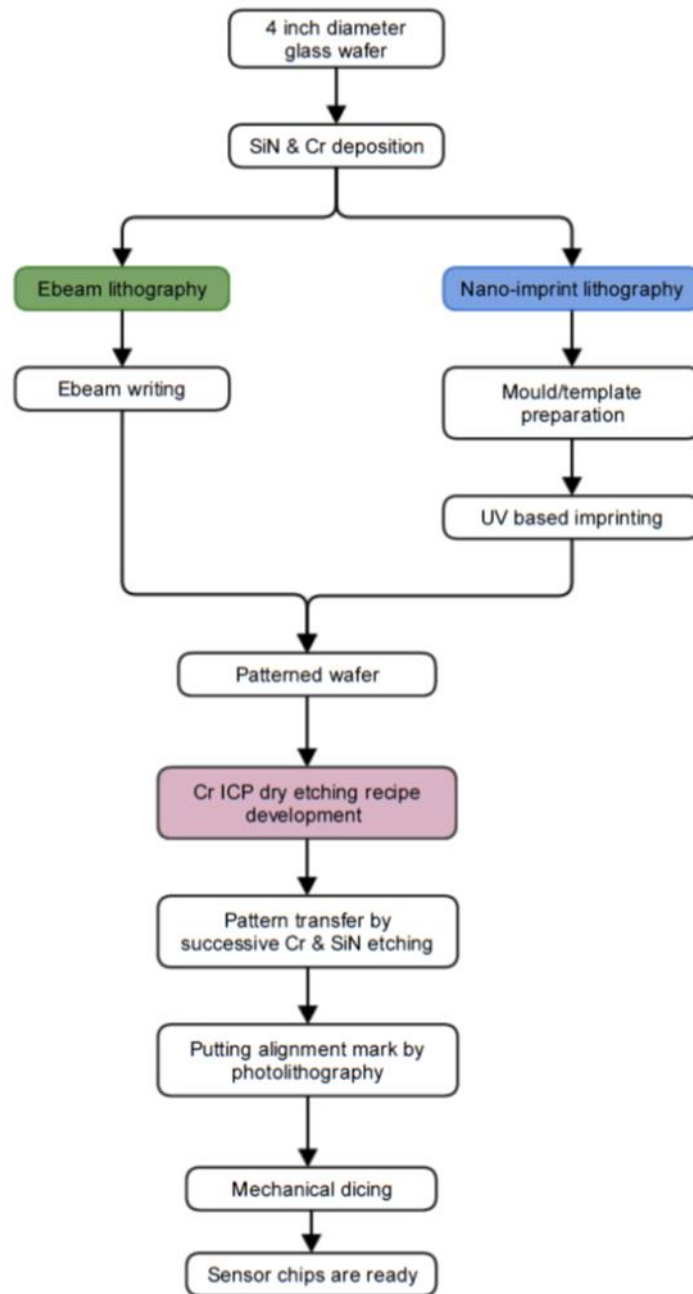
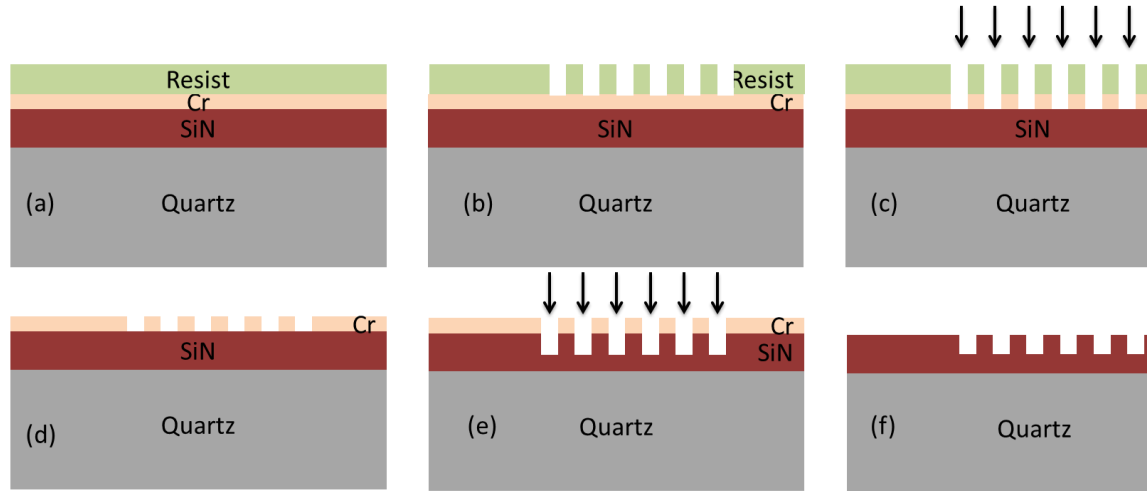


Figure 3.2-1 Flow chart of the nano-fabrication process steps.

The schematic of the RWG sensor wafer level patterning process steps on glass substrate is illustrated in Figure 3.2-2. Having transferred the pattern into the  $\text{Si}_x\text{N}_y$  layer as shown in step (f) of Figure 3.2-2, another level of photolithography is done for putting the alignment mark in each sensor chip. Then the processed wafer is diced into separate sensor chips.



**Figure 3.2-2** The starting quartz wafer has Cr deposited on  $\text{Si}_x\text{N}_y$  (a) ebeam/nanoimprint resist is spun on (b) EBL pattern is written in resist, (c) pattern is transferred to the Cr layer by ICP dry etching, (d) removal of the resist, (e) transfer of the pattern into the  $\text{Si}_x\text{N}_y$  layer by ICP dry etching and (f) removal of the Cr.

### 3.3 Development of $\text{Si}_x\text{N}_y$ Material

As mentioned in the ‘Design’ chapter that  $\text{Si}_x\text{N}_y$  layer on glass substrate is considered as the material platform for the proposed GMR and nano-ribbon cavity.

Low Pressure Chemical Vapour Deposition (LPCVD) technique could be a prospective option for Silicon nitride ( $\text{Si}_3\text{N}_4$ ) because of its very low optical loss ( $\sim 0.2$  dB/cm [118]). Unfortunately, its large internal tensile stress limits the maximum layer thickness to  $< 350$  nm not suitable for the proposed RWG of thickness 400 nm. Moreover, the high LPCVD process temperature ( $\sim 800^\circ\text{C}$ ) is not compatible to the glass substrate of interest. On the other hand, plasma enhanced chemical vapour deposition (PECVD) is a low-temperature process ( $\sim 300^\circ\text{C}$ ), making it suitable for glass substrate and enables thicker film deposition with lower material stress, but with comparatively higher optical loss ( $\sim 0.7$

dB/cm [119]). Therefore, a process for low-loss  $\text{Si}_x\text{N}_y$  waveguides using PECVD was developed as part of this thesis work.

### 3.3.1 $\text{Si}_x\text{N}_y$ deposition techniques

Both PECVD and LPCVD techniques were carried out as part of this thesis work for depositing  $\text{Si}_x\text{N}_y$  film. LPCVD was done at high temperature ( $800^\circ\text{C}$ ) whereas PECVD was carried out at lower temperature ( $300\text{-}500^\circ\text{C}$ ). It is mentioned in [120-123] that the LPCVD deposition technique produces lower H-content in the  $\text{Si}_x\text{N}_y$  film than that of the PECVD deposited film. The disparity in H-content in between LPCVD and PECVD is mostly because of their associated process temperature, since at high temperature both Si-H and N-H bond in Silane and Ammonia respectively can easily be broken with high kinetic energy and so produces  $\text{Si}_x\text{N}_y$  films with lower H-content. As the optical waveguide loss of the  $\text{Si}_x\text{N}_y$  thin film in the IR and near IR region is mostly because of the incorporation of the H content in the  $\text{Si}_x\text{N}_y$  film [124], the LPCVD stoichiometric  $\text{Si}_3\text{N}_4$  has been reported with lower loss than PECVD  $\text{Si}_x\text{N}_y$  [122]. Many published works [124, 125] have already been reported in literature that this loss in the IR region can be reduced by optimizing the plasma parameters in the PECVD process. Though there is literature available for the IR region, it is little available in the visible light region to reduce the optical waveguide loss of  $\text{Si}_x\text{N}_y$  film. So, to improve the waveguide loss of the  $\text{Si}_x\text{N}_y$  material in the visible region, the role of the precursor gas ratio ( $\text{NH}_3\text{:SiH}_4$ ) and other plasma parameters like plasma frequency, pressure, and temperature were investigated as part of this thesis work and presented in this chapter.

### 3.3.2 Silicon-dioxide as an optical isolation

The experiments of developing a low loss  $\text{Si}_x\text{N}_y$  recipe were done on Si substrate which absorbs the whole visible and near infrared spectrum of light (wavelength  $< 1000\text{ nm}$ ). A thick layer of PECVD Silicon-dioxide ( $\text{SiO}_2$ ) was chosen as an optical isolation layer in between the  $\text{Si}_x\text{N}_y$  layer and the Si substrate. For  $\text{Si}_x\text{N}_y$  layer thickness of  $275\text{ nm}$  ( $\sim$  average thickness) and  $\text{SiO}_2$  optical isolation thickness of  $300\text{ nm}$ , the simulated propagating mode decays while travelling along the waveguide as shown in Figure [3.3-1a&c](#).

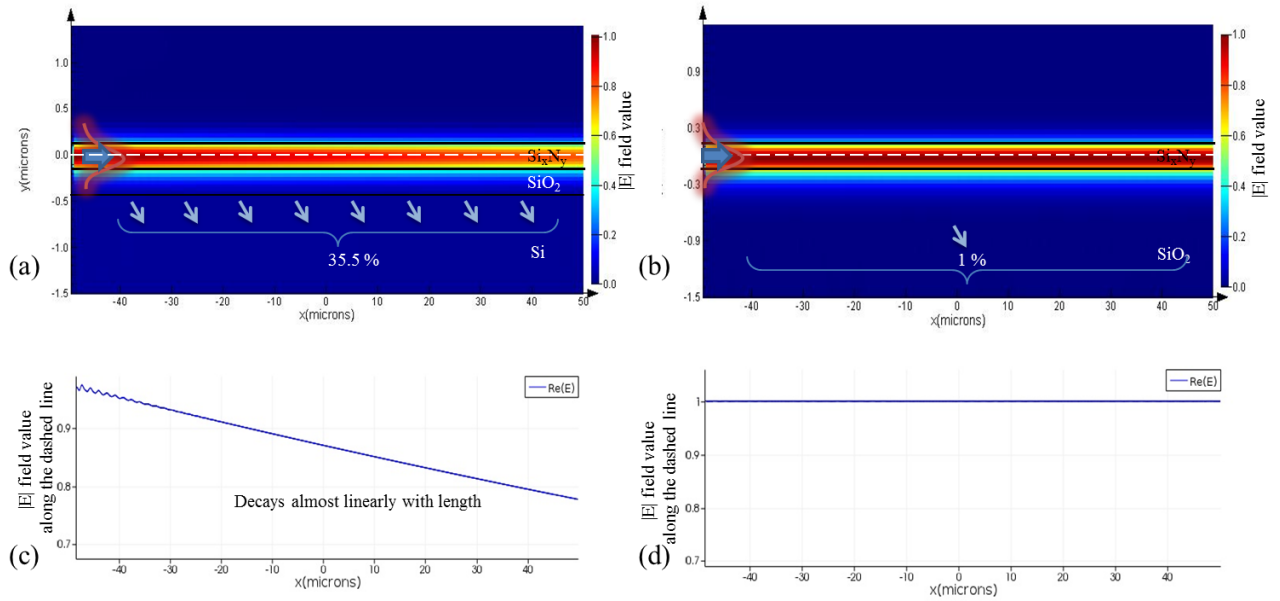


**Figure 3.3-1 Leakage of optical mode to the Si substrate while propagating. Electric field distribution of the propagating mode optically isolated by  $\text{SiO}_2$  layer of thickness (a) 300 nm, and (b)  $2\ \mu\text{m}$ . Decay of the  $|E|$  field along the dashed line (center of the waveguide) for  $\text{SiO}_2$  thickness of (a) 300 nm, and (b)  $2\ \mu\text{m}$ .**

About 35.5% of the launched guided light is leaked to the Si substrate and thus absorbed. For  $2\ \mu\text{m}$  thick  $\text{SiO}_2$  optical isolation there is almost no leakage to the Si substrate as shown in Figure 3.3-1b&d. In order to maintain a good quality optical isolation, a  $2\ \mu\text{m}$  thick  $\text{SiO}_2$  layer was deposited on the silicon substrates by PECVD before depositing the  $\text{Si}_x\text{N}_y$  layer.

### 3.3.3 LPCVD $\text{Si}_x\text{N}_y$

The LPCVD method used Dichlorosilane ( $\text{SiCl}_2\text{H}_2$ ) and ammonia ( $\text{NH}_3$ ) precursor gases at flow rate of 20 standard cubic centimeters per minute (sccm) and 60 sccm respectively to deposit a high quality silicon nitride film. The deposition was performed at a high temperature of  $800^\circ\ \text{C}$  for the reactions to occur. This high deposition temperature was not compatible with typical glass substrate and so, the film was grown on  $\text{SiO}_2$  with Si substrate. The deposition rate of the LPCVD  $\text{Si}_3\text{N}_4$  was 30.3 nm/min.

### 3.3.4 PECVD $\text{Si}_x\text{N}_y$

PECVD uses radio frequency energy to create a plasma from the precursor molecules. Then, the precursor molecules go through chemical reactions to form the film. In the recipe developed0, the precursor gases used for depositing silicon nitride were  $\text{SiH}_4$ ,  $\text{NH}_3$  and  $\text{N}_2$ . The chemical composition of the film was controlled by the  $\text{NH}_3$  and  $\text{SiH}_4$  precursor gas ratio, which in turn affected the refractive index and also the optical absorption of the film. However, the deposited film was non-stoichiometric and contained hydrogen [126, 127] instead of forming pure  $\text{Si}_3\text{N}_4$ . The higher H content in the PECVD film change its characteristics e.g., lower film density, higher etch rate, lower thermal stability etc. compared to the LPCVD grown  $\text{Si}_3\text{N}_4$ .

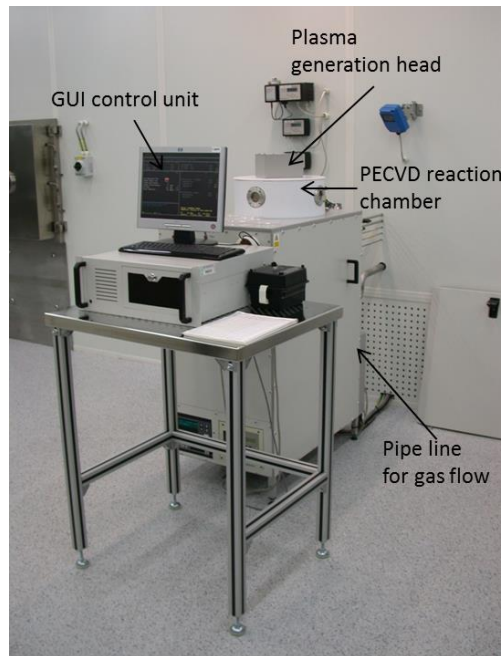


Figure 3.3-2 PECVD system at the Tyndall's III-V cleanroom.

### 3.3.5 Deposition

I used the PECVD machine (STS manufacturing Inc.) to deposit the  $\text{Si}_x\text{N}_y$  film with variation in different process parameters e.g., precursor gas composition, plasma



frequency, pressure etc. The  $\text{Si}_x\text{N}_y$  deposition was done on Si wafers with  $2\mu\text{m}$  thick optical isolation layer (Section 3.3.2). This PECVD system used a *Mixed Frequency* deposition technique (combination of both lower frequency at 187 kHz and higher frequency at 13.56 MHz) with a  $\text{SiH}_4$ ,  $\text{NH}_3$  and  $\text{N}_2$  precursor gasses of 40, 40 and 1960 sccm in a low pressure  $\text{N}_2$  background at  $300^\circ\text{C}$  to get low stress film for electrical isolation. The thin  $\text{Si}_x\text{N}_y$  film developed using the aforementioned PECVD configuration resulted a waveguide loss of  $4\text{ cm}^{-1}$  (loss calculation technique is presented in Section 3.3.6), which was too high to form optical waveguides of couple of millimeter long nano-ribbon (please see Section 7.4). It had been reported in the literature that losses could be reduced by employing only a low frequency process and by increasing the ratio of  $\text{NH}_3$  to  $\text{N}_2$  during deposition [128, 129]. So, separate experiments were carried out at two different low frequencies: 187 kHz (Tyndall III-V cleanroom) and 380 kHz (Tyndall Silicon MEMs laboratory) as shown in Table 3.3-1.

**Table 3.3-1 Controlled variation of PECVD process parameters**

Exp. No.	Frequency (kHz)		Pressure (mTorr)	Gas Mixture $\text{N}_2/\text{SiH}_4/\text{NH}_3$ (sccm)	Temp ( $^\circ\text{C}$ )	Power (Watt)	Thickness (nm)	Loss ( $\text{cm}^{-1}$ )
1	Mixed frequency	187 kHz + 13.56MHz	900	1960/40/40	300	60	240	4
2	Single frequency	380 kHz	550	1960/40/20	300	60	290	0.34
3		380 kHz	550	1960/20/40	300	60	276	0.09
4		380 kHz	550	1960/10/40	300	60	276	0.2
5		187 kHz	650	1960/10/40	300	60	325	0.2
6		187 kHz	650	1960/7/43	300	60	315	0.2

The process pressure and precursor gasses composition ( $N_2:SiH_4:NH_3$ ) were varied to minimize the optical waveguide loss of the  $Si_xN_y$  thin film. The best PECVD  $Si_xN_y$  film showed an optical waveguide loss of  $0.09\text{ cm}^{-1}$  (Exp. No. 2 in the table) which is equivalent to  $0.387\text{ dB/cm}$  compared well with the work in [119].

### 3.3.6 Waveguide loss characterization

The waveguide loss of the films was estimated by imaging the decrease in scaled intensity of light propagating through the  $Si_xN_y$  slab waveguide. The decrease in intensity was imaged using a camera and the trend of decreasing was fitted with an exponential curve which gave the waveguide loss ( $\alpha$ ) in  $\text{cm}^{-1}$  using the equation:

$$I = I_0 e^{-\alpha L} \quad (3.1)$$

where,  $I_0$  is the initial intensity,  $I$  is the decreased intensity after travelling a length of  $L$  cm. An exponential fit was used to estimate the value of the loss ( $\alpha$ ). The schematic of the experimental optical loss characterization setup is shown in Figure 3.3-3.

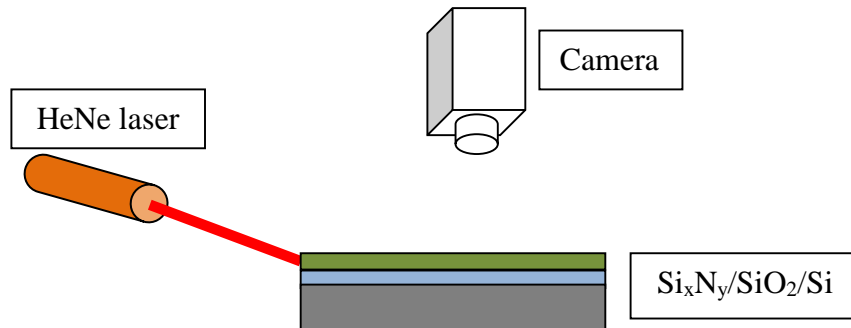


**Figure 3.3-3 Setup for estimation of  $Si_xN_y$  film optical loss.**

Light of wavelength of  $633\text{ nm}$  was coupled into the  $Si_xN_y$  waveguide layer by free space coupling from the He-Ne laser. The coupled light travelled upto a certain length based on the optical loss of the  $Si_xN_y$  material. The propagation length was measured tracking the drop in intensity of the light scattering from the  $Si_xN_y$ 's top surface.

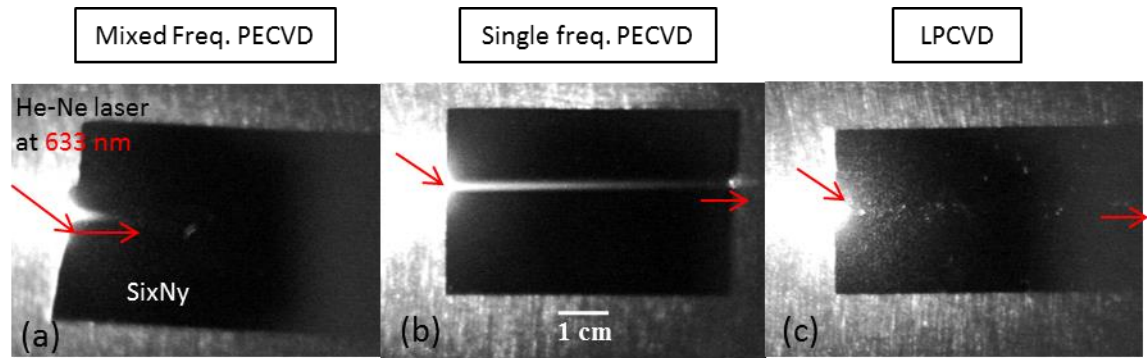


**Figure 3.3-4 Propagation length of  $\text{Si}_x\text{N}_y$  thin film waveguide deposited by (a) Mixed Frequency PECVD, (b) single frequency PECVD, and (c) LPCVD.**

The differences in propagation lengths ( $\propto 1/\text{waveguide-loss}$ ) for different deposition techniques are evident from Figure 3.3-4. The light scattered from the mixed frequency PECVD waveguide (Figure 3.3-4a) had a higher decay than that of the single frequency PECVD film (Figure 3.3-4b). The absence of scattered light in the LPCVD film in Figure 3.3-4c is due to better quality (smoother top surface) of the LPCVD film as compared to the PECVD deposited films. Figure 3.3-5 shows the exponential curve-fitting for the decaying light intensity of the mixed and single frequency PECVD film along the length of light propagation. Switching the PECVD system from mixed to single frequency mode reduced the optical loss from  $4 \text{ cm}^{-1}$  to  $0.6 \text{ cm}^{-1}$ . It was also noted that the loss also decreased with increasing waveguide thickness, therefore similar waveguide thicknesses were compared to give correct comparison of loss.

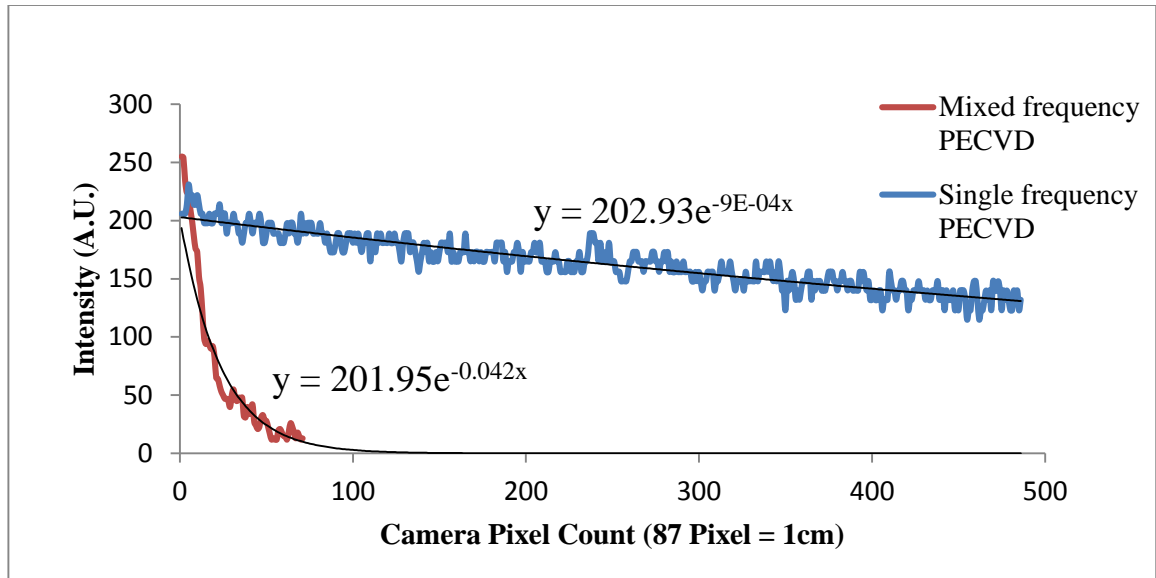


**Figure 3.3-5** The guided light (Figure 3.3-4a&b) decays exponentially at different rate for mixed and single frequency PECVD  $\text{Si}_x\text{N}_y$  films.

It had been observed that the deposition of a thin layer (e.g., 350 nm) of  $\text{SiO}_2$  on top of the  $\text{Si}_x\text{N}_y$  films reduced the loss to half of its original value, most likely due to the decrease in index contrast (from  $\text{Si}_x\text{N}_y \rightarrow \text{Air}$  to  $\text{Si}_x\text{N}_y \rightarrow \text{SiO}_2$ ) which reduced the surface roughness induced light scattering effect. The waveguide loss ( $\propto$  surface roughness) associated with the 187 kHz PECVD deposited films did not improve significantly with changes in plasma parameters (see experiment no. 4 & 5 in Table 3.3-1), therefore PECVD deposition was also tested in a different PECVD system which used 300 kHz (instead of 187 kHz) of low frequency plasma source. A slab waveguide loss of  $0.09 \text{ cm}^{-1}$  was achieved in the 300 kHz system for gas composition of  $\text{N}_2$ ,  $\text{SiH}_4$ ,  $\text{NH}_3 \equiv 1960, 20, 40$  sccm and pressure of 550 mTorr (Experiment no. 2 in Table 3.3-1). This was deemed as an acceptable slab waveguide loss for the sensor application because the proposed RWG (chapter 2) is of sub-millimeter size and the nano-ribbon waveguide (chapter 6) is of couple of millimeter size in length. However, no further reduction of loss was achieved by changing the PECVD process pressure, temperature or RF power. The deposition rate of the PECVD  $\text{Si}_x\text{N}_y$  was measured as 13 nm/min.

### 3.3.7 Surface roughness measurement

The surface roughness of mixed and single frequency PECVD, and LPCVD  $\text{Si}_x\text{N}_y$  films were measured by AFM as shown in Figure 3.3-6 which confirmed the smoother surface of the single frequency PECVD and the LPCVD film compared to the mixed frequency PECVD  $\text{Si}_x\text{N}_y$  film. The RMS roughness of the mixed frequency PECVD, single frequency PECVD and LPCVD  $\text{Si}_x\text{N}_y$  films are 3 nm, 0.5 nm and 0.3 nm respectively.

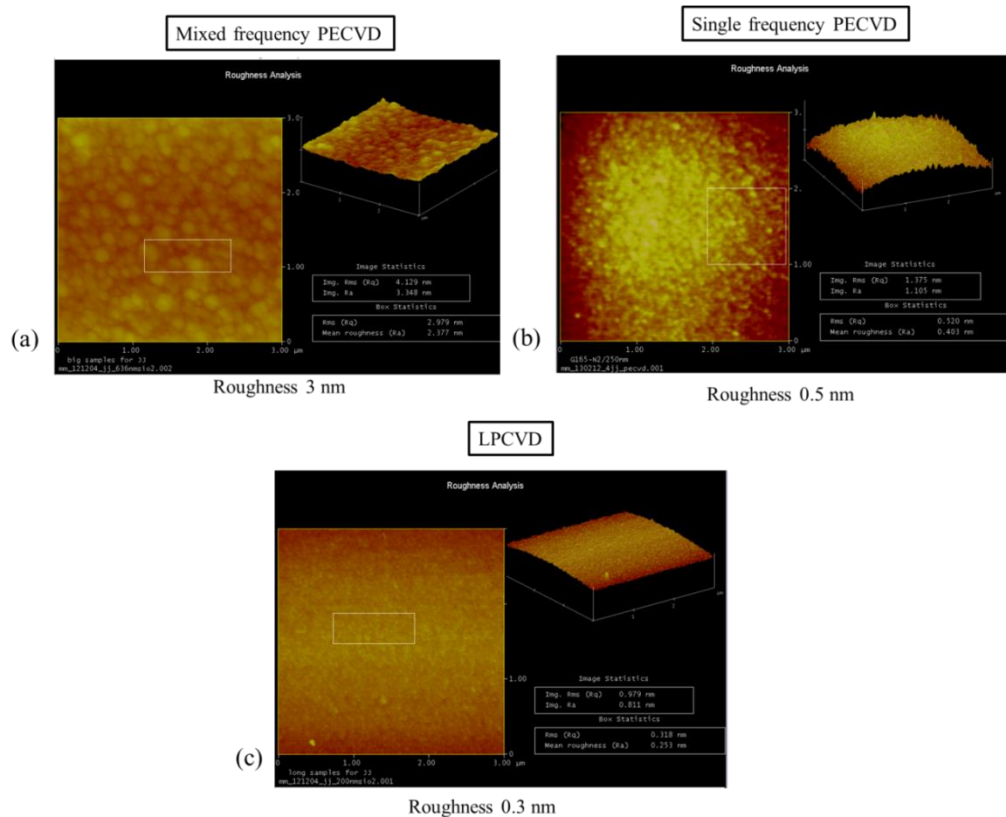


**Figure 3.3-6 Surface roughness measurements by AFM (a) RMS roughness = 3 nm for PECVD (Mixed Frequency), (b) 0.5 nm for single frequency PECVD and (c) 0.3 nm for LPCVD  $\text{Si}_3\text{N}_4$  depositions.**

Despite better smoothness and apparent lower loss, LPCVD films could not be used with “glass” substrates in my project (Phast-ID [51]), because of very high deposition temperature of LPCVD process, approximately  $800^\circ\text{C}$ . Such a high temperature would cause huge stress in the glass substrates. However, the single frequency PECVD (Exp. No. 2 in Table 3.3-1) showed roughness of only about 0.5 nm resulting a low waveguide loss of  $0.09\ \text{cm}^{-1}$  which is good enough for the desired sensor application.

### 3.3.8 Refractive index measurement

Normally, Ellipsometry measures the change of polarization of light upon reflection from the sample and compares it with a model to determine the thickness, refractive index and few other properties of the sample material. The thickness and refractive index of the thin  $\text{Si}_x\text{N}_y$  film were measured using Woolam M2000 ellipsometer (Figure 3.3-7). A fit to the experimental value using the Cauchy dispersion model yielded the best result for the refractive index and thickness. The measured thickness determined by the Cauchy model compared well with the ‘Stylus Profilometer’ thickness measurement.

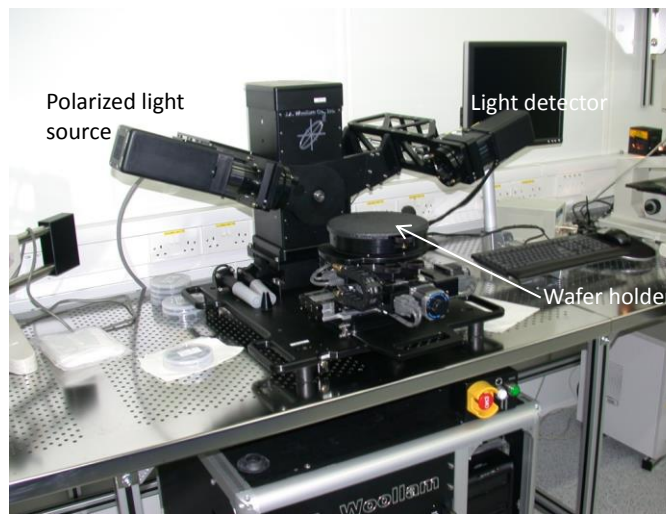


**Figure 3.3-7 Ellipsometer used to characterize optical properties of the developed  $\text{Si}_x\text{N}_y$  film.**

The extracted refractive index values of the low loss  $\text{Si}_x\text{N}_y$  film are plotted in Figure 3.3-8. Because of the dispersion of the material, the refractive index value decreases with increase in wavelength.

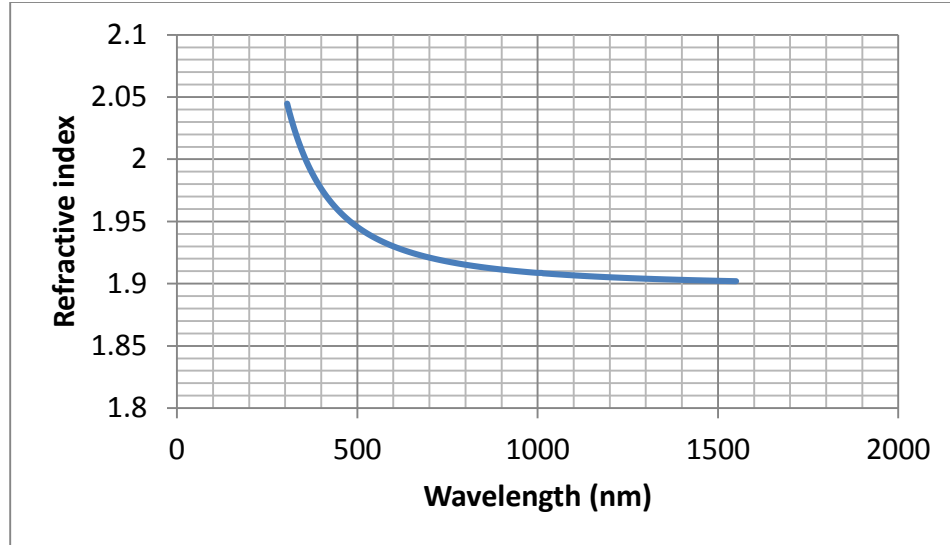


Figure 3.3-8 Measured refractive index of PECVD  $\text{Si}_x\text{N}_y$ .

### 3.4 EBL patterning processes

The fabrication of  $\text{Si}_x\text{N}_y$  nanostructures on semiconductor Si substrate have mostly relied on electron beam lithography (EBL) of a suitable resist followed by dry etching to transfer the pattern. However, glass (quartz) substrates are insulating and therefore they need a discharging mechanism during the EBL writing, otherwise a distortion in the patterned nanostructures can be observed. In [130] a water soluble conductive polymer was used as a charge dissipating layer which was removed after the EBL. However,  $\text{Si}_x\text{N}_y$  generally exhibits poor etch selectivity with EBL resists which degrade the transferred pattern by, for example, sloped sidewalls that greatly reduce the quality (Q) factor of resonant cavity based devices [131]. Furthermore, the etching depth of  $\text{Si}_x\text{N}_y$  RWGs is limited due to the thin EBL resist and the poor etch selectivity. One method to improve this is to use a hard etch mask such as chrome (Cr) or nickel (Ni) that does not degrade during the nitride dry etching because of much higher etch selectivity. Such metals can be patterned by a lift-off technique where the metal is deposited on a EBL patterned resist mask that is subsequently removed [132].

### **3.4.1 Cr on top acting as both the charge dissipating layer during EBL and hard mask for successive etching**

As mentioned earlier that during the EBL pattern writing process on insulating glass the wafer surface gets charged and repels the incoming electrons. This charging effect distorts the pattern which limits patterning of nanostructures on insulating substrates [133]. Here, the charging effects were suppressed by using a 30 nm conductive Cr metal layer on top of the  $\text{Si}_x\text{N}_y$ . Instead of using a lift off technique, a thin layer of Cr is deposited directly on the  $\text{Si}_x\text{N}_y$  before the EBL. The conductive Cr layer not only resolves the electron discharging issue but also act as a hard mask for deep etching of  $\text{Si}_x\text{N}_y$ . Using this method, we also achieved very high aspect ratio (10:1) nanostructures with a minimum dimension of 60 nm (please see Section 3.9) without sacrificing the quality of the flat top of the narrow lines.

### **3.4.2 Sample preparation and EBL Process steps**

A 400 nm thick  $\text{Si}_x\text{N}_y$  layer was deposited on a quartz wafer by using plasma enhanced chemical vapour deposition (PECVD). Then a 30 nm thin Cr layer was deposited on the  $\text{Si}_x\text{N}_y$  by using electron beam evaporation. The Cr deposited wafer is cleaned by DI water and soft baked. Then, a resist adhesion enhancer, HMDS and the diluted positive tone ebeam resist (1:1 ZEP520 : ZEPA) were spun successively on the wafer at a speed of 3000 rpm. The spinning gives about 190 nm thin ZEP resist on the Cr covered Quartz wafer. The wafer is then soft baked at 120°C for 3 minutes. The wafer is then loaded in the E-Beam (JEOL JBX6000FS/E) system (please see appendix B for detail of the specifications of the JEOL JBX6000FS/E EBL system). The RWG pattern was written in the resist using electron beam with acceleration voltage of 50KV and writing field of  $80\ \mu\text{m} \times 80\ \mu\text{m}$ . The full wafer ebeam pattern had been generated separately in a database file format (.gds) using the CleWin layout editor. Each  $1.5\ \text{cm} \times 1\ \text{cm}$  sized chip is designed to have four RWG sensors ( $500\ \mu\text{m} \times 500\ \mu\text{m}$  each) separated by such a distance which matches perfectly with the micro-fluidic channels. Altogether 33x  $1.5\ \text{cm}$  by  $1\ \text{cm}$  chips were designed on each four inch wafer.



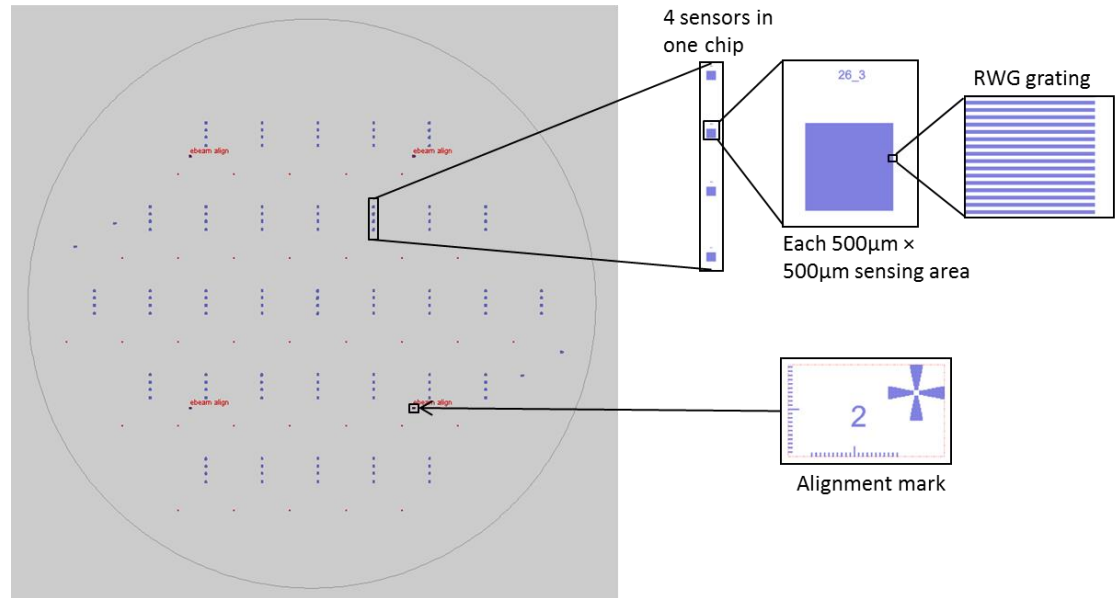


**Figure 3.4-1 Full wafer ebeam pattern consisting of 33 sensor chips of 1.5cm by 1cm size on a 100mm diameter wafer. Each chip has four RWG sensor of size 500µm × 500µm.**

However, the EBL procedure behaves differently for different nano-patterns, different substrates and even for different layers on the same substrate. When an electron from the writing beam strikes the surface of a substrate it undergoes various scattering events losing energy and causing the generation of secondary electrons. Two adjacent features will contribute a background dose of secondary electrons to each other resulting in a higher effective dose known as proximity effect. This causes a broadening of the exposed features [134]. This is particularly apparent with dense features like gratings (1D RWG) or 2D RWGs. Thus a proximity correction has been imposed to the designed ebeam pattern (credit goes to Brendan MacCarthy, engineer at EBL facility at Tyndall National Institute) by the ‘Layout beamer’ software purchased from a German company named Genisys.

Test exposures were performed to find the optimum electron beam energy dose for the pattern concerned. A dose of 120 µC/cm<sup>2</sup> was found to be optimum for RWG pattern on a Cr covered Quartz wafer. At the start of the pattern writing the electron-beam is focused on the resist surface and the writing was started.

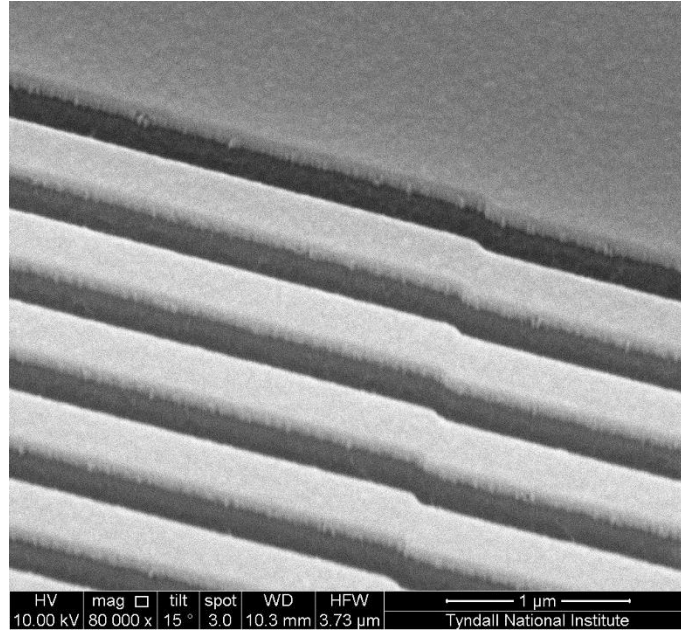


**Figure 3.4-2 SEM image of stitching error during EBL writing.**

As mentioned in 3.1.3, in EBL, a large area pattern is divided into smaller writing fields. In our case the writing field was  $80\ \mu\text{m} \times 80\ \mu\text{m}$ . Each of this  $80\ \mu\text{m} \times 80\ \mu\text{m}$  field was then stitched together by stage movement to generate the large area pattern. Precise stage movement was essential otherwise stitching error occurs occasionally as shown in Figure 3.4-2.

When the pattern was written, the wafer was developed by ZEDN50 developer for 30 seconds followed by an Isopropanol (IPA) rinse. The wafer was then baked again at  $120^\circ\text{C}$  for 3 minute. Then the pattern transfer was done by successive ICP Cr and  $\text{Si}_x\text{N}_y$  dry etching (please see Section 3.6 for detail).

### 3.5 Nano-imprint patterning process steps

The RWG sensors were also manufactured by UV nano-imprint lithography (NIL) on a wafer-scale level with the help of VTT, Finland, one of the EU partners of my PhD project. The basic process of UV-NIL is depicted in Figure 3.5-1. All nano-imprints were made with VTT's Obducat Eitre 6 nano-imprinter tool, which is based on the air pressure

imprinting technique. After the process optimisation for the specific geometry of the sensor, this method enabled good yield and uniformity across the almost full wafer area as well as ultra-thin (<20nm) residual layer, which is preferred for successful pattern transfer by ICP.

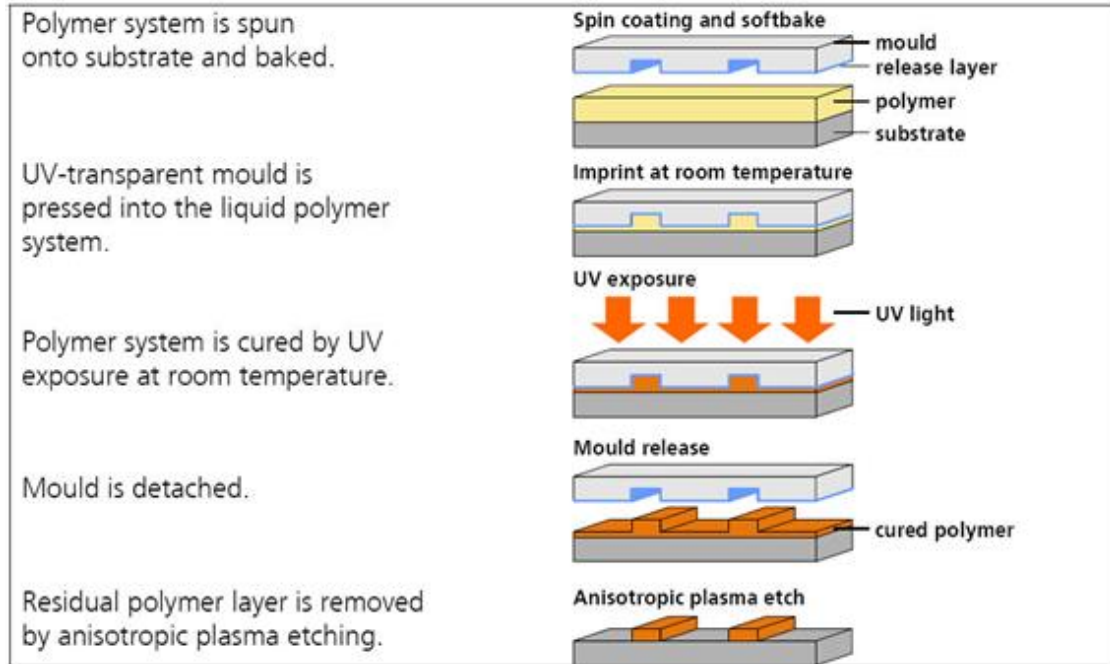


**Figure 3.5-1 Basic process scheme of the used UV-based nanoimprint lithography (drawing by Micro Resist Technology GmbH). Note: Mould means the same as stamp, which is the word used in this report (elsewhere also ‘template’ used sometimes), and polymer means the nano-imprint resist here.**

The master stamp was made by EBL method on the 4” Si wafer. Before any copies can be taken from the master stamp it have to be anti-adhesion treated to enhance the releasing properties of the UV materials that are used to make the intermediate stamps (actual working stamps). The UV material was OrmoStamp (by Micro Resist Technology). The nano-imprint step for making intermediate stamps is depicted in the Figure 3.5-2.

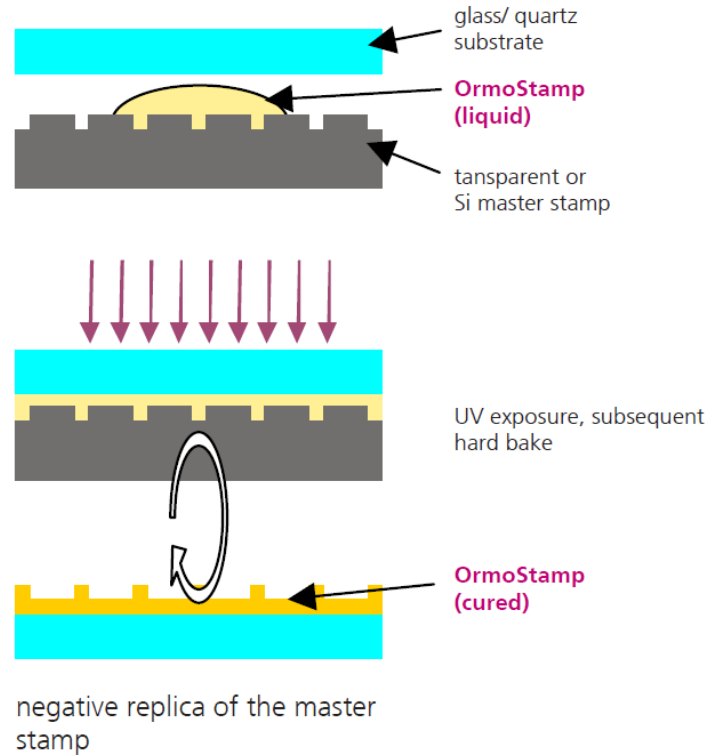


**Figure 3.5-2 Procedure to make intermediate stamps from the master stamp (drawing by Micro Resist Technology).**

Also the intermediate masters were anti-adhesion treated with the trichlorosilane. Intermediate masters were used to pattern the UV-resist layer on the glass wafers. These wafers have  $\text{Si}_x\text{N}_y$  and Cr deposition. The nano-imprint resist used was mr-UVCur21-200nm supplied by Micro Resist Technology. 200nm-thick layer of resist was spun on the glass wafer and pre-baked. After that the resist layers on the wafers were patterned by imprinting with the intermediate stamps. An example photograph of an imprint patterned resist layer on a glass wafer (including  $\text{Si}_x\text{N}_y$  and Cr layers on top) is shown in Figure 3.5-3 left. Some interference pattern (colour variation) is seen, especially near the edges of the resist area, due to the minor thickness variation in the layer. For comparison, similarly patterned resist layer but on a bare Si wafer is shown on the right. It does not include the parallel lines of the interference pattern seen on the left image, which indicates the lines are related to the glass wafer or  $\text{Si}_x\text{N}_y$  and Cr layers on it. However, we were transferring the pattern from nano-imprint resist to Cr which was acting as hard mask. As over-etching was done to have clean and quality hard mask (please see Section 3.6.1), a little thickness variation in the resist layer was not an issue for post-processing.

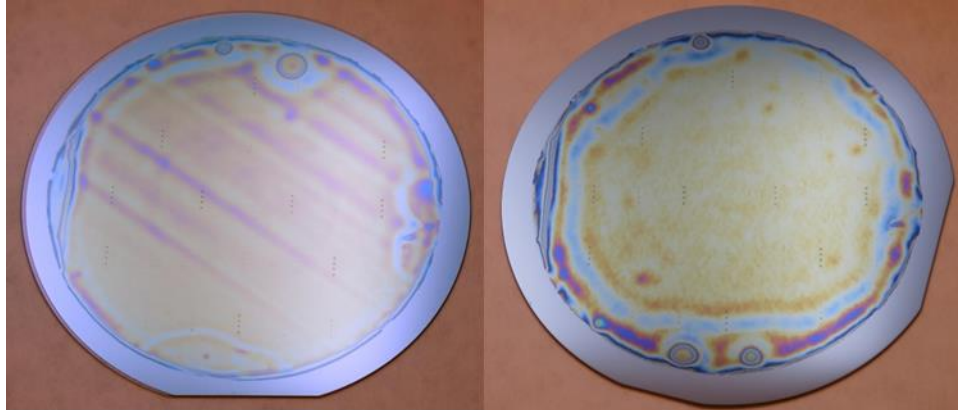


**Figure 3.5-3 Photographs of nano-imprinted resist layers patterned with the RWG on 4” wafers: left) Resist patterned on glass wafer that have  $\text{Si}_x\text{N}_y$  and Cr layers; right) Resist patterned on bare Si wafer.**

Besides, there was variation in between the designed (EBL layout generated for master stamp) and the patterned feature dimensions. As mentioned earlier that at the beginning of the NIL process, normally a Si master stamp is produced by EBL which is used for making OrmoStamp (intermediate stamp). OrmoStamp is used later for nano-patterning on sample substrate. So, if the deviation from the designed dimension occurs at master stamp during EBL, it will be carried out to all the OrmoStamps and successive patterning procedure. So, optimization of the EBL procedure was needed.

## **3.6 Chrome etching process development by Inductively Coupled Plasma (ICP)**

The Cr etching recipe was developed to get high selectivity with nano-patterned resist mask so that the pattern can be transferred from resist layer (limited thickness) to Cr layer easily. As shown later in this chapter that the etch rate of Cr is dependent on the size of the opening of the nanostructure (wider openings etch faster than narrower ones) and the size of the sample to be etched. As we are dealing with nano-structure of size about 100-200nm, it would take quite a long time to get the Cr fully etched into that groove of the

grating and cleaned properly. Having a thin layer of resist (~200 nm), the selection of the thickness of Cr was crucial. The Cr should be thin enough that the Cr layer got fully etched by the time the ebeam/nano-imprint resist (acting as a mask now) was not fully etched away. At the same time, the Cr should be thick enough that it could survive as hard mask while deep etching of  $\text{Si}_x\text{N}_y$  in the next step. So, a highly selective Cr dry etching recipe should be developed.

Cr is the common metal used in photo-mask production and  $\text{Cl}_2 - \text{O}_2$  based dry etching has been used for its patterning. Nakata, et al. [135] have shown that oxygen and chlorine radicals are responsible for etching the chrome. As oxygen will also etch the resist and thus affect the selectivity it is necessary to have a good understanding of the etching chemistry and surface reactions. Kwon, et al. [136] used x-ray photoelectron spectroscopy to study the surface reactions during chrome etching. They found that chrome binds with oxygen and chlorine atoms at the surface. When Cr is etched using a pure  $\text{Cl}_2$  plasma,  $\text{CrCl}_n$  ( $n=1-3$ ) is formed on the surface and is not easily removed because of its low vapour pressure. When  $\text{O}_2$  is included in the plasma  $\text{CrCl}_2\text{O}_2$  is formed ( $\text{Cr} + 2\text{O} + 2\text{Cl} \rightarrow \text{CrO}_x\text{Cl}_y$ ) which is volatile at room temperature.

From the above expression, it is clear that the concentration of oxygen and chlorine radicals are important factors that determine the Cr etch rate. In the ICP etching process the coil and platen power, the gaseous chemical composition, chamber pressure, substrate and chamber surface temperatures, and gas flow rate all play a role. It was also found that the etch rate usually had a radial distribution across a 4-inch wafer with the etch rate being lower towards the periphery of the wafer. The etch rate was also reduced by loading effects caused by the density of the pattern along with the size and shape of the nanostructure to be etched. To overcome the loading effect and feature size dependency, the Cr should be etched for longer as compared with an un-patterned layer. Thus it was necessary to optimise the etch selectivity between the Cr and resist to allow the required patterning.

Different ICP parameters such as the chamber pressure, coil and platen power, and Oxygen : Chlorine ratio had been varied to obtain the selectivity trends. The selectivity

increased with the chamber pressure and gave the highest value for a pressure of 80 mT (Figure 3.6-1a). The increase of the ICP platen power reduced the selectivity before saturating (Figure 3.6-1b). We also found that the selectivity increased initially with the oxygen concentration and then saturated when the oxygen concentration was  $> 20\%$  as shown in Figure 3.6-1c. In contrast, the coil power did not affect the selectivity significantly. Using the selectivity and Cr etch rate trends for different plasma parameters the best selectivity had been found as 1.41. The optimum parameters for the Cr etching recipe were shown in Table 3.6-1. This recipe gave a Cr etch rate of 58 nm/min in un-patterned areas.

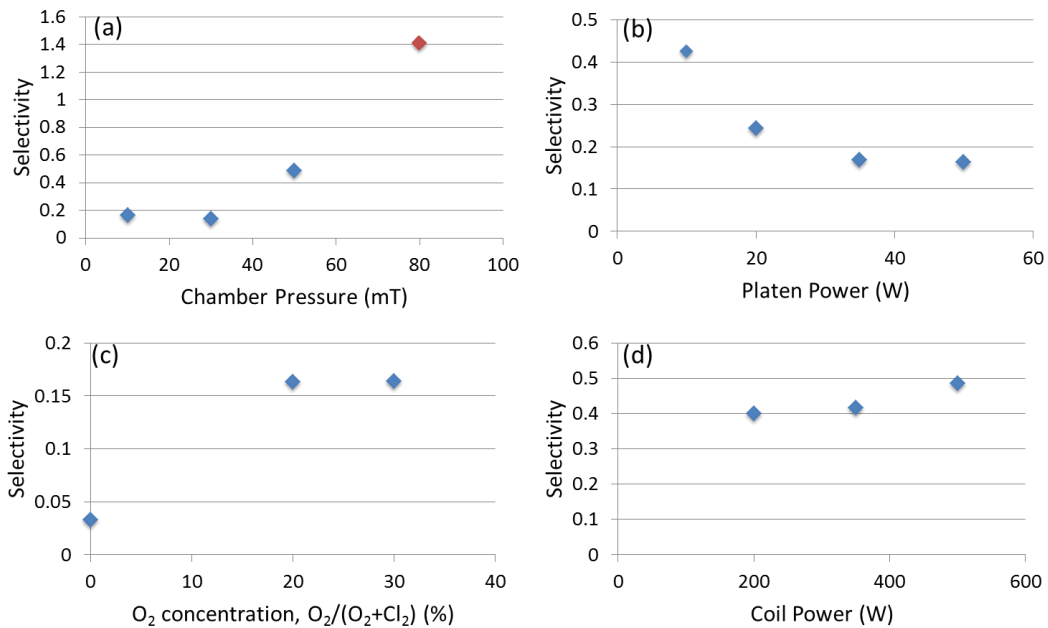


**Figure 3.6-1 Cr/ZEP resist etch selectivity due to variation in (a) chamber pressure, (b) platen power, (c) oxygen concentration ratio ( $O_2/(O_2+Cl_2)$ ) and (d) coil power.**

**Table 3.6-1 Parameters of the optimized Cr etch recipe which gives a selectivity of 1.41:1 and a Cr etch rate of about 58 nm/min in un-patterned areas.**

Parameter	Values
Cl <sub>2</sub> gas flow	70 sccm
O <sub>2</sub> gas flow	30 sccm
Coil power	500 W
Platen power	50 W
Chamber pressure	80 mT
Temperature of platen	10 °C

### 3.6.1 Loading effect

It was found that the etch rate of Cr was dependent on the size of the opening of the nanostructure (wider openings etch faster than narrower ones) and the size of the sample to be etched. As an example, a 30 nm of Cr in an open area took 31 s to be fully etched. But, the SEM image in Figure 3.6-2a showed that a 30 nm-thick Cr nano-grating with groove openings of 240 nm on a 4 inch glass wafer when etched even for 1 minute did not fully remove the Cr and subsequently the Si<sub>x</sub>N<sub>y</sub> etching did not proceed properly. Though etching for 2 min showed improvement, small residues remained at the edge of the grating after the Cr etching and subsequent Si<sub>x</sub>N<sub>y</sub> etching as shown in Figure 3.6-2b and Figure 3.6-2c. Finally, when the Cr nano-grating was etched for 3 min, a fine grating structure was obtained as shown in Figure 3.6-2d. All the images of Figure 3.6-2 were taken before stripping off the Cr (process step in Figure 3.2-2) with a very thin layer of Au deposited on the sample to avoid the charging during SEM imaging.



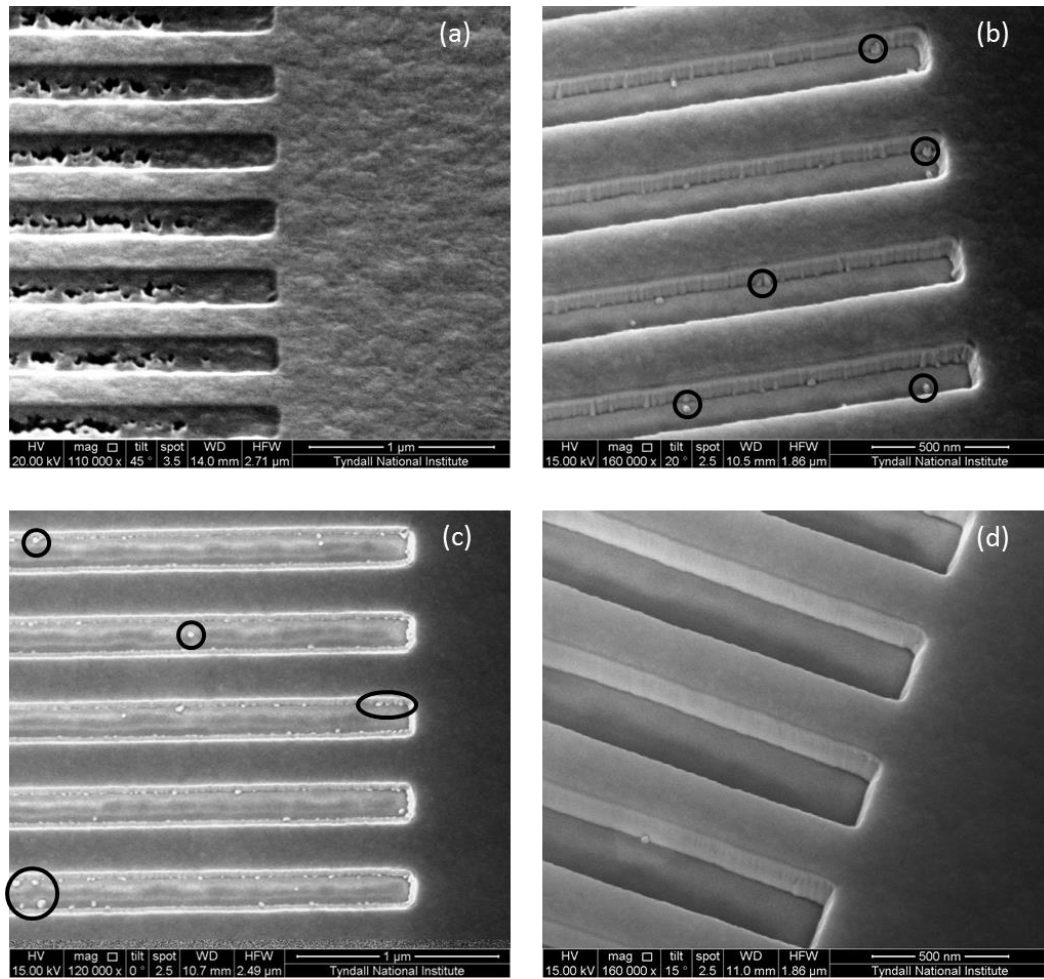


**Figure 3.6-2 SEM images of the  $\text{Si}_x\text{N}_y$  nano-grating after Cr and  $\text{Si}_x\text{N}_y$  etching: (a) Cr etched for 1 min, (b) & (c) Cr etched for 2 min but dot-shaped residues remain at the edge of the nano-grating and (d) cleaner edge of the nano-grating when Cr is etched for 3 min.**

### 3.7 Pattern transfer

The pattern transfer procedure for both ebeam patterned wafer and nano-imprinted wafer were same. The patterned wafer was loaded in the ICP chamber for etching the exposed Cr layer for 3 minutes using the developed optimal Cr etching recipe (Section 3.6). Then the resist layer on top of the Cr layer, was removed by the standard ‘MICROPOSIT resist remover 1165’, a pure organic solvent. Normally, the resist becomes very sticky when exposed to the Chlorine gas inside the ICP chamber during Cr etching and hence require

an additional 3 minutes of O<sub>2</sub> plasma ashing before and after using the 1165 resist remover. At this stage, the wafer had the nano-pattern transferred into the Cr layer.

**Table 3.7-1 Parameters of the SixNy ICP etching recipe.**

Parameter	Values
Gas mixture	CF <sub>4</sub> /CHF <sub>3</sub>
Coil power	800W
Platen power	75W
Chamber pressure	50mT
Chuck Temperature	10°C

The pattern was subsequently transferred into the Si<sub>x</sub>N<sub>y</sub> using another ICP etching recipe as shown in Table 3.7-1. The Cr layer acted as a hard mask for this etching. The etch rate of Si<sub>x</sub>N<sub>y</sub> was measured as 6 nm per second. There was also an initial plasma settling time of about 9 seconds which causes an additional etching depth of 54 nm. So, for etching a depth of 400nm, the etch time was  $(400-54)/6 = 58$  sec. As the etch rate was 6 nm/sec, 58 seconds of etching time gave the etching depth of 348 nm and the initial 9 seconds of plasma settling time gave an additional 54 nm of etching depth which yielded a grating of almost 400nm depth. However, the image in Figure 3.7-1 captures the front face of the full wafer after Si<sub>x</sub>N<sub>y</sub> etching. The RWG sensors lit up at certain diffraction angle as shown in the Figure 3.7-1.

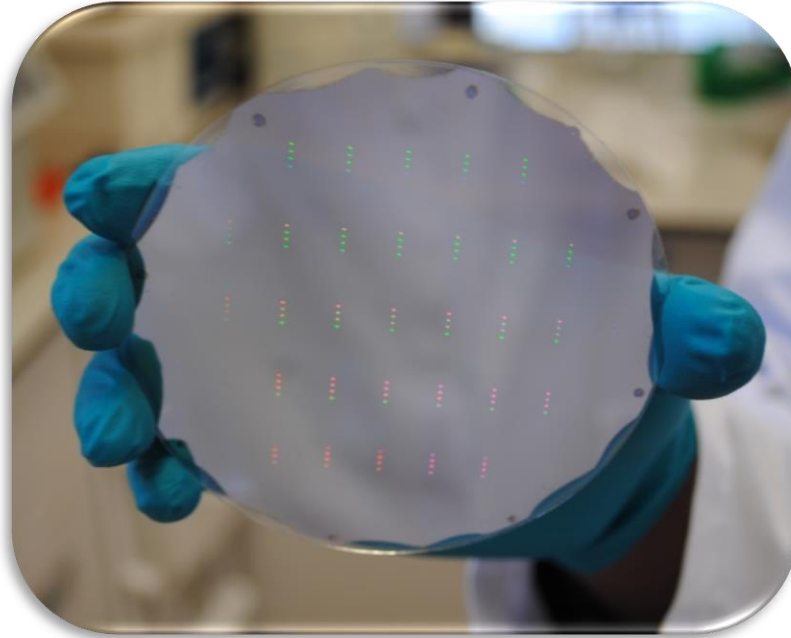


**Figure 3.7-1** Snapshot of the processed full wafer after SixNy etching.

### 3.7.1 Sidewall quality

The influence of etching slope on cavity Q-factors in two-dimensional (2D) photonic crystal (PhC) slab is studied in [131]. RWG sensor is also prone to the reduction of Q factor for increasing grating sidewall slope. The Q-factor decreases with grating's sidewall slope. So, the slope of the fabricated grating was measured by cross-sectioning of the grating using FIB milling and then imaging by SEM.

#### **Tilt angle measurement**

1. RWG sensor with different filling fraction (for making the measurement easy) was fabricated by using the presented EBL nano-fabrication technique.
2. A portion of the grating ( $10\ \mu\text{m} \times 2\ \mu\text{m}$ ) was covered with  $5\ \mu\text{m}$  thick **protective layer** of Tungsten+Platinum deposited by the FIB tool.
3. A  **$5\ \mu\text{m}$  deep** trench of  $10\ \mu\text{m} \times 6\ \mu\text{m}$  size was made perpendicular to the grating lines by ion bombardment.

4. SEM pictures were then taken in the SEM tool by tilting the grating chip at  $52^\circ$  angle.

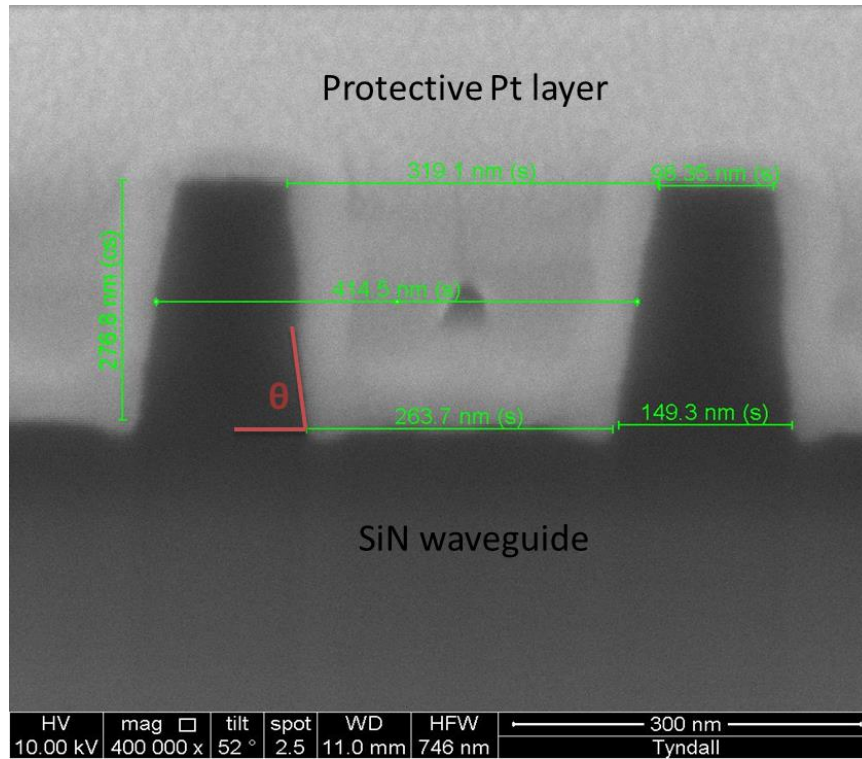


**Figure 3.7-2 Cross-sectional image of the RWG sensor for sloped sidewall angle measurement.**

The groove width and height measurements shown in the above picture reveals that the  $\text{Si}_x\text{N}_y$  etching recipe gives a sidewall angle ( $\theta$ ) of  $84.7^\circ$  which is very good in quality.

### 3.8 Alignment mark and dicing

To make it easy to find the sensor positions in a 1.5 cm by 1cm sensor chip and also for aligning with other bio-steps, an additional photolithography step was introduced to put dedicated alignment marks along with horizontal and vertical lines of Cr pointing towards the sensors. Two alignment marks were introduced in each sensor chip and those alignment marks were required for photo de-protection by Manchester Chemistry group, another EU project partner of my PhD project. Dicing marks were also printed from the

same photolithography procedure. The Cr was then wet etched and the wafer was ready for dicing along the dicing lines created from this photolithography step.

A protective layer of thick resist (S1828 resist of thickness of  $4\mu\text{m}$ ) was coated on top of the full wafer to avoid any damage of the nano-sensors that might be caused by the debris during dicing of the wafer. A mechanical dicer was used to cut the quartz wafer at a slow speed to ensure a smooth edge and also avoid cracking. The 33 chips were diced from a single wafer.

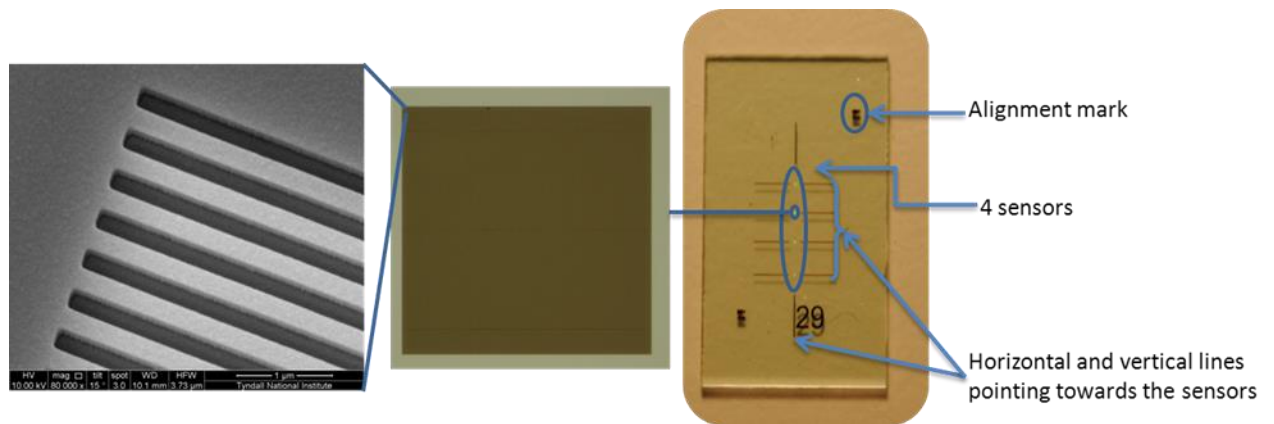


**Figure 3.8-1 Detail of the final sensor chip ( $1.5\text{cm} \times 1\text{cm}$ ) with alignment marks.**

The protective resist layer is removed from each chip and then the chips were ready for inspection. Figure 3.8-1 shows the diced sensor chip ( $1.5\text{ cm}$  by  $1\text{ cm}$ ) with four sensors in the center. Four horizontal lines and two vertical Cr lines are heading towards the sensor so that the sensor can be easily located. Figure 3.8-2 shows the detailed SEM image of the fabricated sensor with period  $430\text{ nm}$ , trench width  $180\text{ nm}$  and grating teeth width  $250\text{ nm}$ . So the filling fraction is  $58.1\%$ . However, two or three chips from the different parts of the full wafer were randomly selected for optical characterization. The measured resonance spectrum at the desired wavelength verified that the fabrication procedure went well (please see chapter 4) and the thirty three sensor chips were ready for bio-functionalisation.

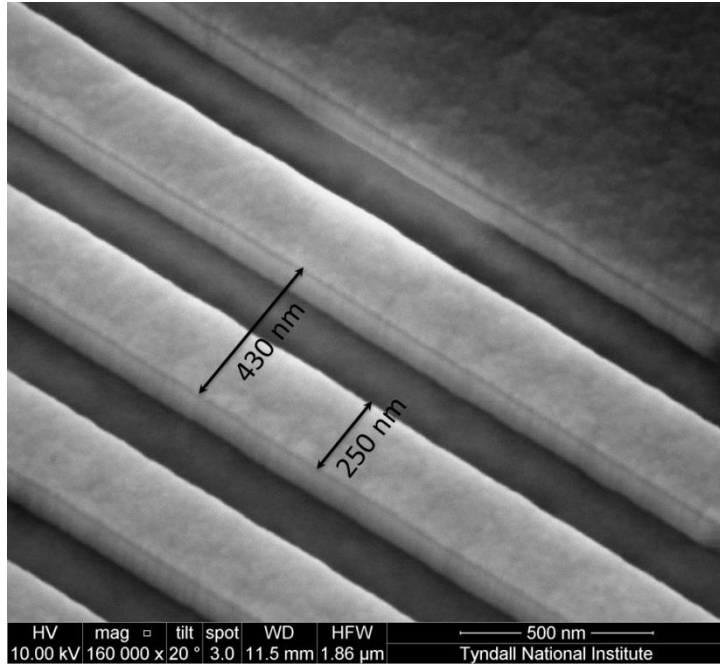


**Figure 3.8-2 SEM image of the fabricated RWG sensor shows period of 430 nm and filling fraction of  $(250/430) = 58.1\%$ .**

### 3.9 High aspect ratio nanostructure

There is interest in the fabrication of high aspect ratio nanostructures on transparent and insulating substrates such as quartz, pyrex or borosilicate glass. High aspect ratio nanostructures can potentially be used for light trapping device for LEDs, solar cells with higher absorption coefficient, for batteries with greater energy densities and also in making nano-imprint moulds.

As mentioned earlier that in the proposed nano-fabrication scheme, the Cr layer acts as a hard mask which facilitates deep etching of nitride layer as the etch selectivity of Cr to  $\text{Si}_x\text{N}_y$  is around 25:1. So, it was challenged to achieve the highest aspect ratio nanostructure in glass using the developed fabrication technique.

A 2  $\mu\text{m}$  thick layer of  $\text{SiO}_2$  is first deposited on the borosilicate glass wafer (100 mm in diameter) followed by 400 nm of  $\text{Si}_x\text{N}_y$  and finally a 30 nm thick Cr layer. A 30 nm thick layer of Cr could survive for etching  $\text{Si}_x\text{N}_y$  up to 750 nm with the selectivity of 25:1. 60 nm wide periodic ridges in a grating structure were patterned by EBL on the wafer.

The pattern was then transferred to the Cr layer using ICP Cr etching mentioned in Section 3.6. After etching the patterned Cr layer, the pattern was then transferred into the  $\text{Si}_x\text{N}_y$  and  $\text{SiO}_2$  layers by ICP dry etching to a total depth of 675 nm. Figure 3.9-1a and Figure 3.9-1b show the SEM images of the high aspect ratio nano-grating with periods of 1.1  $\mu\text{m}$  and 490 nm respectively. A very thin layer of Au was deposited on the sample to avoid the charging during SEM imaging. The Cr layer was not removed and the flat tops of gratings are preserved (Figure 3.9-1). A very high aspect ratio of 10:1 is achieved for ~60 nm narrow lines of grating while preserving the quality of the flat top of these narrow lines. This is the highest achieved aspect ratio to date in glass substrate [137].

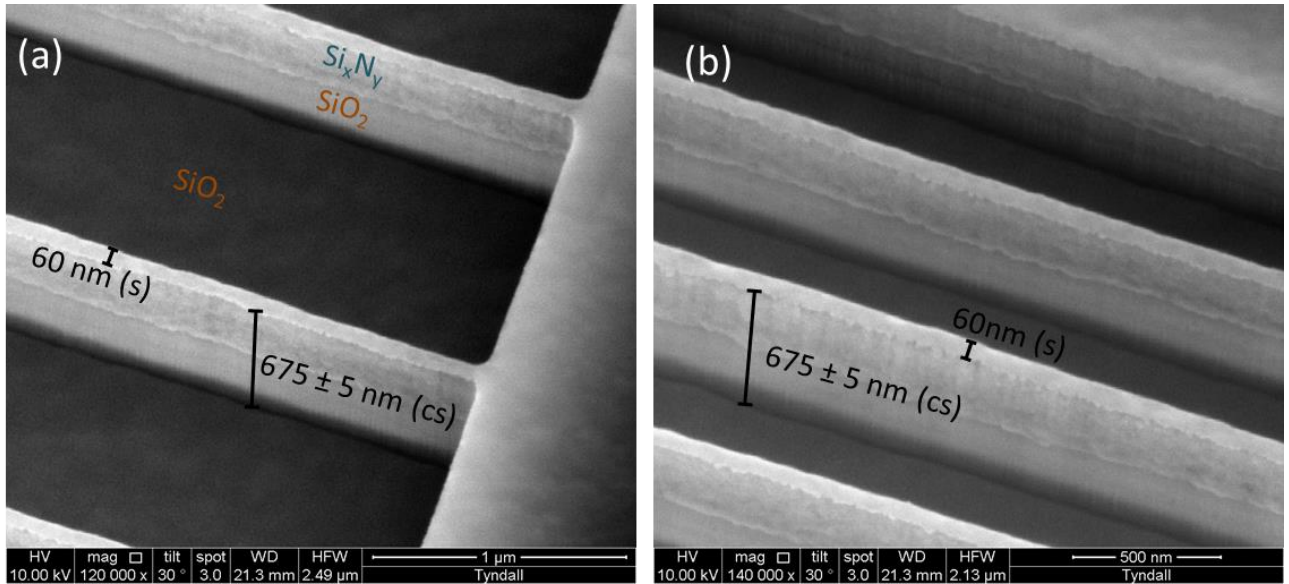


**Figure 3.9-1 SEM images of the fabricated high aspect ratio nanostructures in  $\text{Si}_x\text{N}_y$  on glass substrates:  $\sim 60$  nm wide (surface measurement - s) and  $675 \pm 5$  nm deep (cross-sectional measurement - cs) grating line with (a)  $1.1 \mu\text{m}$  spacing and (b)  $490$  nm spacing.**

### 3.10 Summary

Different potential fabrication techniques are discussed and contrasted to find out viable routes for fabricating the RWG sensor. A fabrication method for RWG nanostructures on insulating (quartz or glass) substrates has been presented using either EBL or NIL as patterning procedure. PECVD process was developed as a low temperature alternative for the development of low optical loss  $\text{Si}_x\text{N}_y$  waveguide material. The study of the impact of different plasma parameters (e.g., precursor gas composition, plasma frequency, pressure etc.) in PECVD  $\text{Si}_x\text{N}_y$  deposition reveals that the increase in  $\text{NH}_3$  concentration and switching the plasma mode from mixed frequency (low + high) to the single (low) frequency improves the surface roughness of  $\text{Si}_x\text{N}_y$  and hence, reduces the optical loss of the material. Deposition of hundreds of nm of  $\text{SiO}_2$  on top of the  $\text{Si}_x\text{N}_y$  layer and thermal annealing can also be considered for further improvement of the optical loss



of the material. However, in the fabrication process, a thin Cr layer is used to act as a hard mask to permit deep  $\text{Si}_x\text{N}_y$  etching and also to serve as a conductive layer which helps reducing the charging effect specifically during EBL. In order to transfer the pattern onto the Cr layer, an optimum Cr etching recipe was developed specially for etching nanostructures. It was found that the Cr etch rate was highly dependent on the size of the opening of the nanostructure with wider openings etching faster than narrower ones. For getting quality Cr etch mask a selective Cr etching recipe was required to allow longer Cr etching with a limited thickness of the resist layer. The developed Cr etching recipe showed selectivity of 1.41 which facilitates 6 times longer Cr etching to get a clean Cr etch mask. Having a clean nano-patterned Cr hard mask, the layout was transferred into  $\text{Si}_x\text{N}_y$  using ICP nitride etching. Higher  $\text{Si}_x\text{N}_y$  etching selectivity of the Cr mask (25:1) than that of ebeam resist mask (1:1) allows deep etching of  $\text{Si}_x\text{N}_y$ . So, an etching depth of 400 nm in  $\text{Si}_x\text{N}_y$  was easily achieved with initial resist thickness of only 200 nm. Using the developed nano-fabrication technique very high aspect ratio (highest to date in literature [137]) nanostructures of 10:1 is achieved for a very narrow 60 nm wide grating lines.

Instead of bogged into single sensor chip production, wafer scale batch production of the RWG sensor was carried out at first using EBL for proof of concept and then NIL to reduce the cost of production further. The gathered knowledge for example, reducing charging effect during EBL, using Cr hard mask for nano-structure, Cr etch rate dependency on nano-structure openings, challenge of making high aspect ratio nano-structure, residual layer thickness variation in NIL across the 4" wafer, optimization of NIL process steps to get the desired dimensions etc. would surely help others heading towards batch nano-structure production on glass. Further, study can be carried out on optimizing NIL processes to achieve micron and nano sized features printed at the same time in the same wafer for full layout solution in a single step.

## References

- [1] Jukka Viheriälä, Tapio Niemi, J. Kontio, and M. Pess, "Nanoimprint Lithography - Next Generation Nanopatterning Methods for Nanophotonics Fabrication, Recent Optical and Photonic Technologies, InTech," 2010.
- [2] "Suss Report: the Customer magazine of SUSS Microtec," 2013.
- [3] "ASML, TWINSCAN™ NXT:1950i specifications," 2009.
- [4] B. L. Kelion, "Intel's Ivy Bridge chips launch using '3D transistors'," in *BBC Technology News*, ed, 22 April 2012.
- [5] S. Reyntjens and R. Puers, "A review of focused ion beam applications in microsystem technology," *Journal of Micromechanics and Microengineering*, vol. 11, pp. 287-300, Jul 2001.
- [6] D. J. Stokes, T. Vystavel, and F. Morrissey, "Focused ion beam (FIB) milling of electrically insulating specimens using simultaneous primary electron and ion beam irradiation," *Journal of Physics D-Applied Physics*, vol. 40, pp. 874-877, Feb 7 2007.
- [7] A. Pimpin and W. Srituravanich, "Review on Micro- and Nanolithography Techniques and Their Applications," *Engineering Journal*, vol. 16, 2011.
- [8] M. J. Madou, *Fundamentals of Microfabrication: The Science of Miniaturization*: New Yourk: CRC, 2002.
- [9] C. Vieu, F. Carcenac, A. Pepin, Y. Chen, M. Mejias, A. Lebib, *et al.*, "Electron beam lithography: resolution limits and applications," *Applied Surface Science*, vol. 164, pp. 111-117, Sep 1 2000.
- [10] A. E. Grigorescu and C. W. Hagen, "Resists for sub-20-nm electron beam lithography with a focus on HSQ: state of the art," *Nanotechnology*, vol. 20, Jul 22 2009.
- [11] M. Altissimo, "E-beam lithography for micro-/nanofabrication," *Biomicrofluidics*, vol. 4, Jun 2010.
- [12] B. D. Gates, Q. B. Xu, M. Stewart, D. Ryan, C. G. Willson, and G. M. Whitesides, "New approaches to nanofabrication: Molding, printing, and other techniques," *Chemical Reviews*, vol. 105, pp. 1171-1196, Apr 2005.
- [13] R. F. Pease and S. Y. Chou, "Lithography and other patterning techniques for future electronics," *Proceedings of the Ieee*, vol. 96, pp. 248-270, Feb 2008.
- [14] R. Menon, A. Patel, D. Gil, and H. I. Smith, "Maskless lithography," *Materials Today*, vol. 8, pp. 26-33, Feb 2005.
- [15] H. Raether, "Surface-Plasmons on Smooth and Rough Surfaces and on Gratings," *Springer Tracts in Modern Physics*, vol. 111, pp. 1-133, 1988.

- [16] W. Srituravanich, N. Fang, C. Sun, Q. Luo, and X. Zhang, "Plasmonic nanolithography," *Nano Letters*, vol. 4, pp. 1085-1088, Jun 2004.
- [17] C. Genet and T. W. Ebbesen, "Light in tiny holes," *Nature*, vol. 445, pp. 39-46, Jan 4 2007.
- [18] W. Srituravanich, L. Pan, Y. Wang, C. Sun, D. B. Bogy, and X. Zhang, "Flying plasmonic lens in the near field for high-speed nanolithography," *Nat Nanotechnol*, vol. 3, pp. 733-7, Dec 2008.
- [19] A. Cattoni, E. Cambril, D. Decanini, G. Faini, and A. M. Haghiri-Gosnet, "Soft UV-NIL at 20 nm scale using flexible bi-layer stamp casted on HSQ master mold," *Microelectronic Engineering*, vol. 87, pp. 1015-1018, May-Aug 2010.
- [20] S. Y. Chou, P. R. Krauss, and P. J. Renstrom, "Imprint lithography with 25-nanometer resolution," *Science*, vol. 272, pp. 85-87, Apr 5 1996.
- [21] J. Chen, J. Shi, D. Decanini, E. Cambril, Y. Chen, and A. M. Haghiri-Gosnet, "Gold nanohole arrays for biochemical sensing fabricated by soft UV nanoimprint lithography," *Microelectronic Engineering*, vol. 86, pp. 632-635, Apr-Jun 2009.
- [22] K. Balasubramanian, "Challenges in the use of 1D nanostructures for on-chip biosensing and diagnostics: A review," *Biosensors & Bioelectronics*, vol. 26, pp. 1195-1204, Dec 15 2010.
- [23] C. Wang, J. Ouyang, H. L. Gao, H. W. Chen, J. J. Xu, X. H. Xia, *et al.*, "UV-ablation nanochannels in micro/nanofluidics devices for biochemical analysis," *Talanta*, vol. 85, pp. 298-303, Jul 15 2011.
- [24] N. Daldosso, M. Melchiorri, F. Riboli, M. Girardini, G. Pucker, M. Crivellari, *et al.*, "Comparison among various Si<sub>3</sub>N<sub>4</sub> waveguide geometries grown within a CMOS fabrication pilot line," *Journal of Lightwave Technology*, vol. 22, pp. 1734-1740, Jul 2004.
- [25] A. Z. Subramanian, P. Neutens, A. Dhakal, R. Jansen, T. Claes, X. Rottenberg, *et al.*, "Low-Loss Singlemode PECVD Silicon Nitride Photonic Wire Waveguides for 532-900 nm Wavelength Window Fabricated Within a CMOS Pilot Line," *IEEE Photonics Journal*, vol. 5, pp. 2202809-2202809, 2013.
- [26] K. N. Andersen, W. E. Svendsen, T. Stimpel-Lindner, T. Sulima, and H. Baumgartner, "Annealing and deposition effects of the chemical composition of silicon-rich nitride," *Applied Surface Science*, vol. 243, pp. 401-408, Apr 30 2005.
- [27] X. J. Liu, J. J. Zhang, X. W. Sun, Y. B. Pan, L. P. Huang, and C. Y. Jin, "Growth and properties of silicon nitride films prepared by low pressure chemical vapor deposition using trichlorosilane and ammonia," *Thin Solid Films*, vol. 460, pp. 72-77, Jul 22 2004.
- [28] S. C. Mao, S. H. Tao, Y. L. Xu, X. W. Sun, M. B. Yu, G. Q. Lo, *et al.*, "Low propagation loss SiN optical waveguide prepared by optimal low-hydrogen module," *Optics Express*, vol. 16, pp. 20809-20816, Dec 8 2008.

- [29] J. Yota, J. Hander, and A. A. Saleh, "A comparative study on inductively-coupled plasma high-density plasma, plasma-enhanced, and low pressure chemical vapor deposition silicon nitride films," *Journal of Vacuum Science & Technology a-Vacuum Surfaces and Films*, vol. 18, pp. 372-376, Mar-Apr 2000.
- [30] F. Ay and A. Aydinli, "Comparative investigation of hydrogen bonding in silicon based PECVD grown dielectrics for optical waveguides," *Optical Materials*, vol. 26, pp. 33-46, Jun 2004.
- [31] W. A. Lanford and M. J. Rand, "The hydrogen content of plasma-deposited silicon nitride," *Journal of Applied Physics*, vol. 49, pp. 2473-2477, 1978.
- [32] B. F. Hanyaloglu and E. S. Aydil, "Low temperature plasma deposition of silicon nitride from silane and nitrogen plasmas," *Journal of Vacuum Science & Technology A*, vol. 16, pp. 2794-2803, Sep-Oct 1998.
- [33] I. JonakAuer, R. Meisels, and F. Kuchar, "Determination of the hydrogen concentration of silicon nitride layers by Fourier transform infrared spectroscopy," *Infrared Physics & Technology*, vol. 38, pp. 223-226, Jun 1997.
- [34] A. Gorin, A. Jaouad, E. Grondin, V. Aimez, and P. Charette, "Fabrication of silicon nitride waveguides for visible-light using PECVD: a study of the effect of plasma frequency on optical properties," *Optics Express*, vol. 16, pp. 13509-13516, Sep 1 2008.
- [35] F. Karouta, K. Vora, J. Tian, and C. Jagadish, "Structural, compositional and optical properties of PECVD silicon nitride layers," *Journal of Physics D-Applied Physics*, vol. 45, Nov 7 2012.
- [36] *Robust, affordable photonic crystal sensors for point-of-care disease diagnostics*. Available: <http://www.phastid.eu/>
- [37] K. Mohamed and M. M. Alkaisi, "Investigation of a nanofabrication process to achieve high aspect-ratio nanostructures on a quartz substrate," *Nanotechnology*, vol. 24, p. 015302, 2013.
- [38] M.-K. Kim, I.-K. Hwang, J.-K. Yang, and Y.-H. Lee, "Influence of etching slope on two-dimensional photonic crystal slab resonators," USA, 2006, p. 63520P1.
- [39] K.-m. Lim, S. Gupta, C. Ropp, and E. Waks, "Development of metal etch mask by single layer lift-off for silicon nitride photonic crystals," *Microelectronic Engineering*, vol. 88, pp. 994-998, 2011.
- [40] M. Muhammad, S. C. Buswell, S. K. Dew, and M. Stepanova, "Nanopatterning of PMMA on insulating surfaces with various anticharging schemes using 30 keV electron beam lithography," *Journal of Vacuum Science & Technology B*, vol. 29, p. 06F304, Nov 2011.
- [41] H. Yi and J. Chang, "Proximity-effect correction in electron-beam lithography on metal multi-layers," *Journal of Materials Science*, vol. 42, pp. 5159-5164, 2007/07/01 2007.

- [42] H. Nakata, K. Nishioka, and H. Abe, "Plasma etching characteristics of chromium film and its novel etching mode," *Journal of Vacuum Science and Technology*, vol. 17, pp. 1351-1357, 1980.
- [43] K.-H. Kwon, S.-Y. Kang, S.-H. Park, H.-K. Sung, D.-K. Kim, and J.-H. Moon, "Additive oxygen effects in Cl<sub>2</sub> plasma etching of chrome films," *Journal of Materials Science Letters*, vol. 18, pp. 1197-1200, 1999/08/01 1999.
- [44] M. N. Hossain, J. Justice, P. Lovera, B. McCarthy, A. O'Riordan, and B. Corbett, "High aspect ratio nano-fabrication of photonic crystal structures on glass wafers using chrome as hard mask," *Nanotechnology*, vol. 25, p. 355301, Sep 5 2014.

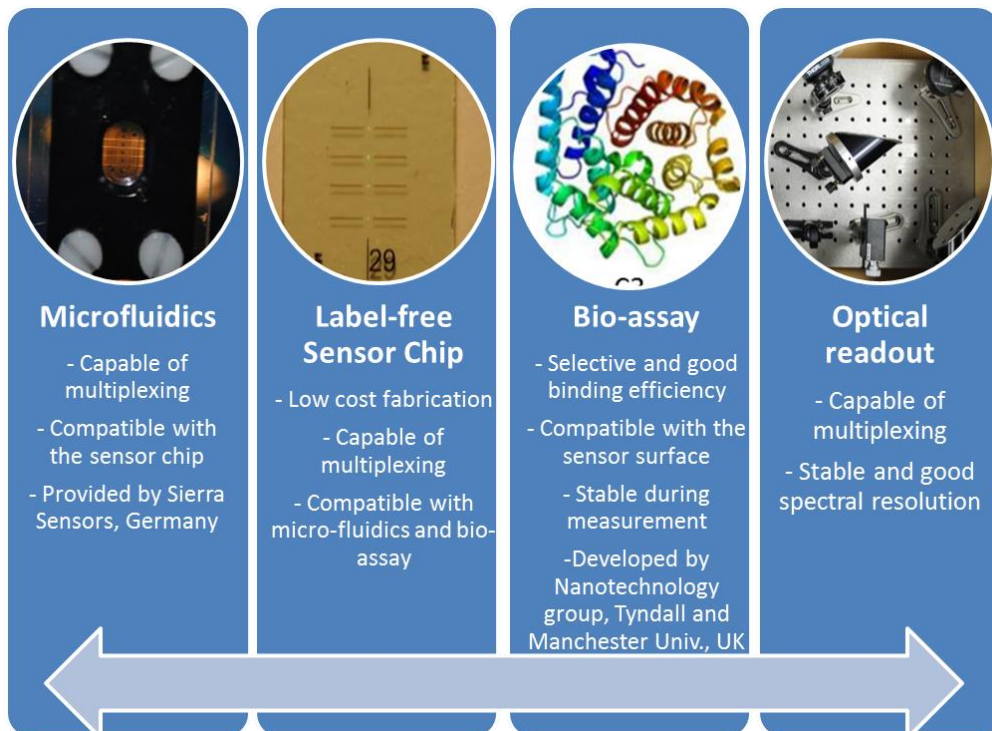
# Chapter 4

## Bio-Characterization of RWG sensor



## 4.1 Introduction

In this chapter, we report on the characterization of the resonant waveguide grating (RWG) as a bulk and surface sensors designed and fabricated in Chapter 2 and Chapter 3 respectively. Fiber based characterization and free space coupling based characterization are presented in Section 4.2.1 and 4.2.2 respectively. Both bulk and surface sensitivities are measured and presented in Sections 4.3 and 4.4. The characterization setup will require 4 main components: the microfluidic delivery system to inject the analyte solution to the sensor surface, the sensor chip itself for detection of the target analyte, selective and binding efficient bio-attachment chemistry, and the optical readout system for interrogating the resonance wavelength shift to quantify the analyte.



This multi-disciplinary project [14] involved the Nanotechnology group from Tyndall National Institute and Chemistry group from Manchester University, UK for developing a selective and efficient bio-assay [138], and Sierra Sensors from Germany to provide the microfluidic liquid delivery system [139]. The abovementioned four components of the characterization setup are interlinked and had to be compatible with one another to have a fully functioning bio-characterization setup. For example, the

multiple sensors in the sensor chip had to be properly aligned with the corresponding microfluidic channels to work properly.

## 4.2 Characterization setup

### 4.2.1 Fiber based Characterization

RWG sensors can be characterized in both transmission as well as in reflection mode because the resonance dip in the transmission spectrum appeared as a resonance peak in the reflection spectrum. The microfluidic setup was also amended (Polydimethylsiloxane, PDMS, material was used so that it was transparent to visible wavelengths) to accommodate optical transmission and reflection measurements. Experiments were initially carried out to assess this reflection based interrogation method. Basically, the RWG sample was loaded in the microfluidic holder and a bifurcated fiber was used to illuminate the sensor and collect the reflected light as shown in Figure 4.2-1. The fiber was connected to a portable spectrometer and reflected spectra was recorded as liquid of different refractive indices were injected into the RWG sensor through the microfluidics. The shift in the resonance reflection spectra was noticed by the spectrometer.

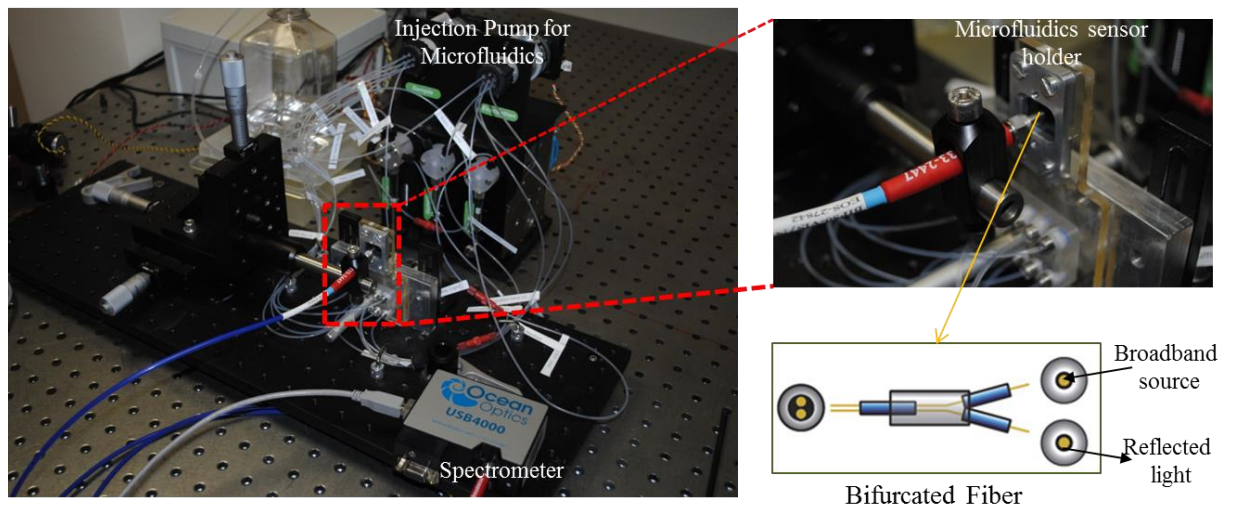


**Figure 4.2-1 Characterization setup in reflection mode uses a bifurcated fiber to get the broadband light in and reflected light (from RWG) out. Fiber tip is aligned to the RWG sensor hold by the microfluidic chamber. Reflected light is analysed by the portable ‘Ocean Optics’ spectrometer.**

The resolution of the spectrometer used here was  $\sim 2\text{nm}$ . The bulk sensitivity could be measured using this setup as the resonance wavelength shift was large in that case but the small shifts expected from the label-free bio-molecule sensing experiments (0.2-2 nm) could



not be detected and so, another optical setup was implemented with high resolution spectrometer. Nevertheless, this type of fiber based characterization setup is used in commercial EPIC® technology [26] but with higher resolution spectrometer. The benefit is that multiple fibers can be aligned with multiple sensors and interrogated at once. These fibers can be bundled together and scan the sensor chip at faster rate which increases the throughput.

### 4.2.2 Bio-characterization Setup

Free space coupling based optical characterization setup with high resolution spectrometer was used for biodetection. The transmittance of the RWG sensor was measured to spectrally locate the position of the resonance. As shown in Figure 4.2-2, a polarized broadband white light source illuminated the sensor grating area and an objective lens collected the light transmitted through the sensor. The sensor was placed in a chamber where microfluidic channels are aligned with the sensor position. Different analyte solutions were injected manually through the microfluidic channels. The spectral location of the resonance was then tracked in the transmission spectrum to know the amount of resonant shift for different analyte solutions. The transmission spectrum was measured in a spectrometer with a resolution of 0.1 nm. The simplified schematic of the characterization setup is shown in Figure 4.2-2.

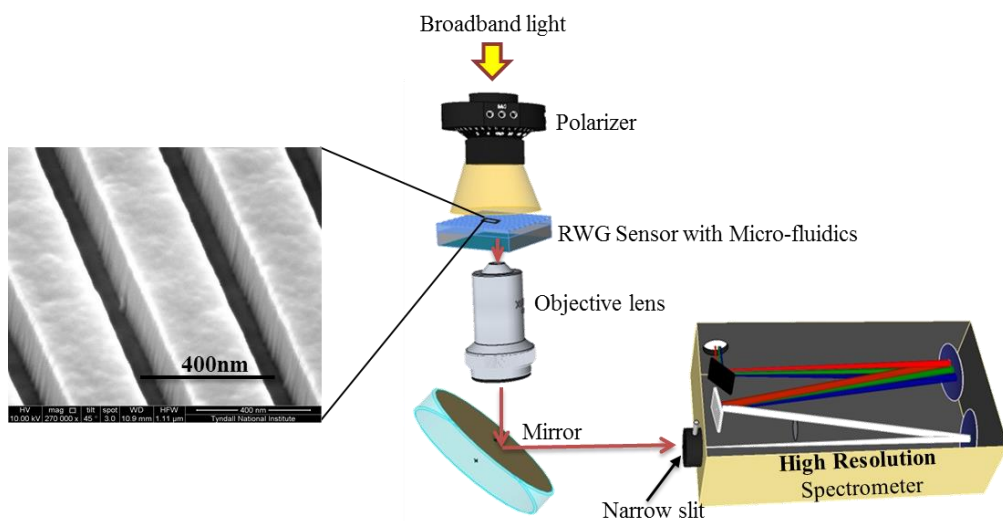


**Figure 4.2-2 Schematic representation of the transmission spectrum measurement setup with high resolution spectrometer for RWG sensor based biodetection.**

The detection limit of the sensor depends on how precisely the spectral shift of the resonance wavelength for bio-attachment can be measured. Both the sharpness of the spectral resonance peak / notch ( $\sim$  Q-factor) and the spectral resolution of the

spectrometer determines the error bar or detection limit of the sensing system. The spectrometer resolution was 0.1 nm in the bio-assay measurement setup which corresponds to the lowest amount of detection of 300 ng/ml (or 0.77 nM) of C1q protein based on the bio characterization shown in 4.4.1.2.1. This can be further improved by using higher resolution spectrometer.

## 4.3 Characterization of RWG sensor

### 4.3.1 Bulk sensitivity

As shown in Figure 4.3-1, the transmission spectrum of the fabricated (by Nanoimprint) RWG sensor gave resonances at the wavelength of 634.9 nm and 754 nm when the sensor was submerged into de-ionized (DI) water whose refractive index is about 1.3319. The change in the refractive index of the wetting liquid shifts the resonance wavelengths. For a salt solution of refractive index of 1.342, the 1<sup>st</sup> resonance wavelength shifted to 637nm. For further increment of the refractive index of the wetting liquid, isopropanol (IPA) of refractive index of 1.3776 was applied and it shifted the wavelength to 643.2 nm. The bulk sensitivity of the sensor is thus calculated as  $(643.2-634.9) \text{ nm}/(1.3776-1.3319) \text{ RIU}=181.6 \text{ nm/RIU}$ . As calculated by simulations in Chapter 2, the bulk sensitivity was expected to be 183.33 nm/RIU for the 1<sup>st</sup> resonance. On the other hand the bulk sensitivity of the 2<sup>nd</sup> resonance was calculated as  $(752.4-750.3)\text{nm}/(1.3776-1.3319) \text{ RIU}=45.9 \text{ nm/RIU}$ . The 2<sup>nd</sup> resonance was actually designed for surface sensitivity and so less sensitive to the bulk refractive index change than the 1<sup>st</sup> resonance. See Chapter 5 for the distinctive use of both resonances in a ‘Dual resonance approach’ for separating bulk and surface sensitivities.

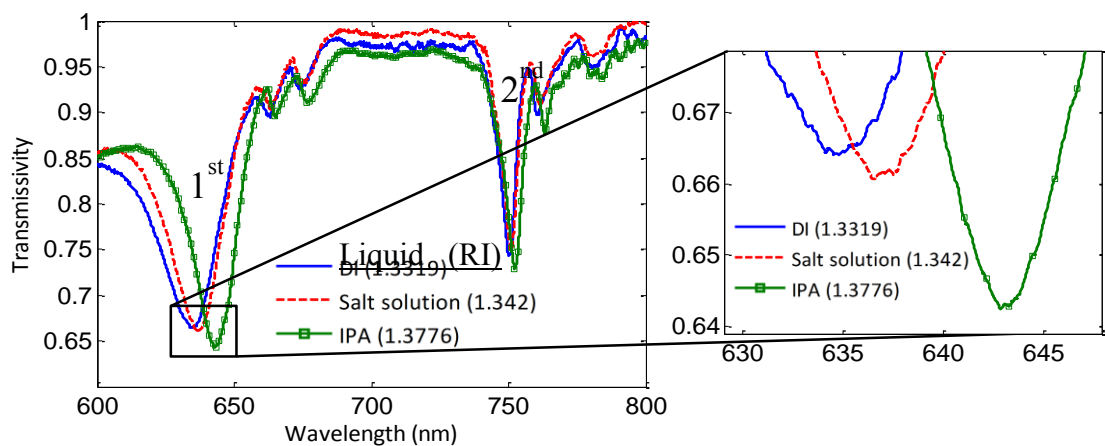


**Figure 4.3-1 Transmission spectrum of the RWG sensor for different sensing liquids to measure the bulk sensitivity.**

## 4.4 Surface Sensitivity

As detailed in Chapter 2, Section 2.6.2 that the surface sensitivity is nothing but the spectral shift of the resonance wavelength for the attachment of a thin layer of bio-molecule on the RWG sensor surface which causes change in the local refractive index (RI) and so shifts the resonance wavelengths.

The SEM image of the fabricated Nano-imprinted sensor (Figure 4.4-1 inset) showed that the dimensions of the fabricated sensor is bit different than designed in Chapter 2. The period, filling fraction and etching depth was found 465 nm, 82%, and 450 nm respectively. These data was given input to the simulator and the RWG sensing performance was modeled again. The simulated transmittance spectrum showed resonance at the wavelength of 688.6 nm considering the RWG sensor is covered by PBS solution. Phosphate-buffered saline (abbreviated PBS) is a water-based salt buffer solution to maintain the pH level so that the proteins can survive. PBS buffer is modeled as a liquid solution of refractive index of 1.332 in the simulator. Then, 20 nm thin conformal layer of biomolecule is added on the sensor surface in simulations to know the amount of resonance shift. The refractive index of the bio-molecule layer is considered as 1.45. The attachment of the 20 nm thin layer shifts (~1.7 nm) the resonance wavelength from 688.6 nm to 690.3 nm as shown in Figure 4.4-1.

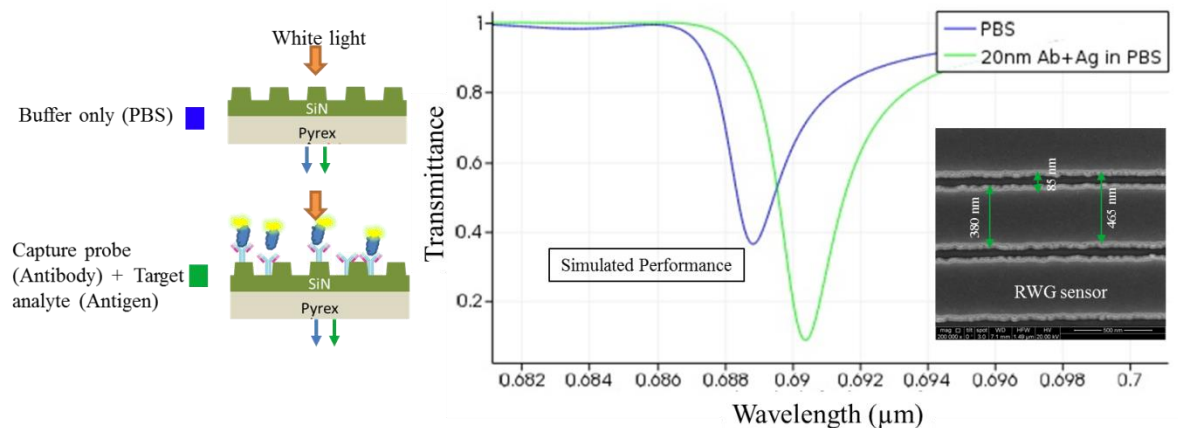


**Figure 4.4-1 Transmittance spectra of the modeled (considering fabricated parameters) RWG sensor for bio-molecular attachment. Simulation shows that 20 nm thin conformal layer of biomolecule added on the sensor surface shifts the resonance wavelength 1.8 nm.**

### 4.4.1 Bio-assay experiment

Immunoglobulin proteins: C1q and C3 antibodies and antigen were selected for bio-assay experiments. The proteins C1q (complement 1q) and C3 (complement 3) are part of the complement system, which is part of the innate immune system. Bio-assays were carried out using both C1q and C3 proteins in PBS solution and C3 protein in serum.

#### 4.1.1.1 Contact angle measurement

Contact angle is the measurement of the wettability of the solid surface by a liquid. For bio-assay experiment, it tells whether the sensor surface is wet enough to let the bio-fluid go inside the nano-structure of the RWG sensor. From the contact angle measurement as shown in Figure 4.4-2a, it was found that the fabricated RWG sensor by the Nano-imprint technology was not wet enough (bit hydrophobic) to do the bio-assay experiment. The contact angle found on average was  $32^\circ$ . However,  $O_2$  plasma treatment at 50W for 3 min made the RWG sensor surface very hydrophilic (contact angle is  $6^\circ$  only) as shown in Figure 4.4-2b.

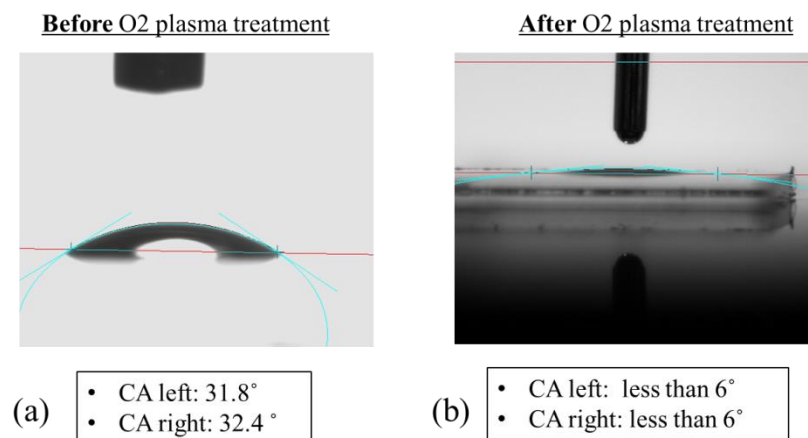


**Figure 4.4-2 Contact angle measurement of the fabricated (by Nano-imprint) RWG sensor: (a) before, and (b) after the  $O_2$  plasma treatment.**

#### 4.4.1.2 Bio-assay experiment in PBS solution

##### 4.4.1.2.1 Adsorption based C1q protein bio-assay experiment

1. RWG sensor was fabricated by nano-imprinting. The size of the sensor was  $200\mu\text{m} \times 200\mu\text{m}$ .
2.  $O_2$  plasma surface treatment at 50W for 3 min which made the sensor surface hydrophilic (contact angle measurement showed  $6^\circ$  angle. See Figure 4.4-2b) favorable for bio-attachment.

3. Bio-attachment experiment was done based on adsorption principle.
4. Transmission spectrum was taken in PBS before antigen immobilization.
5. C1q antigen (Ag) were then attached to the surface of the sensors by incubating the sample with a 4  $\mu\text{g/ml}$  single-chain variable fragment (scFv) C1q Ag solution for two hours. The sample was then washed in PBS buffer.
6. The sample was then rinsed in PBS solution.
7. Transmission spectrum was taken in PBS solution after antigen immobilization.

As shown in Figure 4.4-3, the transmission spectra were taken before and after immobilisation of antigen on the RWG sensor surface. The RWG sensor showed resonance at the wavelength of 695.8 nm. The resonance wavelength shifted from 695.8 nm to 697.1 nm which gave a resonance wavelength shift of 1.3 nm for 4 $\mu\text{g/ml}$  of C1q antigen immobilization. The experimentally found value of resonance shift (~1.3 nm) is bit lower than the simulated value (~1.8 nm) because only antigen was adsorbed on the RWG surface, but in simulation both antibody and antigen was considered.

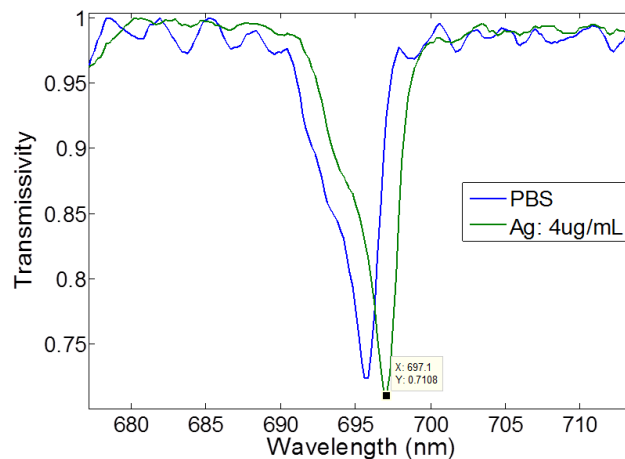


**Figure 4.4-3 Adsorption based bio-assay experiment with RWG sensor. 1.3 nm of resonance wavelength shift was observed for 4 $\mu\text{g/ml}$  of C1q antigen immobilization.**

#### 4.4.1.2.2 EDC coupled C3 protein bio-assay experiment to show selectivity

1-Ethyl-3-(3-dimethylaminopropyl) carbodiimide (EDC) is a water-soluble carbodiimide used as a carboxyl activating agent. In this experiment EDC was used in

combination with N-hydroxysuccinimide (NHS) for the immobilisation of C3 biomolecules.

1. The same type of RWG sensor of size  $200\mu\text{m} \times 200\mu\text{m}$  was used. The sensor was fabricated by nano-imprinting.
2. The sensor surface was modified by single assembled monolayer (SAM) and then photo-patterned (UV light at 365 nm) through optical mask to activate the amino-terminated surface only at the sensing region. The work of surface functionalization [138] was done jointly with University of Manchester, UK.
3. Bio-attachment experiment was done based on EDC coupling. Injection of 200  $\mu\text{l}$  of 200 mM EDC and 25 mM NHS supplied by Sierra Sensors, GmbH, Hamburg to activate the carboxyl groups of the precoated Mercaptohexadecanoic acid (MHDA).
4. EDC/NHC incubation for 30 min.
5. C3 Ab was then attached to the surface of the sensors by incubating the sample with a 7  $\mu\text{g}/\text{ml}$  scFv C3 Ab solution for another two hours.
6. The sample was then incubated for one hour and a half in a 4  $\mu\text{g}/\text{ml}$  solution of C1q antigen in PBS to know the selectivity of the EDC coupled C3 antibody.
7. The sample was then washed in PBS buffer.
8. The sample was then again incubated for one hour and a half in a 4  $\mu\text{g}/\text{ml}$  solution of C3 antigen in PBS. The sample was once again washed in PBS.

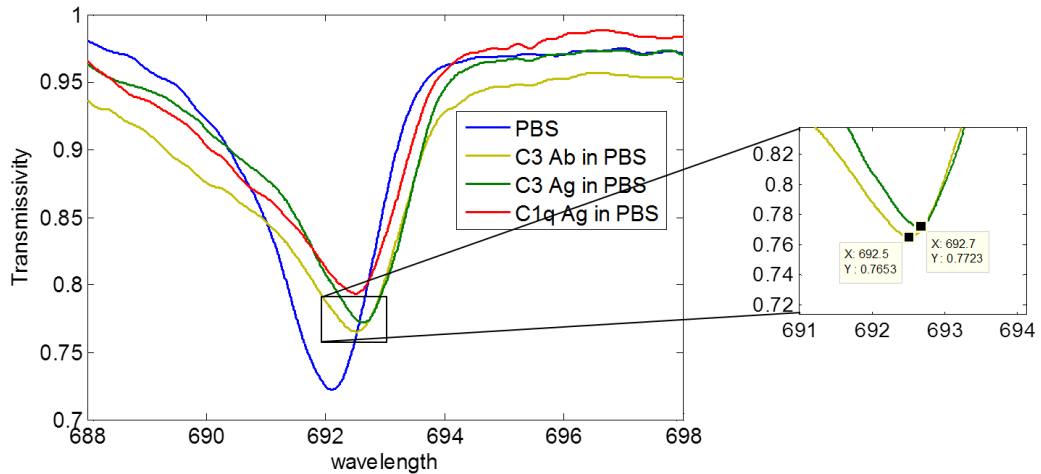


**Figure 4.4-4 EDC coupled bio-assay experiment showed a total of 0.7 nm (0.5 nm for Ab and 0.2 nm for Ag) of resonance wavelength shift for 7 $\mu$ g/ml and 1 $\mu$ g/ml of C3 antibody and antigen attachment respectively. There was no shift for C1q incubation which showed the selectivity of the sensor.**

Transmission spectra in PBS were acquired after each step of the assay. The spectra were taken before and after immobilisation of C3 antibody and again after binding of C3 antigen. The transmittance was also measured after C1q incubation to know whether the attachment was selective or not. Each time the sensor was rinsed in PBS before the spectrum was taken. As shown in Figure 4.4-3, the resonance wavelength shifted 0.5 nm for 7 $\mu$ g/ml of C3 antibody immobilization (step 5 in bio-assay experiment) and further 0.2 nm of resonance wavelength shift was achieved for 1 $\mu$ g/ml C3 Antigen binding (step 8), but there was no shift in resonance for C1q incubation (step 6). So, a total of 0.7 nm of resonance wavelength shift was observed for both antibody and antigen attachment and no shift were observed C1q antigen incubation with C3 antibody which showed the selectivity of the sensor. The bio-assay was also done in serum instead of PBS. The process steps of the serum experiment were same as the EDC coupled C3 experiment upto step 5. Then 0.5% serum was incubated for two hours and got a shift of 0.4 nm from Ab to Ag attachment which was 0.2 nm in C3 experiment.

## 4.5 Summary

The fabricated RWG sensor was characterized for both bulk and surface sensitivity. Among the four components of the characterization setup 'liquid delivery system (Microfluidics)' was done by Sierra Sensors, Germany, a partner of the project.

Whereas, bio-assay development (surface functionalization, bio-attachment) were done by both Nanotechnology group in Tyndall National Institute and a Chemistry group from Manchester University, UK. Optical fiber based reflectance measurement setup was made for characterization. EPIC® technology based biosensors from Corning Inc. use fiber based interrogation system. But, the fiber based spectrometer used in this project was low in resolution (~2 nm) and so was not good enough to use it for biomolecule detection (0.1 nm resolution expected). So, another simple transmittance measurement setup based on free space coupling of light into the RWG sensor was made with high resolution (0.1 nm) spectrometer for bio-assay experiment. The bulk sensitivity of the RWG sensor was measured by changing the refractive index of the liquid on top of the sensor and by measuring the amount of corresponding resonance wavelength shift for that change. The change of refractive index was done by changing liquids from DI water to another salt solution and then replacing that by IPA. The measured bulk sensitivity was 183.3 nm/RIU.

As the fabricated sensor was not exactly the same as designed in Chapter 2, the dimensions of the fabricated RWG was measured by SEM and then those data was used in the simulator to predict the performance of the prepared RWG sensor in bio-assay experiment. Immunoglobulin proteins: C1q and C3 antibodies and antigen both were used in the bio-assay experiments. Bio-assay experiments were done both by adsorption and EDC coupling. From the adsorption experiment 4 µg/ml C1q antigen was easily detected by observing 1.3 nm of resonance wavelength shift. The detection of 4 µg/ml solution of the C1q Antigen (410 kDa) corresponds to detection of just under 10 nM. The spectrometer resolution was 0.1 nm in the bio-assay measurement setup which corresponds to the lowest amount of detection of 300 ng/ml (or 0.77 nM) of C1q protein. This can be improved by using higher resolution spectrometer. Later, C3 antigen of 1 µg/ml was detected in an EDC coupled bio-assay experiment and showed selectivity with C1q proteins. The experiment was done in 0.5% serum and showed successful detection of C3 antigen in serum.

However, the little less amount of resonance shift from the fabricated RWG sensor than the value predicted by the simulator may be attributed to poor bio-attachment. It was found that the EDC coupled RWG sensor was very hydrophobic and this may cause the bio-molecule not to go inside the RWG grating groove and attach on the surface and sidewall. In simulation the total thickness of the attached antibody and antigen layers was assumed to be 20 nm, but the bio-attachment is not static, rather



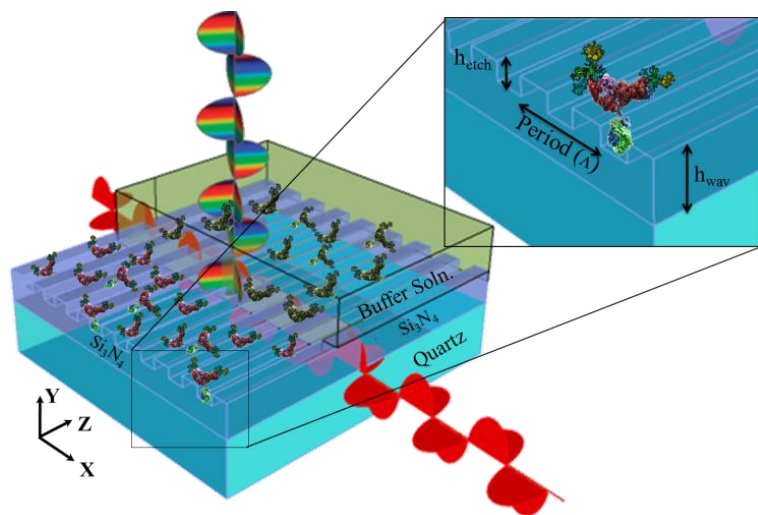
dynamic, and moreover the thickness is protein orientation dependent. So, the thickness of the single-chain variable fragment C3 and C1q proteins (antibody+antigen) may be less than 20 nm of thickness.

## References

- [1] *Robust, affordable photonic crystal sensors for point-of-care disease diagnostics.*  
Available: <http://www.phastid.eu/>
- [2] P. Hazarika, J. M. Behrendt, L. Petersson, C. Wingren, and M. L. Turner,  
"Photopatterning of self assembled monolayers on oxide surfaces for the  
selective attachment of biomolecules," *Biosensors and Bioelectronics*, vol. 53, pp.  
82-89, 2014.
- [3] C. Whalen, "A New form of Microfluidic Sample Delivery for High Throughput  
Biosensor Analysis," *Journal of Physics: Conference Series*, vol. 307, p. 012002,  
2011.
- [4] "[www.corning.com/lifeSciences](http://www.corning.com/lifeSciences)."

# Chapter 5

Dual resonance approach for better sensing



## 5.1 Introduction

Label-free optical sensing based on the guided mode resonance (GMR) property [78, 140, 141] in resonant waveguide grating (RWG) platforms has been used for more than a decade to detect the in-situ binding kinetics of enzymes, viruses and cells [142, 143]. Such sensors have refractive index discrimination down to  $10^{-6}$  refractive index units (RIU) with a large dynamic range [142]. This sensing technique has been incorporated recently in a handheld smartphone based label free portable sensing platform [72]. Utilizing the integrated camera of the smartphone optically aligned with a custom-designed cradle as a spectrometer, accurate and repeatable measurements of shifts in the resonant wavelength of the sensor is demonstrated [72]. Although RWG sensors are widely used for affinity sensing, the information obtained by the present mono-polarized single resonance technique is limited [71].

The resonance wavelength value (RWV) of the sensor is readily tuned by a change in the optical density of the medium lying within the range of the evanescent electric (E) field. Therefore, in addition to refractive index (RI) changes associated with the surface-bound target biomolecular material, thermal induced RI changes of the bulk liquid medium covering the sensor will also induce a shift in the RWV. This could be a significant problem in portable diagnostic applications where thermal variations are likely. The suppression of this unwanted noise will be especially important for applications requiring the detection of small molecules or ultralow analyte concentrations. A PhC sensor with an enhanced surface-to-bulk sensitivity [144] has been reported to suppress the noise coming from the bulk solution in the near ultra-violet wavelength region. By modifying the device structure and, hence, the evanescent electric field profile, the sensitivity characteristics of the biosensor was modified in [144]. They scale down the IR biosensor to curb down the extent of the evanescent electric field since the field extent is proportional to the resonant wavelength for a given angle of incidence and thereby enabled operation only at short wavelengths (UV) [144].

However, a single resonance of polarized light, normally used for detection, cannot simultaneously resolve changes in the biolayer and the surrounding in one measurement. R. Magnusson et al. [71] have proposed a dual (TE and TM) polarization based approach to determine individual attributes of the bulk and surface changes.

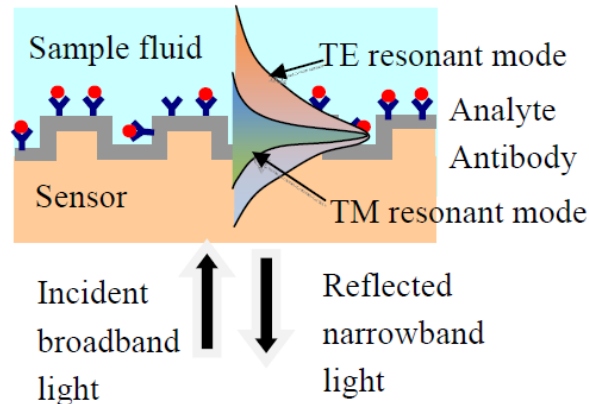


**Figure 5.1-1 Schematic of a RWG sensor system. The collimated beam from a broadband source is incident on the sensor at normal incidence. The reflected spectral response is monitored in real time with an optical spectrum analyzer. As binding events occur at the sensor surface, the resonance peak shift is tracked.**

The peaks result from individual, polarization-dependent resonant leaky modes that are the foundation of their technology. The unique responses of these two peaks to the biomolecular event enrich the data set available for event quantification. Thus, by modeling the binding event and fitting to a rigorous electromagnetic formalism, the individual attributes of the biolayer and its surroundings were determined and thus, a separate reference site for background monitoring was avoided [71]. Though further improvement of their backfit model was suggested [71] for precise separation of the attributes of the biolayer and its surroundings, fundamentally, the spatial electric field distribution of the TE and TM resonant modes are not distinctive enough for accurate decoupling of these contributions.

In this chapter, I present a dual resonance (Section 5.2.1) based discrimination method (Section 5.4) which monitors the response of two spatially (electric field) and spectrally different resonance modes to decouple the interfering surface and bulk attributes. One resonance acts as a bulk sensor because of its larger electric field penetration depth into

the bulk solution whereas the other resonance serves mostly as a surface sensor. This approach also avoids the need of a separate reference site for background monitoring. In a controlled experimental (Section 5.4.1) test of the dual-mode operation, we differentiate the thickness of a deposited thin layer (imitates as a bilayer) on the sensor surface, with a superimposed bulk refractive index variation as a perturbation. The proposed dual resonance approach is also compared with the polarization based discrimination method in Section 5.4.2.

## 5.2 Design

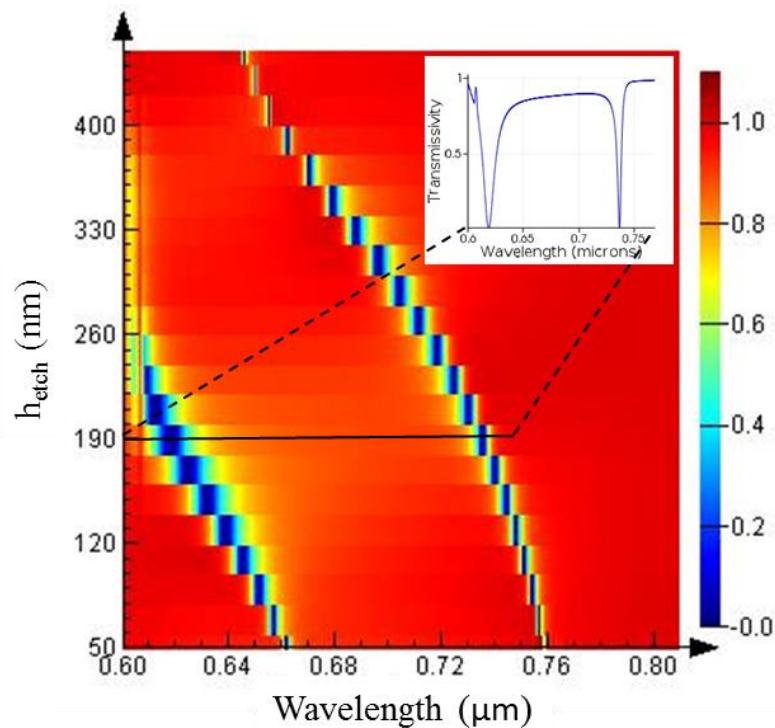
As discussed earlier in Chapter 2 a RWG sensor is a subwavelength grating structure in a single or multilayer waveguide film designed to create a narrow resonant reflection peak at a selected wavelength of certain polarization. When the light is incident upon a subwavelength grating, the zeroth order of the diffracted light follows the Snell's law of refraction while the higher order diffracted light is either guided by the waveguide of the RWG waveguide or becomes evanescent based on the grating and waveguide parameters. At the resonance wavelength, the strong coupling between the external propagating waves (zeroth order) and the adjacent evanescent waves (higher order) produces the rapid increase in the reflectance and concomitant decrease in transmittance.

### 5.2.1 Dual resonance RWG

As mentioned in the Section 2.4.1 the dual resonance in the RWG originates from two sustainable waveguide modes determined by the waveguide layer thickness ( $h_{\text{wav}}$ ) and etching depth ( $h_{\text{etch}}$ ). The device parameters are chosen such that  $m = \pm 1$  are the only diffraction orders existing in the waveguide. Both of the degenerate resonant leaky modes are from the same diffraction order ( $\pm 1$ ) but with different sustainable waveguide modes in the  $\text{Si}_3\text{N}_4$  waveguide layer at two different wavelengths. The  $\text{TE}_{+1,1}$  and  $\text{TE}_{-1,1}$  modes as well as  $\text{TE}_{+1,2}$  and  $\text{TE}_{-1,2}$  modes are degenerate due to the symmetry at normal incidence. Here, for  $\text{TE}_{m,a}$ , 'm' refers to the diffraction order and 'a' refers to the sustainable mode number.

When the diffracted light from the grating structure is coupled with a leaky waveguide mode satisfying the phase-matching condition, sharp resonance peak/dips are observed at particular wavelengths in the reflection and transmission spectra [78]. Incident light at the resonance wavelength becomes spatially confined in a mode which generates a high optical field at the sensor surface. This localized electric field extends evanescently a short distance into the test analyte sample. This leads to a strong interaction between the structure and adsorbed biomaterial and to the ability to perform high resolution sensing of protein and cell attachment.

The RWG sensor designed for our experiment consists of a partially etched subwavelength grating structure in a thin layer of silicon nitride ( $\text{Si}_3\text{N}_4$ ) deposited on a quartz substrate as shown in Figure 5.1-1. For a 55% filling fraction grating with  $\Lambda = 420$  nm and  $h_{\text{wav}} = 450$  nm,  $h_{\text{etch}}$  is varied to investigate its role in the resonance spectra.



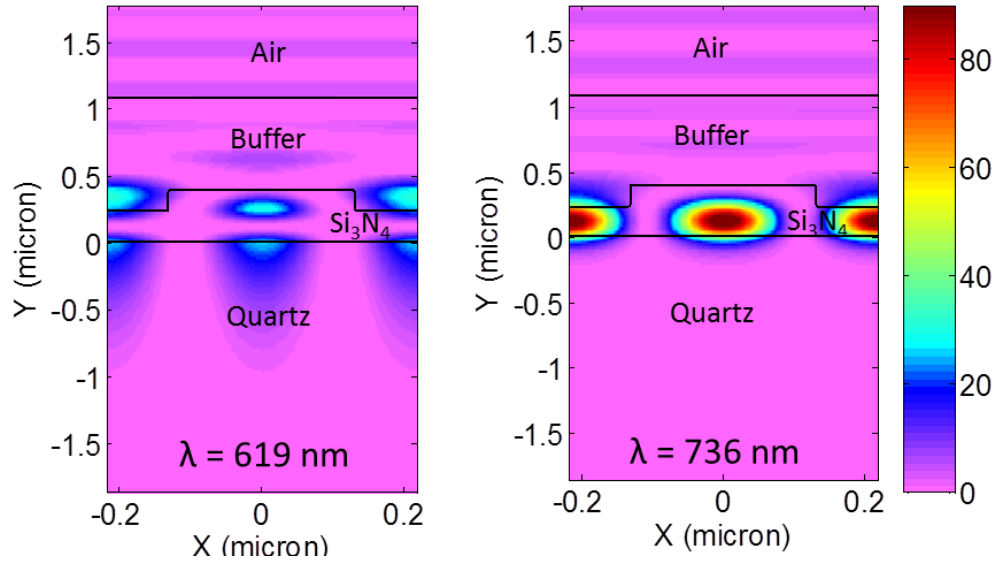
**Figure 5.2-1** Transmission spectra map showing the resonance wavelengths (blue coloured regions shows resonance dips) for different etch depths. Inset shows the transmission spectrum for an etching depth of 190nm

Figure 5.2-1 shows transmission spectra mapping of the sensor for different etching depth carried out using a finite-difference time-domain (FDTD) simulator [35]. *FDTD Solutions* is a 3D Maxwell solver, capable of analyzing the interaction of UV, visible, and IR radiation with complicated structures employing wavelength scale features.

For shallow etching (up to 250 nm) the sensor sustains two resonances whereas for deep etching (depth greater than 250 nm) the 1<sup>st</sup> resonance fades out while the 2<sup>nd</sup> resonance is sustained. As the etching depth increases the effective index of the Si<sub>3</sub>N<sub>4</sub> waveguide layer reduces and so the resonance wavelength shifts to lower wavelength. The full width half maximum (FWHM) of the resonance peaks also change with etching depth.

A doubly resonant [145] RWG sensor with an etching depth of 190 nm is studied further with a view to exploiting the distinctive electric field of the two resonances for separating bulk and surface sensitivity. Figure 5.2-2 shows the distinctive E-field distribution of the two resonance modes when illuminated by a mono-polarized (E-field parallel to the grating lines) broadband planewave light source. The resonances are found at wavelengths of 619 nm and 736 nm which are distinctive by their spectral shape (FWHM) (Figure 5.2-1 inset) and electric field distribution (Figure 5.2-2). The 1<sup>st</sup> resonance (at 619 nm) acts as a bulk sensor because of its higher E-field penetration depth into the bulk solution whereas the 2<sup>nd</sup> resonance (at 736 nm) serves mostly as a surface sensor.





**Figure 5.2-2 E-field distribution of PhC unit cell with an etching depth of 190 nm resonating at wavelengths ( $\lambda$ ) of 619 nm and 736 nm.**

### 5.3 Fabrication of dual resonance RWG

The RWG is patterned by electron beam lithography and then the pattern is transferred into the  $\text{Si}_3\text{N}_4$  layer by a nano-fabrication technique [137] where Chrome is used as the hard mask. Please see Chapter 3 for detail of the fabrication procedure.

### 5.4 Decoupling bulk and surface contribution

To validate the dual-mode operation in biosensing, we differentiate the thickness of the attached thin layer on sensor surface, with superimposed bulk refractive index variation as a perturbation [146]. The shift in the resonance wavelength occurs because of refractive index (RI) changes of the bulk liquid medium and the formation of thin layer of biomolecules on the sensor surface as schematically shown in Figure 5.4-1.

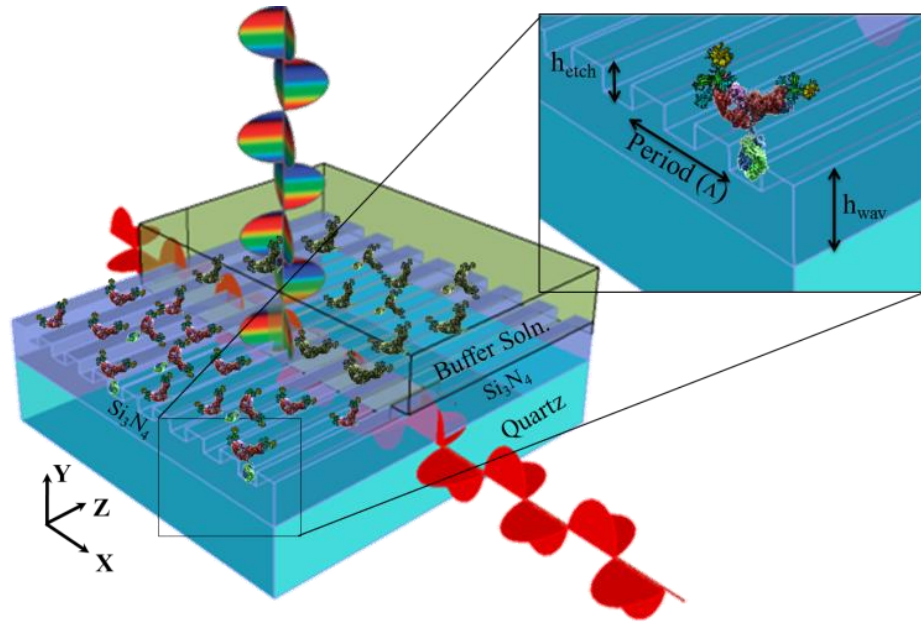


**Figure 5.4-1 Schematic of the PhC biosensor where  $\Lambda$  = period of the grating,  $h_{\text{etch}}$  = etching depth,  $h_{\text{wav}}$  =  $\text{Si}_3\text{N}_4$  waveguide layer thickness. The buffer solution on top contains the bioanalytes. (The antibody-antigen complexes shown in the schematic are not at the same scale as the grating)**

The functional dependence of the measured wavelength shift ( $\Delta\lambda$ ) of each resonance as the result of both the change in added layer thickness ( $\Delta d$ ) and bulk index ( $\Delta n_b$ ) is expressed as:

$$\begin{pmatrix} \Delta\lambda_1 \\ \Delta\lambda_2 \end{pmatrix} = \begin{pmatrix} \frac{\partial\lambda_1}{\partial d} \frac{\partial\lambda_1}{\partial n_b} \\ \frac{\partial\lambda_2}{\partial d} \frac{\partial\lambda_2}{\partial n_b} \end{pmatrix} \times \begin{pmatrix} \Delta d \\ \Delta n \end{pmatrix} \quad (5.1)$$

The subscripts 1 and 2 in Eq. 5.1 denote the 1<sup>st</sup> and 2<sup>nd</sup> resonance respectively. The respective differential values of the matrix in Eq. 5.1 can be obtained by linearly changing the added layer thickness and RI of bulk solution. This can be done either from the FDTD simulations shown in Figure 5.4-2a and Figure 5.4-2b or from experimental measurements. Based on these differential values and the shift of each resonance peak found from the experiment, the added layer thickness and the bulk index change can be calculated from a single experiment using Eq. 5.1.

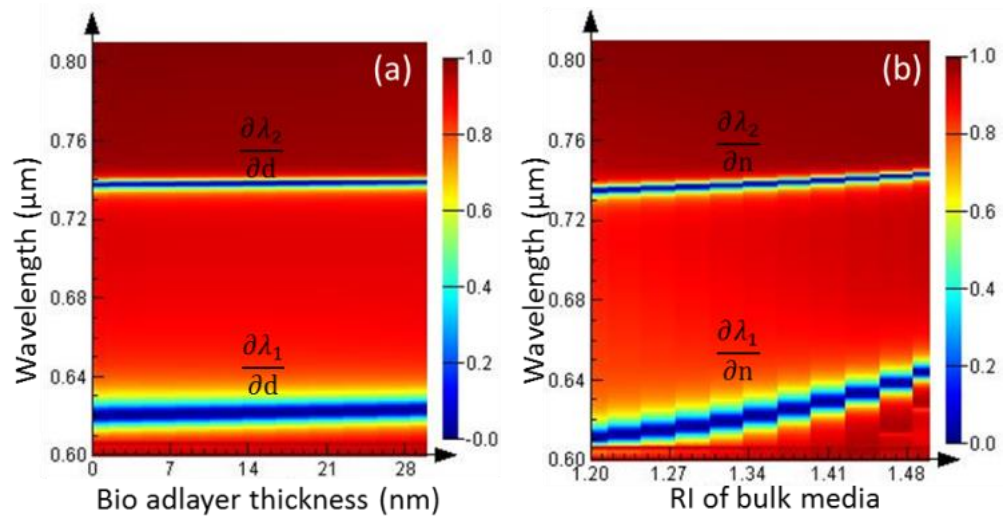


**Figure 5.4-2** Map of the transmission spectrum of the PhC sensor for (a) different added layer thickness,  $\Delta d$  and (b) RI of bulk medium,  $n$ .

The transmission spectrum of the sensor with DI water on top (Figure 5.4-3) shows two resonances at the wavelength of 618.6 nm and 739.4 nm. The experimentally found 1<sup>st</sup> RWV matches with the model, but the 2<sup>nd</sup> RWV is few nm longer than that of the simulated (Figure 5.2-1) value. The FWHM of the 1<sup>st</sup> resonance (Figure 5.4-3) is also broader than that calculated (Figure 5.2-1) unlike the 2<sup>nd</sup> resonance. This can be associated with the sidewall roughness of the grating lines and the spatial position of E-field of each resonance.

### 5.4.1 Controlled experiment

A 16 nm thin layer of silicon dioxide ( $\text{SiO}_2$ ) of RI 1.45 comparable to the RI of biomolecules is coated on the sensor surface. The transmission spectrum of the thin layer coated sensor is measured again with different bulk solution to imitate the scenario of a bulk index perturbation during biomolecular attachment. The bulk solution on top of the sensor is changed from DI water (RI=1.332) to isopropyl-alcohol (RI=1.3776). The change in both bulk index and surface layer together yield a total RWV shift of 10.4 nm and 1.9 nm for the 1<sup>st</sup> and 2<sup>nd</sup> resonance respectively.

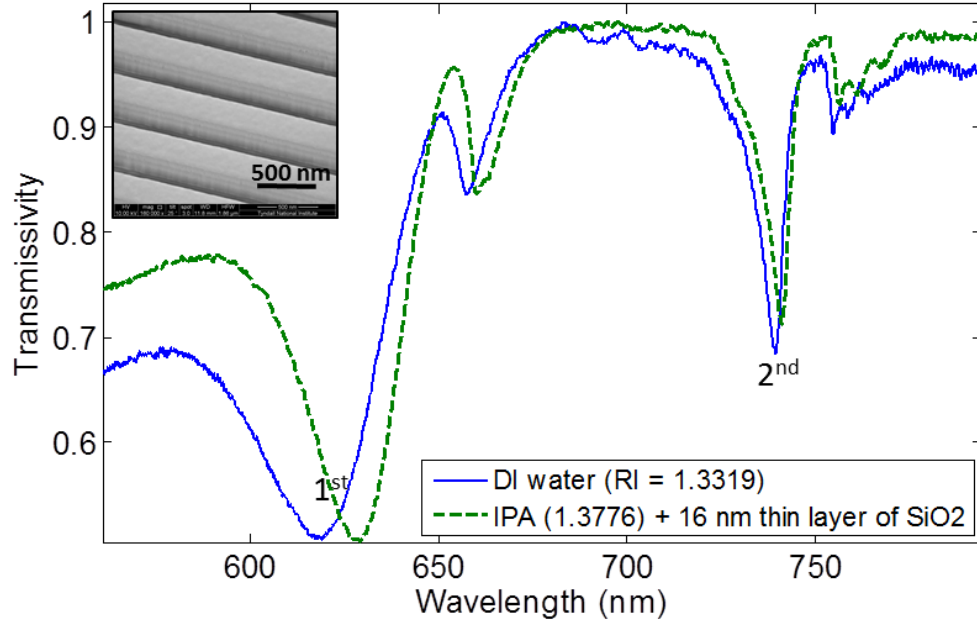


**Figure 5.4-3 Resonance wavelengths shift when the bulk solution is changed from DI water to IPA along with a thin added layer (16 nm) on the sensor surface. Inset shows the SEM image of the sensor grating.**

Sensors based on single resonance cannot distinguish between the individual contributions from surface and bulk. But, the two resonance approach provides separate values of additional layer ( $\Delta d$ ) and index change ( $\Delta n_b$ ) by monitoring the RWV shift of both resonances. The respective differential values (listed below) of the matrix in Eq. 5.1 have been obtained from a separate experiment on the fabricated sensor where the RI of the bulk solution and the added layer thickness are linearly changed individually (RI : 1.33  $\rightarrow$  1.38 and  $\Delta d$  : 0  $\rightarrow$  16 nm) and the change in resonance wavelengths are measured.

$$\frac{\partial \lambda_1}{\partial d} = 0.04375; \quad \frac{\partial \lambda_1}{\partial n_b} = 205.7 \text{ nm/RIU}$$

$$\frac{\partial \lambda_2}{\partial d} = 0.05; \quad \frac{\partial \lambda_2}{\partial n_b} = 21.9 \text{ nm/RIU}$$

Here, the sensitivity of the 1<sup>st</sup> resonance to the surrounding bulk index, ( $\partial \lambda_1 / \partial n_b$ ) is 10 times higher than that of the 2<sup>nd</sup> resonance ( $\partial \lambda_2 / \partial n_b$ ). This is due to the distinctive nature

of the E-field distribution of the 1<sup>st</sup> resonance which has higher penetration depth into the bulk solution compared to the 2<sup>nd</sup> resonance.

Using the measured resonance shift of  $\Delta\lambda_1=10.4$  nm and  $\Delta\lambda_2=1.9$  nm (Figure 5.4-3), Eq. 5.1 gives the added layer thickness and bulk RI change as:

$$\begin{pmatrix} \Delta d \\ \Delta n_b \end{pmatrix} = \begin{pmatrix} 17.5 \text{ nm} \\ 0.0467 \end{pmatrix} \quad (5.2)$$

The dual resonance approach thus could follow the change in both bulk and surface properties taking into consideration the amount of shift in the 1<sup>st</sup> and 2<sup>nd</sup> resonances and their interdependency. The proposed method calculates the added layer thickness as 17.5 nm and bulk RI change as 0.0467 which are very near to the engineered perturbation values of 16 nm and 0.0457.

### 5.4.2 Comparison with the polarization based approach

In order to compare the dual resonance scheme with the polarization based approach presented in [71], the bulk (surrounding index) sensitivity for TM and TE polarization are measured. This is done for the 2<sup>nd</sup> resonance because this sharp resonance with its particular E-field distribution is typically used for RWG based biosensing.

**Table 5.4-1 Sensitivity comparison of two different approaches to bulk index**

Dual resonance approach		Polarization based approach	
1 <sup>st</sup> resonance	205.7 nm/RIU	TM resonance	54.7 nm/ RIU
2 <sup>nd</sup> resonance	21.9 nm/ RIU	TE resonance	21.9 nm/ RIU
$1^{\text{st}} : 2^{\text{nd}} = 9.4$		$\text{TM} : \text{TE} = 2.5$	

As shown in table 1, the dual resonance approach gives sensitivity ratio of 9.4 whereas the polarization based approach can offer 2.5. The higher contrast in the bulk sensitivity for the dual resonance approach helps decouple the attributes of the biolayer and its

surroundings leading to increased detection accuracy and reduced probability of false readings in bioassay experiments.

## 5.5 Summary

In summary, the number of resonance modes of a multi-order, multi-mode RWG is tuned by changing the thickness of the waveguide layer. The proposed dual resonance RWG sensor sustains two resonance modes with their E-field distribution being distinctive in a way that one acts as a bulk sensor whereas the other behaves primarily as a surface sensor. Taking benefit of the different behavior of the two co-existing resonances, a new approach to separating bulk and surface properties is proposed and validated. It leads to a self-referenced biosensor robust against environmental background noise. Furthermore, multiple resonances in combination with different polarizations with resulting diverse E-field distributions of interest could lead to a better understanding of the biomolecular interaction. This multi-parametric approach to biosensing will assist in revealing additional information in proteomics and clinical diagnostic applications instead of just quantifying the analytes.

## References

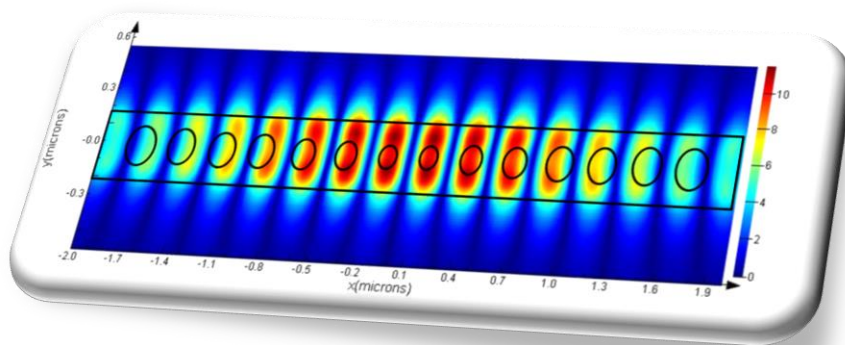
- [1] S. S. Wang and R. Magnusson, "Theory and applications of guided-mode resonance filters," *Applied Optics*, vol. 32, p. 2606, 1993.
- [2] Y. Ding and R. Magnusson, "Resonant leaky-mode spectral-band engineering and device applications," *Optics Express*, vol. 12, pp. 5661-5674, 2004/11/15 2004.
- [3] A. Ricciardi, S. Campopiano, A. Cusano, T. F. Krauss, and L. O'Faolain, "Broadband Mirrors in the Near-Infrared Based on Subwavelength Gratings in SOI," *IEEE Photonics Journal*, vol. 2, pp. 696-702, 2010.
- [4] B. Cunningham, B. Lin, J. Qiu, P. Li, J. Pepper, and B. Hugh, "A plastic colorimetric resonant optical biosensor for multiparallel detection of label-free biochemical interactions," *Sensors and Actuators B-Chemical*, vol. 85, pp. 219-226, Jul 25 2002.
- [5] Y. Fang, A. M. Ferrie, and G. S. Li, "Probing cytoskeleton modulation by optical biosensors," *Febs Letters*, vol. 579, pp. 4175-4180, Aug 1 2005.
- [6] D. Gallegos, K. D. Long, H. J. Yu, P. P. Clark, Y. X. Lin, S. George, *et al.*, "Label-free biodetection using a smartphone," *Lab on a Chip*, vol. 13, pp. 2124-2132, 2013.
- [7] R. Magnusson, D. Wawro, S. Zimmerman, and Y. Ding, "Resonant photonic biosensors with polarization-based multiparametric discrimination in each channel," *Sensors (Basel)*, vol. 11, pp. 1476-88, 2011.
- [8] N. Ganesh, I. D. Block, and B. T. Cunningham, "Near ultraviolet-wavelength photonic-crystal biosensor with enhanced surface-to-bulk sensitivity ratio," *Applied Physics Letters*, vol. 89, pp. -, 2006.
- [9] Z. S. Liu and R. Magnusson, "Concept of multiorder multimode resonant optical filters," *Ieee Photonics Technology Letters*, vol. 14, pp. 1091-1093, Aug 2002.
- [10] S. Boonruang, A. Greenwell, and M. G. Moharam, "Multiline two-dimensional guided-mode resonant filters," *Applied Optics*, vol. 45, pp. 5740-5747, Aug 1 2006.

- [11] A. Greenwell, S. Boonruang, and M. G. Moharam, "Control of resonance separation over a wide spectral range in multiwavelength resonant grating filters," *Applied Optics*, vol. 46, pp. 6355-6361, Sep 1 2007.
- [12] R. Magnusson, "Spectrally dense comb-like filters fashioned with thick guided-mode resonant gratings," *Optics Letters*, vol. 37, pp. 3792-3794, Sep 15 2012.
- [13] J. Homola, "Surface Plasmon Resonance Sensors for Detection of Chemical and Biological Species," *Chemical Reviews*, vol. 108, pp. 462-493, 2008.
- [14] M. N. Hossain, J. Justice, P. Lovera, M. Mitchell, A. Oriordan, and B. Corbett, "Two Color Approach to Separating Surface and Bulk Sensitivity in a Photonic Crystal Biosensor," in *Frontiers in Optics 2013*, Orlando, Florida, 2013, p. FM4E.5.
- [15] M. N. Hossain, J. Justice, P. Lovera, B. McCarthy, A. O'Riordan, and B. Corbett, "High aspect ratio nano-fabrication of photonic crystal structures on glass wafers using chrome as hard mask," *Nanotechnology*, vol. 25, p. 355301, Sep 5 2014.
- [16] M. N. Hossain, J. Justice, P. Lovera, A. O'Riordan, and B. Corbett, "Dual resonance approach to decoupling surface and bulk attributes in photonic crystal biosensor," *Opt Lett*, vol. 39, pp. 6213-6, Nov 1 2014.



# Chapter 6

## Resonant nano-ribbon cavity



## 6.1 Introduction

The resonant nano-ribbon cavity which is a form of 1-D Photonic crystal (PhC) cavity [22, 23, 57, 58], has been demonstrated as a significant alternative to the 2D slab based PhC cavity [25, 26]. 1-D PhC cavity can achieve Q as high as those found in the slab based geometries but with much smaller footprint [22] which is beneficial for small analyte detection. It has already found its application not only in bio-sensing [24, 59], but also in opto-mechanics [60], optical trapping [61] and opto-fluidics [62] etc. Furthermore, it has a naturally convenient geometry for integration with an optical waveguide.

In this chapter, a waveguide embedded resonant nano-cavity is proposed to be integrated on a  $\text{Si}_x\text{N}_y$  waveguide on glass substrate. The design of the cavity and the methodology of calculating the Quality (Q) factor of the cavity are detailed in Section 6.2. Sections 6.2.2 - 6.2.4 present the effect of different cavity parameters (e.g., Bragg mirror strength, cavity length etc.) on the Q-factor of the cavity. Grating coupler is used as an in/out component and Section 6.3 presents the design and optimization scheme of coupling efficiency of the single layer uncladded  $\text{Si}_x\text{N}_y$  grating coupler. The fabrication of the nano-ribbon cavity along with the grating couplers was attempted by using nano-imprint lithography technique in VTT, Finland and the pattern transfer technology presented in Chapter 3, in Tyndall National Institute, Ireland. The results of the nano-imprinting and pattern transferring of different components at different stages are presented in Section 6.4.1 and 6.4.2 respectively.

## 6.2 Design of the nano-ribbon cavity

The proposed nano-ribbon cavity has PhC component (Figure 6.2-1a) embedded into a nanowire (~300 nm in width) waveguide which is elongated couple of millimeter (mm) and expanded to a wider waveguide (~20  $\mu\text{m}$  in width) to make easier coupling of incoming and outgoing light using grating couplers. Similar grating couplers (Figure 6.2-1c) tuned to the PhC cavity resonance wavelength, are placed at both sides of the long waveguide (Figure 6.2-1b) to facilitate the in and out-coupling of light.

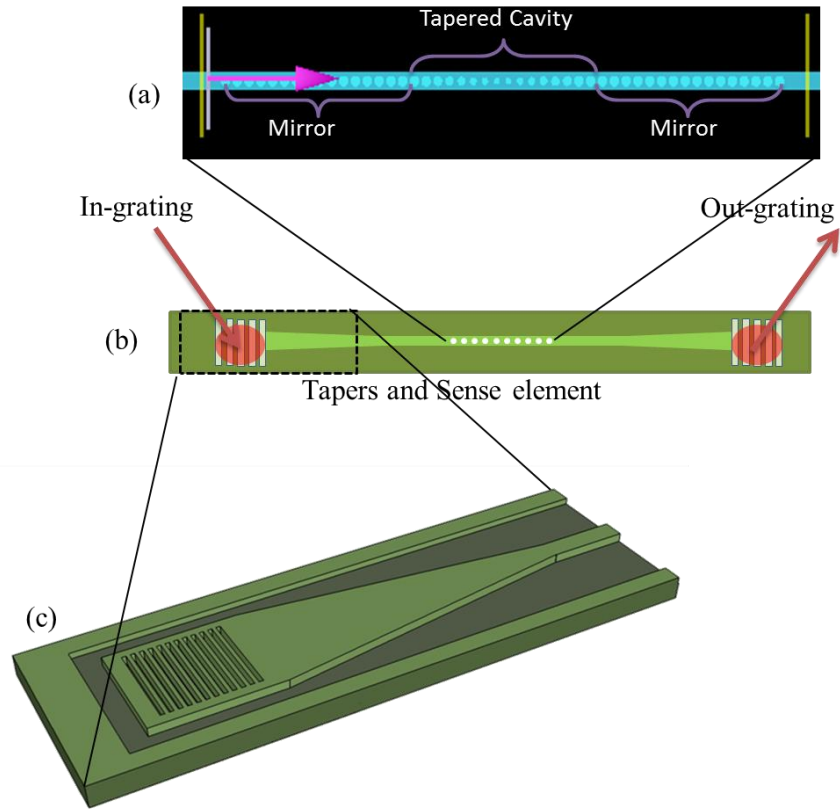


**Figure 6.2-1 Schematic of nano-ribbon PhC cavity with in and out-coupling grating at two sides (a) 1-D PhC cavity with Bragg mirrors at both ends, (b) PhC cavity integrated with tapered waveguide and coupling grating, and (c) grating coupler with tapered waveguide.**

The cavity section at the center is sandwiched between two Bragg mirrors. The Bragg mirrors confine light in the waveguide direction (X-axis) whereas the total internal reflection in the  $\text{Si}_x\text{N}_y$  waveguide restrains light to escape in the other two directions (Y & Z axes) (see Figure 6.2-2).

The light is coupled into the  $\text{Si}_x\text{N}_y$  waveguide by grating coupler and travels as a fundamental waveguide mode. For the wavelength allowed by the PhC, the mode is then transformed into PhC Bloch mode while passing the PhC Bragg mirror. When the forward propagating PhC Bloch mode passes the Bragg mirror section and enters into the cavity section, the transverse (Y-Z plane) Bloch mode is to be transformed into the cavity waveguide mode to sustain the resonance. Then the cavity mode is reflected back and forth by the Bragg mirror and builds up in the cavity as a resonant mode. While being

reflected by the mirror, additional Bloch modes are excited at the abrupt interface in between the Bragg mirror and the cavity section because of the transverse modal mismatch of the Bloch mode and the cavity waveguide mode, and inevitably some light leaks out in the cladding dropping down the Q-factor.

Two tapered lines of air holes acting as partial mirrors, are placed face to face in the cavity section to reduce the abrupt changes in between the effective refractive index of the cavity waveguide mode and the PhC Bloch mode [147]. So, adiabatic transition between these two modes is obtained minimizing the scattering loss and so, high Q cavity is achieved.

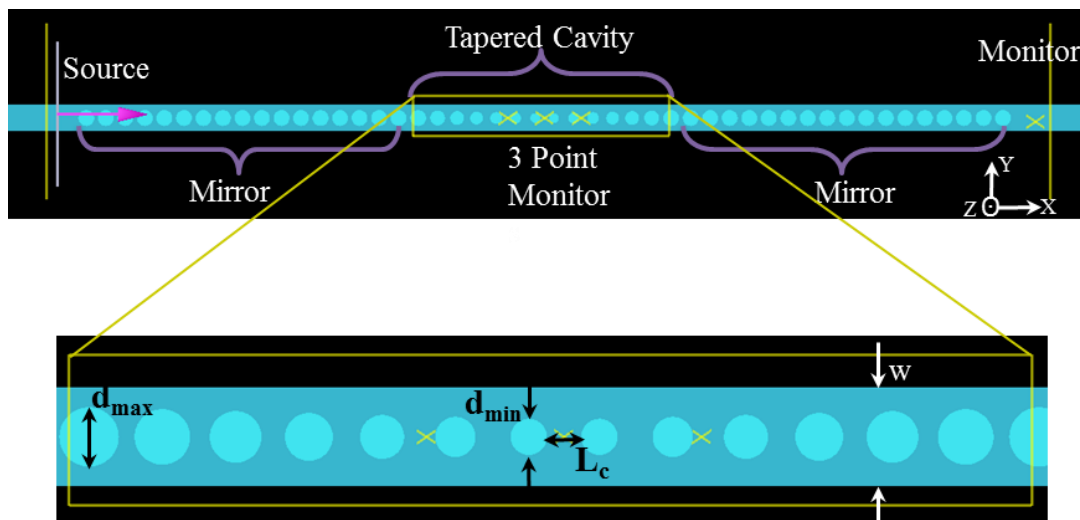


**Figure 6.2-2 Schematic of the simulation setup of the nano-ribbon cavity with Bragg mirror at two sides and linearly tapered line of air holes placed face to face in the cavity. In simulations, a waveguide mode is injected from left end and a monitor is placed at the right side to measure the transmissivity. Three point monitors are included at the cavity section to measure the decay rate of the resonant mode for calculating the Q-factor.**

The nano-ribbon width ‘w’ and waveguide thickness ‘h’ are fixed as 300 nm and 400 nm respectively to ensure single mode operation of the waveguide in water/buffer solution background (for biosensing) at the wavelength of 850 nm as shown in Figure 6.2-3. The photonic crystal Bragg mirrors are realized by means an array of circular holes of number ‘N’ in a line at both sides of the cavity (Figure 6.2-2). The Bragg mirror strength increases with the number of air holes included in the mirror. The period (spacing between two consecutive holes) ‘p’ and the hole diameter ‘d’ in the Bragg mirror are fixed to 260 nm

and 220 nm respectively in order to center the resonance around 850 nm. The tapered holes (linearly decreasing in diameter along the line) are symmetrically located at the center with respect to the nanocavity and each taper is constituted by ‘ $N_t$ ’ number of circular air holes of decreasing diameter. The effective cavity length increases with the number of tapered air holes,  $N_t$ . The largest hole is of diameter ( $d_{max}$ ) of 220 nm and the smallest one ( $d_{min}$ ) is 120 nm as shown in Figure 6.2-2. The separation length ( $L_c$ ) of the two smallest air holes at the center of the cavity (Figure 6.2-2) is initially set to 100 nm and later  $L_c$  is varied to maximize the Q-value. However, the ribbon is considered to be sitting on glass substrate and surrounded by water because the designed nano-ribbon cavity sensor is intended to be used for bio-molecule diagnosis.

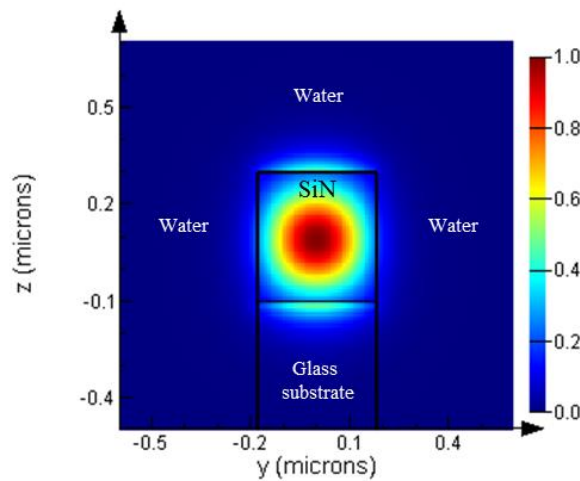


**Figure 6.2-3 Transverse E-field distribution (fundamental mode) of the nano-ribbon waveguide sitting of glass (AF32) substrate. The height ( $h$ ) and width ( $w$ ) of the  $Si_xN_y$  waveguide are 400 nm and 300 nm respectively. The waveguide is considered to be submerged in water for biosensing application.**

The numerical analysis of these structures was performed by a three-dimensional Finite Difference Time Domain (FDTD) simulator, Lumerical FDTD Inc. [12]. The computational domain is bounded by perfectly matched layers (PMLs) all around the nano-ribbon. The fundamental waveguide mode (Figure 6.2-3) is injected by a modal source from one end of the waveguide and the transmitted light is collected by a monitor at the other end as shown in Figure 6.2-2.

### 6.2.1 Calculation of the Quality factor (Q)

The cavity Quality factor can be defined as

$$Q = \frac{\omega_r}{\Delta\omega} \quad (6.1)$$

where  $\omega_r$  is the resonant frequency ( $\omega_r = 2\pi f_r$ ) and  $\Delta\omega$  is the full width half maximum (FWHM) of the resonance intensity spectrum.

From the simulation point of view, for a high Q cavity, the electromagnetic fields do not completely decay within the simulation time ( $T_{sim}$ ) that could be reasonably simulated by FDTD. The  $T_{sim}$  is normally set considering the complexity (memory required for meshing the geometry) of the simulating geometry and computational power of the PC or cluster (RAM and no. of processing cores) available. For the PhC cavity structure the simulation time was set to 30 pico seconds. As the FWHM of the resonance peak in the spectrum is limited by the time of simulation,  $T_{sim}$ , and the FWHM is inversely proportional to  $T_{sim}$ , in this case, we can not directly calculate Q from the frequency spectrum using Eq. 6.1. So, for very high Q cavities the simulation should be done for very long time ( $\gg 30$  ps) which is not reasonable for taking long time simulating a single cavity even with clustered computers. Instead, the quality factor should be determined by the slope of the envelope of the decaying signal using the formula [32] :

$$Q = \frac{-2\pi f_r \log_{10}(e)}{2m} \quad (6.2)$$

where  $f_r$  is the resonant frequency of the mode, and  $m$  is the slope of the electromagnetic fields' decay.

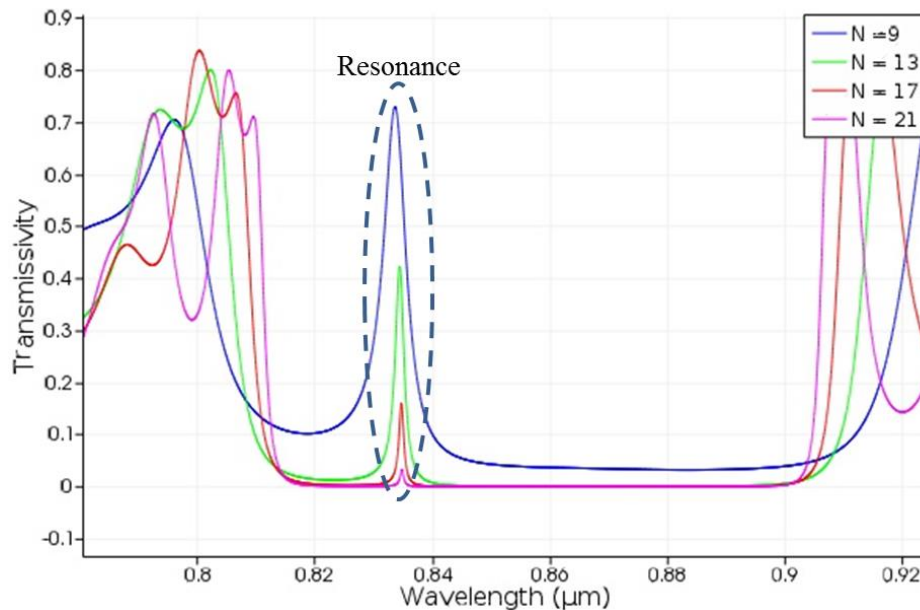
But, when multiple resonant modes are sustained in the cavity, they would interfere with each other in the time domain. The interference of multiple modes made it hard to estimate the decay rate accurately. So, each resonance peak in the frequency domain was isolated using a Gaussian filter, and then the inverse Fourier transform was used to calculate the time decay separately for each peak. The slope of the time decay was then used to calculate the Q factor using Eqn. (6.2). In addition, few point monitors were added in the

simulation at different locations inside the cavity to avoid the chance of having a monitor placed at a node in the mode profile of a cavity mode capturing a weak signal.

### 6.2.2 Effect of Bragg mirror strength on Q-factor

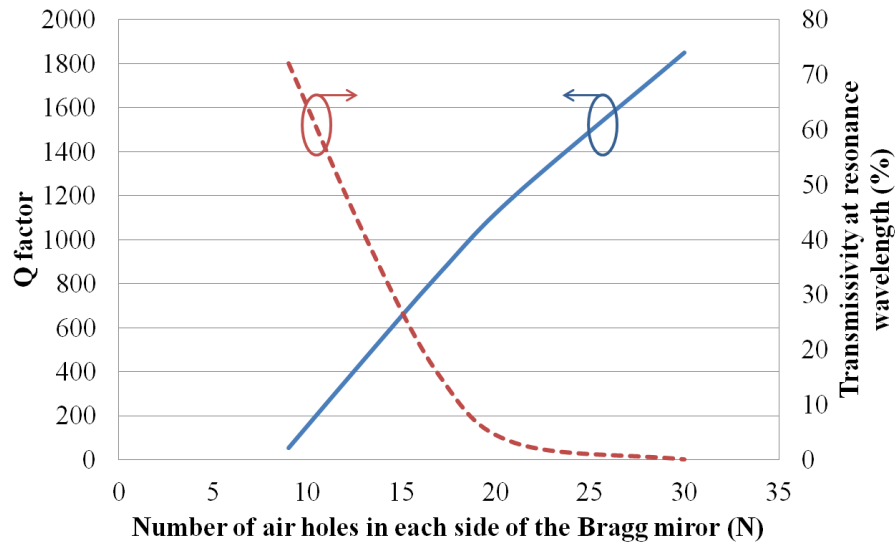
To know the effect of Bragg mirror reflectance on the Q-factor and transmittance of the resonant wavelength, the mirror strength is increased by varying the number of air holes in each side (N) from 7 to 30. In this case, the tapered air hole number ( $N_t$ ) is set to 3 to decrease the time of the simulation.

Figure 6.2-4 shows the transmission spectra of the nano-ribbon cavity with varying number of air holes in the Bragg mirror. Except the resonance there is a bandgap of ~90 nm extending from 815 nm to 905 nm of wavelength as shown in Figure 6.2-4. The FWHM of the resonance decreases (Figure 6.2-4) and consequently Q-factor increases (Figure 6.2-5) with increase in N, but the transmissivity at the resonance wavelength drops down significantly at the same time. So, there is a tradeoff in between the Q-factor and the transmissivity of the nano-ribbon.



**Figure 6.2-4** Transmission spectra of the resonant nano-ribbon waveguide for different number (N) of air holes in the Bragg mirror. At resonance the transmissivity decreases with the increase in air hole number.

Figure 6.2-5 shows that the Q-factor increases almost linearly with the increase in number of air holes in the Bragg mirror. There is a kink in the Q-factor curve at around  $N = 20$  which tells that after achieving a certain strength of the mirror the impact of mirror strength on Q-factor decreases. On the other hand, the transmissivity of the resonant wavelength decreases sharply with increase in mirror strength upto the kinking ( $N = 20$ ) and then decreases at a slow rate. Further improvement of the transmissivity can be envisaged by considering the Bragg mirror tapered at both ends.

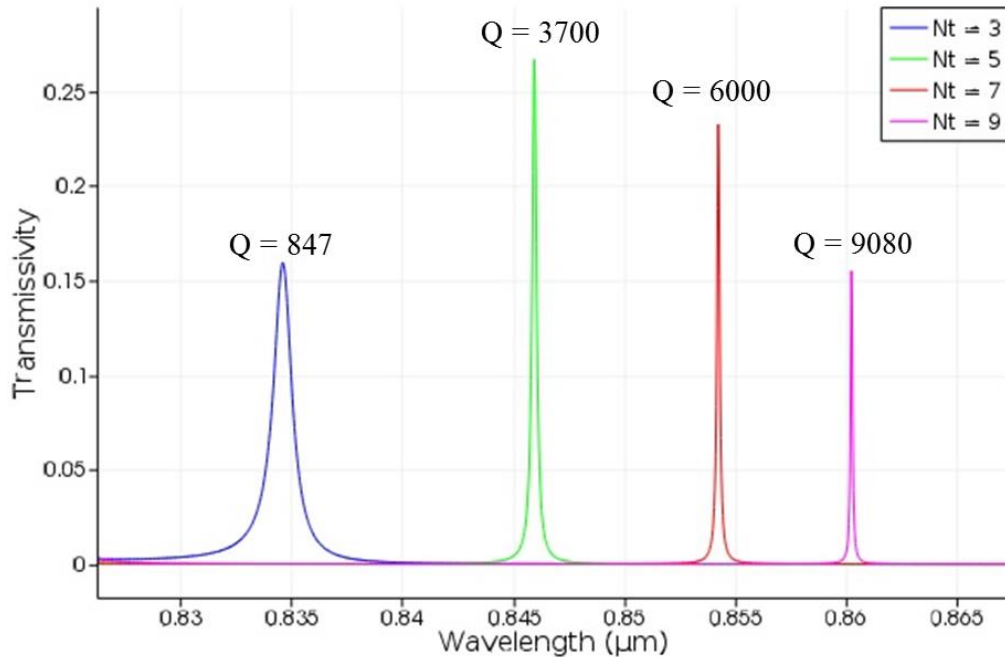


**Figure 6.2-5 Q-factor and transmissivity vs number of air holes (N) in Bragg mirror. Q-factor increases but the transmissivity decreases with increase in Bragg mirror strength.**

### 6.2.3 Effect of cavity length on the Q-factor

The total cavity length for the resonant mode is the summation of the length of separation in between the two Bragg mirrors and the penetration depth of the resonant mode inside the mirror at both sides. So, the cavity length can simply be increased by increasing the number of tapered air holes ( $N_t$ ) in the cavity. To have a reasonable transmissivity the number of air holes in the Bragg mirror (N) is set to 17 in this case. As shown in Figure 6.2-6, the resonance gets sharper and Q-factor increases when the  $N_t$  is varied from 3 to 9. While the increased cavity length increases the Q-factor, the mode volume of the resonance is also increased at the same time which is not desired for bio-sensing application with smaller analyte solutions.

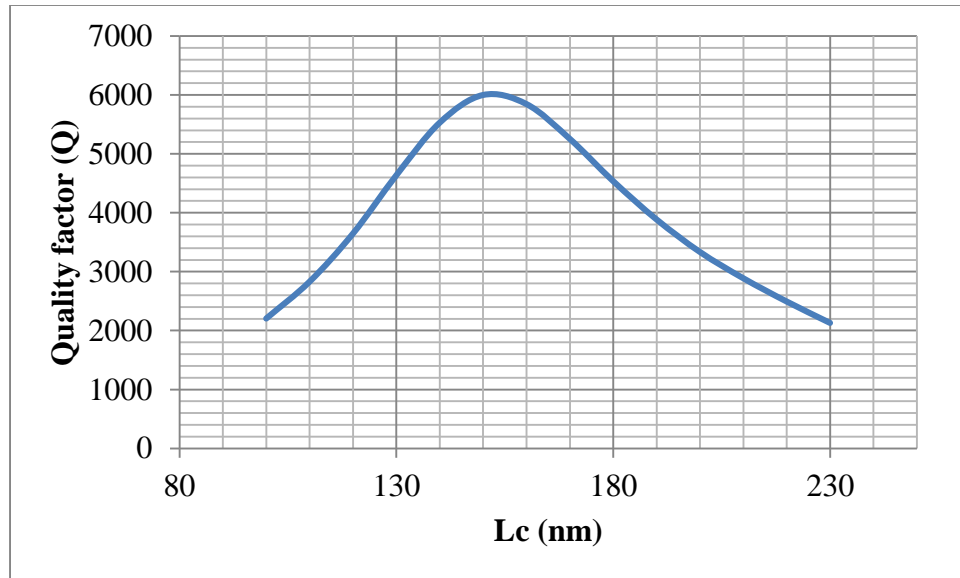




**Figure 6.2-6** Resonance spectra of the nano-ribbon cavity for different number of air holes in the tapered mirror ( $N_t$ ) inside the cavity. The Q-factor increases with cavity length ( $\propto N_t$ ).

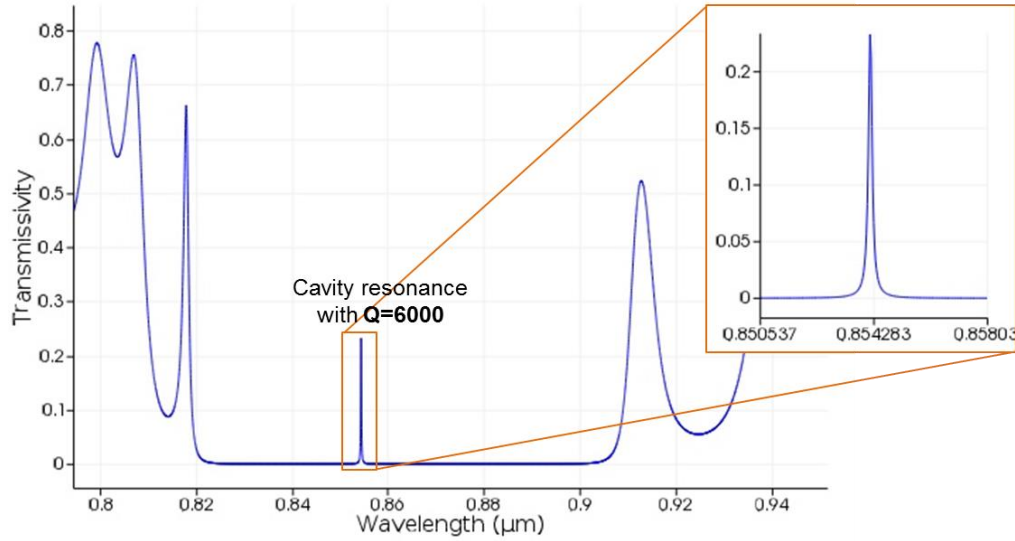
#### 6.2.4 Effect of $L_c$ on Q-factor

Figure 6.2-7 plots the simulation results of the Q-factor value when the separation in between the two smallest air holes ( $L_c$ ) at the center of the cavity (Figure 6.2-2) is varied in the range from 100 nm to 230 nm while keeping  $N = 17$  and  $N_t = 7$ . As we can infer from this data is that the maximum evaluated Q-factor was equal to 6000 for a cavity length  $L_c = 150$  nm,  $N = 17$  and  $N_t = 7$ . The Q-factor can further be improved by increasing  $N$  and  $N_t$  but then the transmissivity and the mode volume would be traded-off. It is worth mentioning that while  $L_c$  was varied, the resonant wavelength experienced a slight red-shift but falls within the range (840-850 nm) of our interest.



**Figure 6.2-7** Quality factor as a function of the central separation length  $L_c$  for the nano-ribbon cavity characterized by the period = 260 nm, hole diameter = 220 nm (max) ~ 130 nm (min).

Trading off the effect of Bragg mirror strength, cavity length and central air hole separation ( $L_c$ ) on the Q-factor and transmissivity, the reasonable parameters of the PhC nano-ribbon cavity selected for the bio-sensor were  $N = 17$ ,  $N_t = 7$ , and  $L_c = 150$  nm. The transmission spectrum showed a Q of ~ 6000 for the resonance peak at 854 nm wavelength in Figure 6.2-8.



**Figure 6.2-8** Transmission spectrum of the designed PhC nano-ribbon cavity with  $N = 17$ ,  $N_t = 7$  and  $L_c = 150$  nm.

Figure 6.2-9a&b shows the refractive index and resonant E-field distribution of the cavity ( $\lambda_{\text{res}} = 854$  nm) respectively and Figure 6.2-9c shows the value of the E-field along the dotted line shown in Figure 6.2-9b. The E-field decreases in a Gaussian pattern and the cavity length is around  $\sim 8\mu\text{m}$  as shown in Figure 6.2-9c.

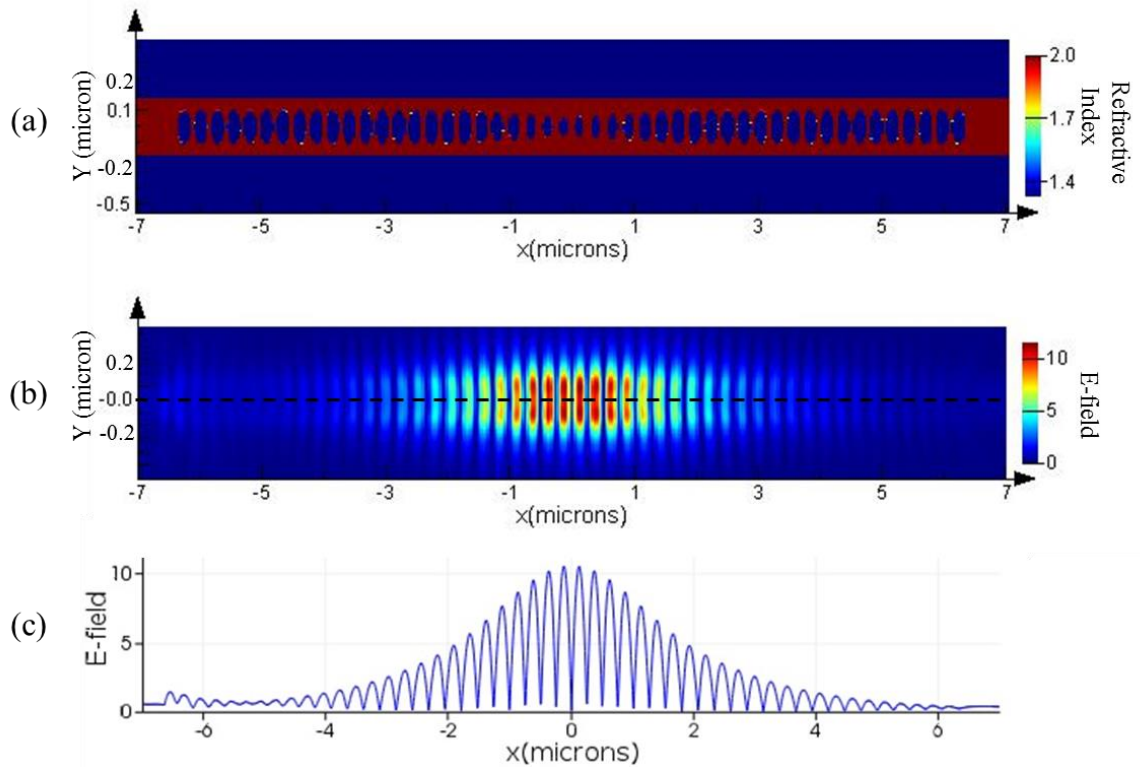


**Figure 6.2-9 (a) Refractive index distribution of the tapered nano-ribbon cavity, (b) E-field distribution obtained from FDTD simulation, and (c) E-field value along the dashed line in (b).**

### 6.2.5 Bulk and surface sensitivity of the designed nano-ribbon cavity

Bulk sensitivity refers to the sensitivity of the nano-ribbon sensor to the change in refractive index (RI) of the bulk media surrounding the cavity region. The FDTD simulation result in Figure 6.2-10a shows that if the surrounding media of the sensor is changed from a Buffer solution (RI = 1.33) to isopropanol (IPA with RI = 1.378), the resonant mode interact with the change in RI and correspondingly, the resonance wavelength red-shifts by 8 nm (from 854 nm to 862 nm) which determines the bulk sensitivity of the sensor as 175 nm/RIU. Whereas, surface sensitivity corresponds to the shift in the resonance wavelength because of a thin layer of biomolecular (RI~1.45) attachment on the surface of the sensor waveguide and at the sidewall of the air holes. The simulation result in Figure 6.2-10b shows that for an attachment of 20 nm (~7nm of

Antibody + 13 nm of Antigen) thin bio-molecular layer of RI=1.45 on the sensor surface shifts the resonance wavelength from 854 nm to 858.6 nm i.e. 0.23 nm shift per nanometer of biomolecule attachment.

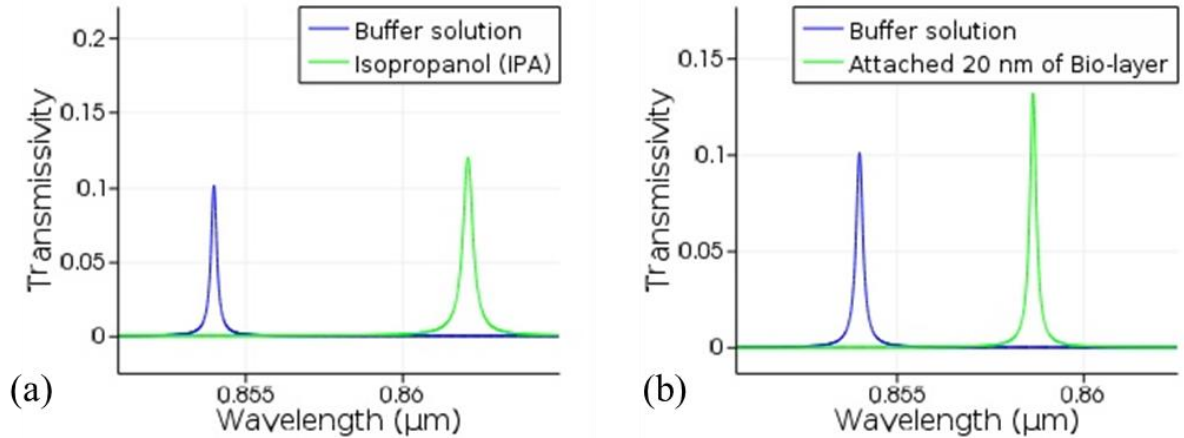


**Figure 6.2-10 Shift in resonance wavelength (a) when the background changes from buffer solution (RI=1.33) to isopropanol (RI=1.378). Resonant shift of about 8nm corresponds to bulk sensitivity of 175 nm/RIU, (b) when 20 nm thin layer of bio-molecule (RI=1.45) is attached on the surface.**

### 6.3 Design of the Grating coupler

It is always challenging to couple light into submicron sized photonic circuit from the comparatively larger (few orders of magnitude) single mode fiber (SMF). At the wavelength of 850 nm, the small size of single mode silicon nitride ( $\text{Si}_x\text{N}_y$ ) waveguide compared with the diameter of a single mode fiber makes coupling inefficient. The  $\text{Si}_x\text{N}_y$  waveguide is extremely small, with a core cross sectional area of approximately less than  $0.12 \mu\text{m}^2$ , which correspond to core height and width around  $0.4 \mu\text{m}$  and  $0.3 \mu\text{m}$  respectively. On the other hand, a single mode optical fiber at the wavelength of 850 nm has a core with a cross sectional area of around  $80 \mu\text{m}^2$  (with a radius of 3-5  $\mu\text{m}$ ), which is ~650 times larger.

Though there are several solutions of this problem, normally they are usually of two types: horizontal edge coupling using tapered waveguide [148] and vertical coupling using grating coupler (GC) [149, 150]. There are both advantage and disadvantages for both of these approaches.

The GC devices take advantage of the Bragg diffraction phenomenon to couple the light from a fiber to the submicron photonic waveguide [151]. GCs enable efficient coupling from optical fibers to photonic waveguide without the need of using lenses or precise inverted tapers. They also avoid expensive methods such as end-polishing and routing the waveguide upto the edge of the chip, and also allows vertical in/out from any place of the chip with smaller footprint. So, 1D grating coupler is preferable in our case for its comparatively smaller footprint ( $\sim 20 \mu\text{m} \times 30\mu\text{m}$ ), vertical coupling, and simplicity in characterization. Though the GC device structure is simple but it requires a well developed consistent fabrication facilities for providing precise and reproducible period and etching depth dimensions as the GC is very sensitivity to those parameters. Back reflection from GC to fiber is also needed to be taken care in a polarization sensitive GC characterization setup.

Figure 6.3-1 shows the schematic of the coupling scheme. These kinds of structures have the advantage of coupling light from standard, non-lensed single mode fibers.

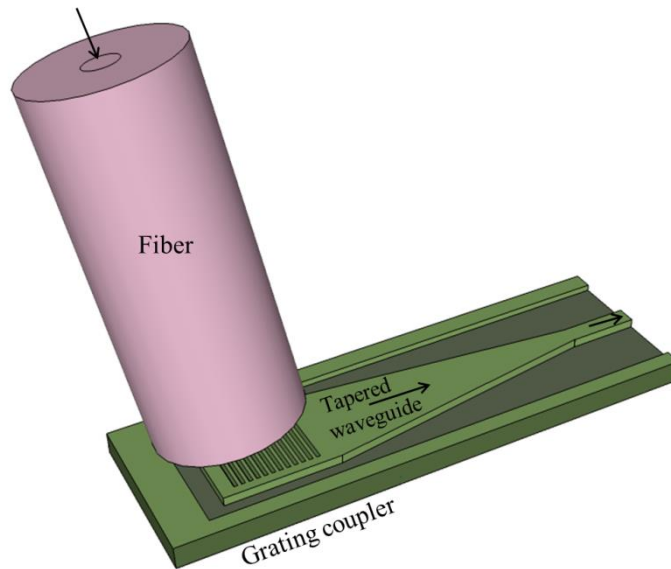


**Figure 6.3-1 Schematic of the coupling scheme from fiber to the waveguide based on grating principle.**

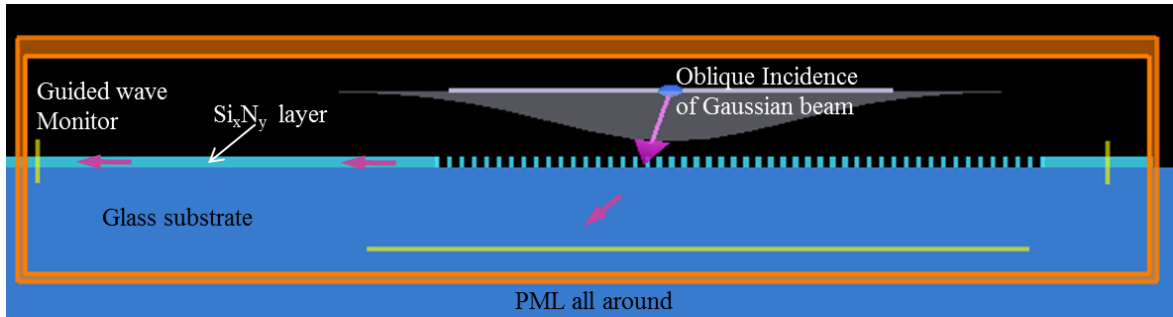


**Figure 6.3-2 FDTD simulation setup for the grating coupler design.**

The simulations and parameters optimization are done by Finite Difference Time Domain (FDTD) simulator, Lumerical FDTD Inc. [12]. The simulation setup is shown in Figure 6.3-2 where the simulation region is surrounded by perfectly matched layer (PML) and the Gaussian beam of TE polarized (E-field parallel to the grating line) light is incident upon the grating at an oblique angle. The grating coupler is made from a  $\text{Si}_x\text{N}_y$  grating on top of Glass substrate. Power monitors are placed in simulation for measuring the guided wave and the diffracted light transmitting through the substrate (Figure 6.3-2).

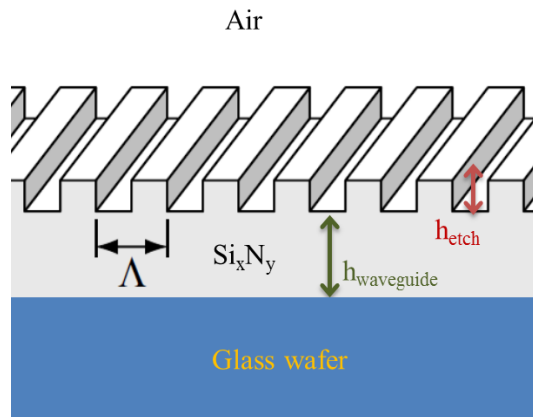


**Figure 6.3-3 Schematic of the  $\text{Si}_x\text{N}_y$  grating coupler on glass wafer where  $\Lambda$  denotes the period,  $h_{\text{waveguide}}$  is the  $\text{Si}_x\text{N}_y$  waveguide thickness, and  $h_{\text{etch}}$  is the etching depth of the grating.**

The schematic of the grating coupler as shown in Figure 6.3-3 points out the parameters which are varied to maximize the efficiency of the coupler at the desired wavelength. Particle Swarm Optimization (PSO) [39, 92, 152], a population based stochastic optimization technique, inspired by the social behaviour of flocks of birds or schools of

fish, is used to optimize the efficiency of the grating coupler. The optimized parameters are listed in Table 6.3-1.

**Table 6.3-1** Optimized parameters for the  $\text{Si}_x\text{N}_y$  grating coupler on glass substrate.

Parameter	Value for $\text{Si}_3\text{N}_4$ grating coupler
Grating period ( $\Lambda$ )	590nm
Etching depth ( $h_{\text{etch}}$ )	250nm
Filling factor (FF)	50%
Incident angle of the wave ( $\theta$ )	10 degree
Number of period (N)	50
Waveguide width ( $h_{\text{waveguide}}$ )	400 nm
Efficiency	<b>36.9%</b>
1dB Bandwidth	20nm

The coupling efficiency of the optimized grating coupler vs wavelength for both TE (E-field parallel to the grating line) and TM (E-field perpendicular to the grating line) is plotted in Figure 6.3-4 which shows the maximum coupling efficiency of 36.9% for TE polarized light at the wavelength of 846 nm with 1dB bandwidth of 20 nm easily overlapping with the resonance wavelength of the designed nano-ribbon cavity (Figure 6.2-8). For TM polarized light the maximum coupling efficiency is 23% at the wavelength of 785 nm with 1dB bandwidth of 22 nm.



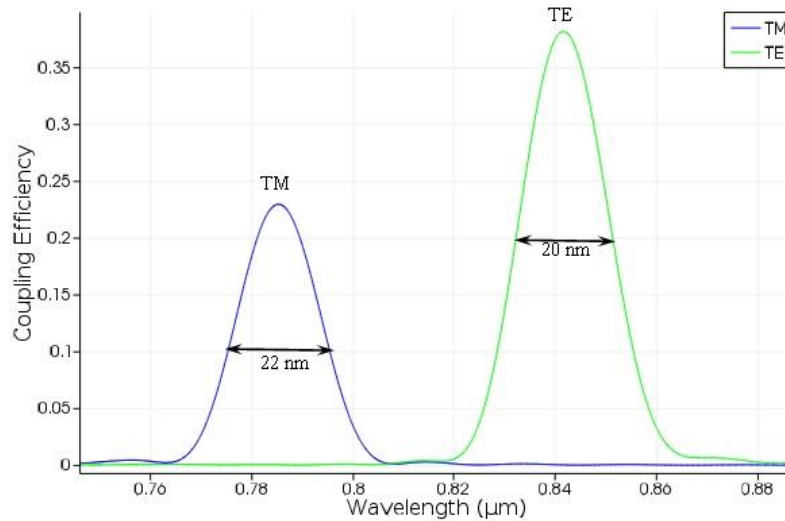


**Figure 6.3-4** Optimized grating coupler's (Table 6.3-1) coupling efficiency vs wavelength for both TE and TM polarized light.

## 6.4 Fabrication of Nano-ribbon cavity and grating couplers

The photonic crystal nano-ribbon cavity fabrication was done using nano-imprinting technique jointly with VTT (Finland). The whole nano-ribbon was designed as an 8 mm long and 30 μm wide (at the beginning) waveguide which was tapered into a width of only 300 nm at the center. Both ends of the waveguide had grating couplers and in the middle of the waveguide it had the PhC cavity as indicated in Figure 6.4-1. There was a line of air holes of different diameters in the middle of the nano-ribbon including the tapered line of air holes (placed front to front at the center) acting as a partial mirror for the incoming light and formed an optical cavity. The fabrication was done following the process steps described in Chapter 3.

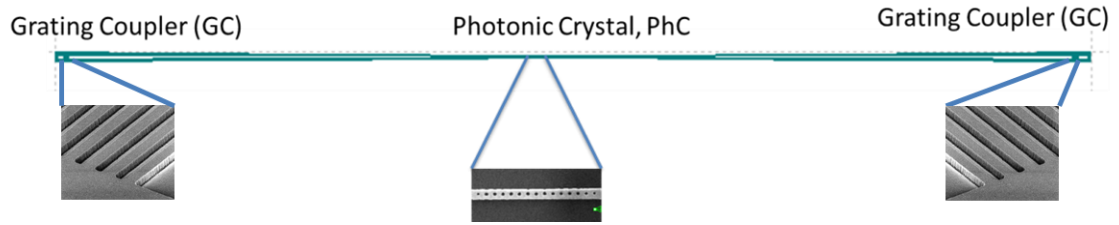


**Figure 6.4-1** Schematic of the nano-ribbon cavity with in and out grating coupler.

## 6.4.1 Investigation of the pattern transfer during the nano-imprint steps

### 6.4.1.1 PhC cavity air holes

The middle part of the nano-ribbon waveguide contains very small air holes ( $\sim 60$  nm in radius) which are challenging to fabricate by the nano-imprint. In addition, the diameter of the holes was varied from 120 nm to 220 nm to form a line of tapered holes. Figure 6.4-2 presents SEM pictures of holes in the waveguide. Numbers above the waveguide refer to air-hole identifier (ID). Figure 6.4-2a is from *master* stamp, Figure 6.4-2b is from *Ormostamp* copy and Figure 6.4-2c is from resist imprinted with *Ormostamp* copy (Section 3.4 and Figure 3.4.1 for the nano-imprint process steps). As can be seen in Figure 6.4-2a the hole depth of the smallest holes (ID-42) was shallower than that of the bigger ones (ID-17 or less). Only holes bigger than  $\sim 200$ nm (ID upto 29) had reached the etching depth. Besides, the side walls were slanted and rough. Some side walls of widest holes were etched through in sideways (ID 17, 18, 21 in Figure 6.4-2a).

The intermediate stamp (Figure 6.4-2b) was a mirror image from the *master* (Figure 6.4-2a). Features which could be seen in the master should be also visible inversely in the *Ormostamp* copy. But, the intermediate stamp (*Ormostamp* copy) taken from *master* contains less pattern details (Pillar missing at the center) than the *master* stamp, most probably, because of the shallower etching depth at the center of the *master*. The pattern details were copied well from the intermediate *master* to the resist layer (Figure 6.4-2c).

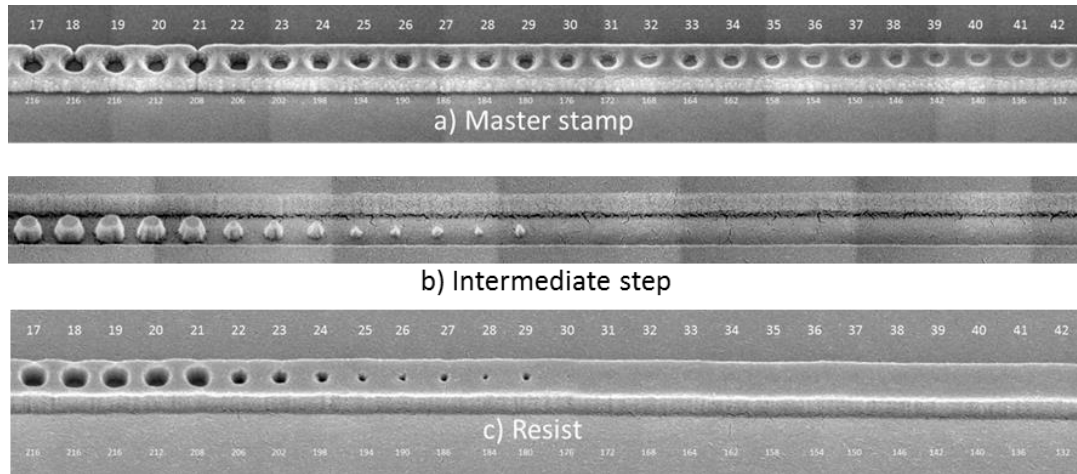


**Figure 6.4-2 SEM images of nano-ribbon cavity on a) *master stamp*, b) *intermediate stamp* and c) *patterned resist*.**

The realized diameter of the holes in the *master* (done by EBL) as shown in Figure 6.4-3 was smaller than targeted. The realized diameter was only 100 nm in the bottom of the hole though the targeted diameter was  $\sim 220$  nm. This is due to the conical shape of holes as can be seen in Figure 6.4-2b and Figure 6.4-3b. Apparently, during the EBL process, the e-beam resist of the smallest holes were not fully exposed and the etchant could not reach the Si during etching. Besides, the roughness of the etched side-walls were also too high.

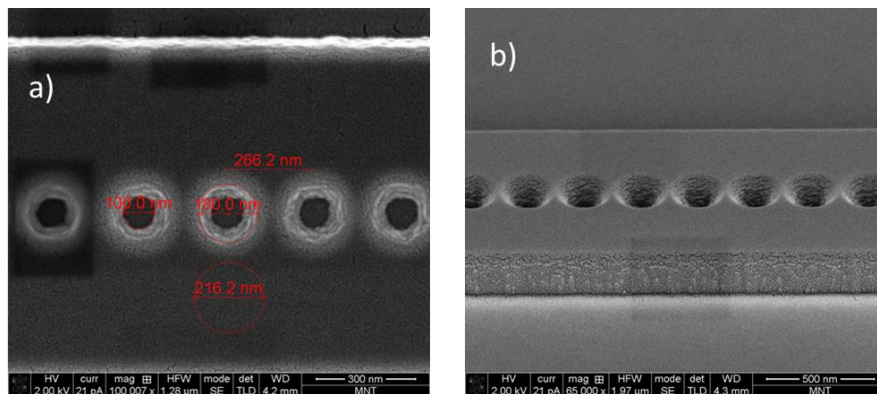


**Figure 6.4-3 SEM image of the holes in the nano-ribbon cavity from *master stamp*: (a) top view and (b) tilted side view. The targeted diameter was  $\sim 220$  nm.**

### 6.4.1.2 Grating coupler

Both ends of the nano-ribbon waveguide contained similar in and out coupling gratings. Figure 6.4-4 shows SEM images of the grating on the resist layer. The upper image was the top view of the grating and the lower was of the FIB milled cross section. Both images were adjusted to maintain the same magnification and aligned with each other. As can be seen from the cross-section that the side walls were slanted. Slanted side walls originated from the *master* as can also be seen later in Figure 6.4-5. The width of the groove was ~210 nm at the bottom and ~350 nm on top.

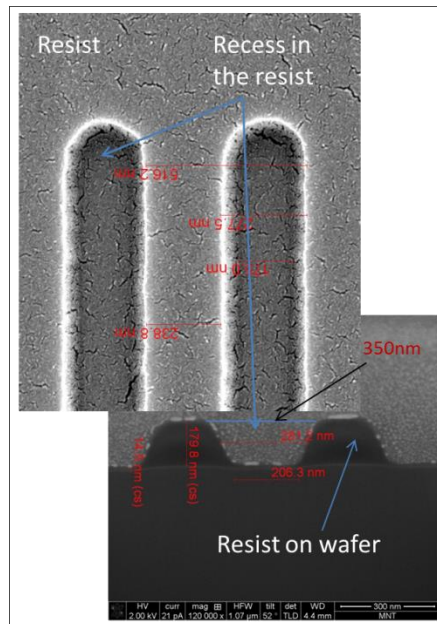


**Figure 6.4-4 SEM images from the coupling grating. Upper image is taken from the top and lower one is the FIB milled cross section.**

Slanted side walls in the resist layer were problematic and so, investigated further. Figure 6.4-5 presents a comparison of the *master* and the *Ormostamp* copy (intermediate stamp). Both images are adjusted to have the same magnification. Images were cross sections of the coupling grating. The origin of the slanted shape was in the *master* stamp as can be seen from Figure 6.4-5.

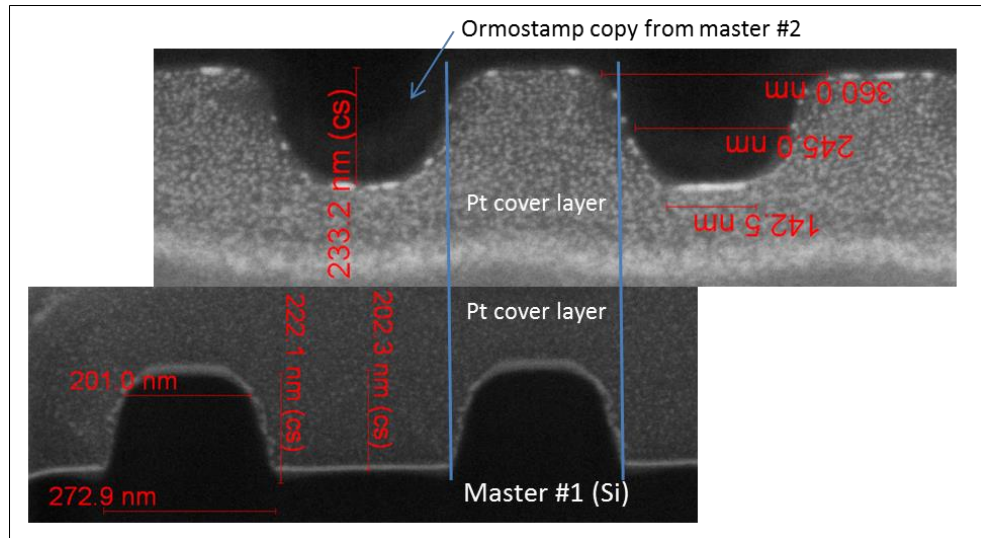


**Figure 6.4-5 SEM pictures of the FIB milled cross sections of the *master* (below) and *Ormostamp* copy of *master* (top).**

### 6.4.2 Pattern transfer from nano-imprinted resist to $\text{Si}_x\text{N}_y$

The nano-imprinted wafers were then processed. The wafers had patterns imprinted in the resist layer on top of Cr and  $\text{Si}_x\text{N}_y$  layer on glass substrate. First, the Cr was etched for 3 min (see in Chapter 3) and then the pattern was transferred from the Cr to the  $\text{Si}_x\text{N}_y$  layer using another ICP etching recipe as previously shown in Section 3.6. The wafers were then diced into individual chips and inspected in the SEM.

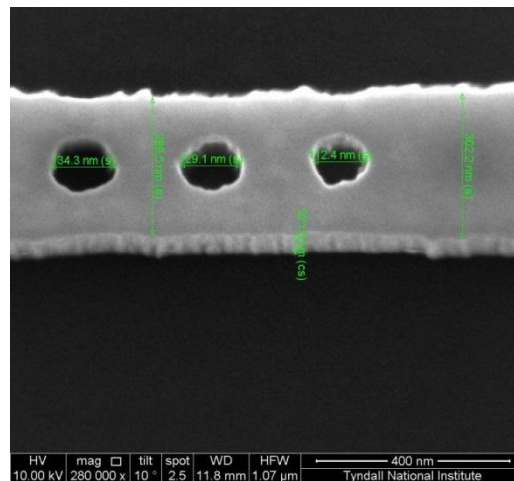


**Figure 6.4-6 SEM image of part of a fully processed photonic crystal nano-ribbon cavity fabricated by nano-imprint technology.**

The photonic crystal air holes in the nano-ribbon cavities came out after pattern transfer, though there were some missing air holes at the center of the cavity. There was also a mismatch between the dimensions of the designed and the fabricated air holes. Also, the edge roughness was pretty high. These features originate mainly from the nano-imprint Si master itself as shown in Section 6.4.1.1.

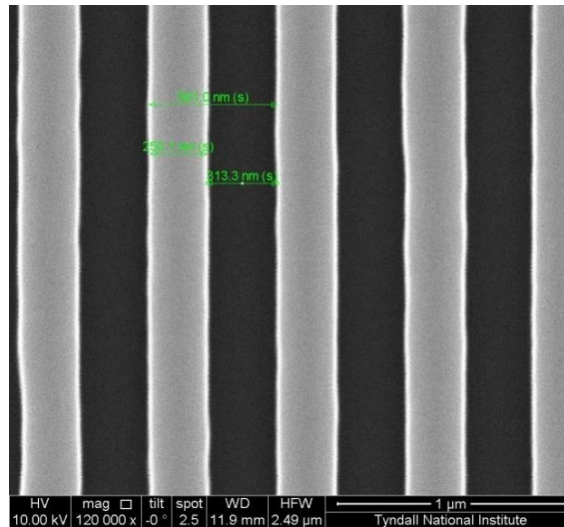


**Figure 6.4-7 SEM image of a portion of the grating coupler after pattern transfer.**

Similarly, in Figure 6.4-7, a portion of a fully processed grating coupler showed groove width of ~310nm, period of ~570 nm. There was a mismatch between the designed feature size and the values got from the SEM inspection as shown in Table 7.1. It was hard to define clearly how big additional effect came from the imprinting and the etching steps, since the side walls were so slanted that they did not define the etching area precisely.

Table 7.1 Contrast between the designed and the fabricated grating coupler using nano-imprint.

Grating coupler	Design	SEM
Period	590 nm	570 nm on average
FF	35.7%	<b>42.7% on average</b>

## 6.5 Summary

The composition of the 1D PhC nano-ribbon cavity was studied and tapered mirror was included in the cavity to increase the Q-factor. The effect of the Bragg mirror reflectance, cavity length and central smallest air hole separation on the Q-factor was examined. The trade-off among the Q-factor, transmissivity and mode volume determines the parameters of the nano-ribbon cavity. Bragg mirror tapered at both ends may also be considered for further improvement of both Q-factor and transmissivity. The grating coupler's parameters were optimized using PO optimization algorithm.

The designed device was fabricated by nano-imprint lithography in wafer-scale. Different sized components (from mm to 100 nm) on the same wafer made the nano-imprinting quite challenging to optimize the imprinting process to get the precise dimensions in accordance with the design. However, the SEM data was used to model the fabricated grating coupler in the simulator. It was found that the discrepancy in the period, filling fraction and the etching depth of the designed and nano-imprinted GC deviated the coupling efficiency quite a lot that it fell beyond the designed cavity resonance wavelength. Moreover, the nano-ribbon cavity holes did not come out properly in the first run of the nano-imprinting to sustain any resonance. Sidewall roughness specifically for nano-structure of size  $< 200$  nm, is also an issue to improve by optimizing the patterning and etching recipe. Figuring out the specific sources of deviation in the nano-imprinting processes was an important achievement for the future wafer-scale nano-imprinting process development.

## References

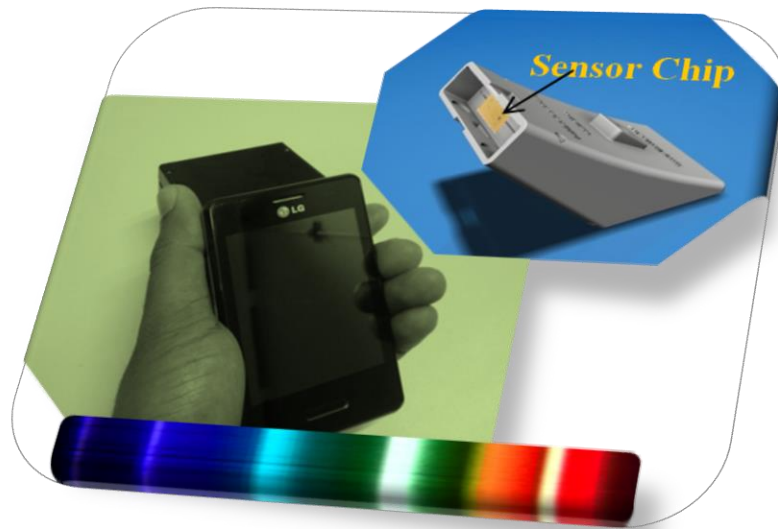
- [1] G. C. M. Grande, V. Petruzzelli, and A. D'Orazio "High-Q photonic crystal nanobeam cavity based on a silicon nitride membrane incorporating fabrication imperfections and a low-index material layer," *Progress In Electromagnetics Research B*, vol. 37, pp. 191-204, 2012.
- [2] Q. M. Quan, P. B. Deotare, and M. Loncar, "Photonic crystal nanobeam cavity strongly coupled to the feeding waveguide," *Applied Physics Letters*, vol. 96, May 17 2010.
- [3] Q. M. Quan and M. Loncar, "Deterministic design of wavelength scale, ultra-high Q photonic crystal nanobeam cavities," *Optics Express*, vol. 19, pp. 18529-18542, Sep 12 2011.
- [4] C. Schriever, C. Bohley, and J. Schilling, "Designing the quality factor of infiltrated photonic wire slot microcavities," *Optics Express*, vol. 18, pp. 25217-25224, Nov 22 2010.
- [5] E. Chow, A. Grot, L. W. Mirkarimi, M. Sigalas, and G. Girolami, "Ultracompact biochemical sensor built with two-dimensional photonic crystal microcavity," *Optics Letters*, vol. 29, pp. 1093-1095, May 15 2004.
- [6] M. Lee and P. M. Fauchet, "Two-dimensional silicon photonic crystal based biosensing platform for protein detection," *Optics Express*, vol. 15, pp. 4530-4535, Apr 16 2007.
- [7] F. Liang, N. Clarke, P. Patel, M. Loncar, and Q. M. Quan, "Scalable photonic crystal chips for high sensitivity protein detection," *Optics Express*, vol. 21, pp. 32306-32312, Dec 30 2013.
- [8] G. Shambat, S. R. Kothapalli, J. Provine, T. Sarmiento, J. Harris, S. S. Gambhir, *et al.*, "Single-Cell Photonic Nanocavity Probes," *Nano Letters*, vol. 13, pp. 4999-5005, Nov 2013.
- [9] M. Eichenfield, J. Chan, R. M. Camacho, K. J. Vahala, and O. Painter, "Optomechanical crystals," *Nature*, vol. 462, pp. 78-82, Nov 5 2009.
- [10] D. G. Grier, "A revolution in optical manipulation," *Nature*, vol. 424, pp. 810-816, Aug 14 2003.
- [11] D. Psaltis, S. R. Quake, and C. H. Yang, "Developing optofluidic technology through the fusion of microfluidics and optics," *Nature*, vol. 442, pp. 381-386, Jul 27 2006.
- [12] P. Lalanne, C. Sauvan, and J. P. Hugonin, "Photon confinement in photonic crystal nanocavities," *Laser & Photonics Reviews*, vol. 2, pp. 514-526, Dec 2008.
- [13] "Lumerical Solutions, Inc. <http://www.lumerical.com/tcad-products/fdtd/>".
- [14] "Quality factor calculations". Available: [http://docs.lumerical.com/en/diffractive\\_optics\\_cavity\\_q\\_calculation.html](http://docs.lumerical.com/en/diffractive_optics_cavity_q_calculation.html)



- [15] M. H. Pu, L. Liu, H. Y. Ou, K. Yvind, and J. M. Hvam, "Ultra-low-loss inverted taper coupler for silicon-on-insulator ridge waveguide," *Optics Communications*, vol. 283, pp. 3678-3682, Oct 1 2010.
- [16] D. Vermeulen, S. Selvaraja, P. Verheyen, G. Lepage, W. Bogaerts, P. Absil, *et al.*, "High-efficiency fiber-to-chip grating couplers realized using an advanced CMOS-compatible Silicon-On-Insulator platform," *Optics Express*, vol. 18, pp. 18278-18283, Aug 16 2010.
- [17] R. Topley, L. O'Faolain, D. J. Thomson, F. Y. Gardes, G. Z. Mashanovich, and G. T. Reed, "Planar surface implanted diffractive grating couplers in SOI," *Optics Express*, vol. 22, pp. 1077-1084, Jan 13 2014.
- [18] C. R. Doerr, L. Chen, Y. K. Chen, and L. L. Buhl, "Wide Bandwidth Silicon Nitride Grating Coupler," *Ieee Photonics Technology Letters*, vol. 22, pp. 1461-1463, Oct 1 2010.
- [19] "Particle Swarm Optimization". Available:  
[http://docs.lumerical.com/en/sweeps\\_optimization\\_particle\\_swarm.html](http://docs.lumerical.com/en/sweeps_optimization_particle_swarm.html)
- [20] J. Robinson and Y. Rahmat-Samii, "Particle swarm optimization in electromagnetics," *Ieee Transactions on Antennas and Propagation*, vol. 52, pp. 397-407, Feb 2004.
- [21] J. Pond and M. Kawano, "Virtual prototyping and optimization of novel solar cell designs," *Photonics North 2010*, vol. 7750, 2010.

# Chapter 7

## Conclusions and Further Development



The purpose of this thesis was to investigate a low cost, easy to characterize, compact and high throughput (multiplexed) optical biosensor compatible with wafer scale batch production. The developed sensor should decouple the bulk and surface sensitivity, necessary for detecting small amount of analyte in the presence of thermal or other perturbations. The sensor had to operate in the visible and near infrared (~850 nm) wavelengths and so, was developed preferably with Silicon nitride ( $\text{Si}_x\text{N}_y$ ) material on glass substrate which facilitated back illumination allowing the front side to be used with micro-fluidics. To lower down the cost of the sensor, wafer scale nano-imprint fabrication technology was also tried. To fulfill these requirements two different types of optical sensing technology: resonant waveguide grating (RWG) and photonic crystal (PhC) nano-ribbon cavity were investigated.

## 7.1 Summary and Conclusions

The physical basis of operation of RWG sensor was investigated by a customized Finite difference time domain (FDTD) model interfaced with MATLAB. Different physical parameters of the RWG like period, filling fraction, etching depth, and waveguide thickness were studied to understand the relationship between these physical design parameters and sensor sensitivities. A simple step by step design procedure was presented for designing RWG at specific wavelength fulfilling the lineshape and linewidth requirements. The sensitivity of the RWG sensor was divided into two types: bulk and surface sensitivities. Surface sensitivity is important for bio-molecular detection because it defines the extent of resonance wavelength shift and so the detection limit for the bio-molecular binding events. Both analytical and numerical studies revealed that the surface sensitivity was mostly dependent on the overlap integral of the resonant mode electric field at the detection region (~20 nm thin region on surface where bio-molecular binding happens). The RWG parameters that affect the overlap integral by effectively changing the E-field distribution are specifically the etching depth, polarization of the light source, and filling fraction. The designed and optimized RWG sensor based on Silicon nitride

(Si<sub>x</sub>N<sub>y</sub>) waveguide material showed a bulk sensitivity of ~180 nm/RIU and surface sensitivity of 0.1 nm shift per nm of bio-molecular attachment.

A wafer scale nano-fabrication technique was presented to fabricate the RWG sensors on glass substrate using either Electron beam lithography (EBL) or nano-imprint lithography (NIL). EBL was used mostly for the RWG development phase (proof of concept) whereas NIL was targeted for low cost wafer scale batch production. Low optical loss Si<sub>x</sub>N<sub>y</sub> waveguide (0.09 cm<sup>-1</sup>) material was developed by PECVD technique. It was found that increasing NH<sub>3</sub> precursor gas concentration and switching the PECVD plasma mode from mixed (high+low) frequency to single (low) frequency improved the surface roughness of the developed material and concomitantly reduced the optical waveguide loss of the material. Chromium (Cr) has been being used for making external hard mask in semiconductor processing industry to photo-pattern micro-structures, but had not been used that much as local hard mask embedded in the nano-fabrication process for making nano-structures. In the proposed nano-fabrication process a thin layer of Cr was used as a local hard mask which not only resolved the charging effect during EBL, but also facilitated making high aspect ratio nano-structure. An aspect ratio of 10 was achieved for ~60nm narrow grating lines which is the highest aspect ratio presented so far in the literature for nano-structure of that small dimension.

The RWG sensors were optically characterized by using custom bench top fiber based reflectance measurement and free space coupling based transmittance measurement setup. The bulk sensitivity of the sensor was found 183 nm/RIU experimentally. Bio-assay experiments were done for both adsorption based and standard EDC coupling based attachment mechanism. Biomolecules e.g., Immunoglobulin-G (IgG) C1q and C3 proteins of different concentration (>0.5µg/ml) were successfully detected in both buffer and serum with selectivity with other proteins.

Waveguide embedded 1D PhC nano-ribbon cavity was also studied as part of this work. Multi-parametric FDTD analyses were done to understand the composition and operational principle of the PhC cavity and more important the relationship between the

physical design parameters and cavity Q-factor to improve the sensor sensitivity. A tapered partial mirror was included in the cavity section to improve the mismatch between the PhC Bloch mode and waveguide cavity mode which improved the Q-factor. By trading-off the Q-factor, transmittance and mode volume a waveguide embedded PhC cavity was designed which had a reasonable Q-factor (~6000), mode volume and transmittance (10-15%). A grating coupler was also designed and included as in and out coupling components. The PhC cavity was fabricated at the wafer scale jointly with VTT (Finland) by using the nano-imprint technology. It was challenging to maintain the different dimensions precisely (from 60 nm in radius air holes to 8 mm long tapered waveguide) of different components in the same wafer run. In the first run of the process, the period and filling fraction of the grating coupler and PhC cavity came out differently than the designed values and so the spectral response of these two components were different. Moreover, some air holes in the cavity were missing which inhibits the fabricated sensor to work properly. However, figuring out the specific sources of deviation in the NIL process steps, resolving the residual layer thickness variation in NIL across the 4 inch diameter wafer, further direction to optimize the NIL process steps to get the desired dimensions would surely help others for the future wafer-scale nano-imprinting process development on glass substrates. In multi dimensional NIL technique, it is important to have the Silicon (Si) master stamp done accurately by EBL otherwise the error will carry on in all steps of the NIL processes as all other stamps are copied from that Si master stamp. Nevertheless, sidewall roughness is also a problem specifically for nano-structure of size  $< 200$  nm, which should be resolved by optimizing the NIL patterning and pattern-transferring etching recipe.

A dual resonance approach was presented for separating the bulk and the surface sensitivity. Distinguishing the sensor responses coming from the bulk and the surface is very important for avoiding false reading in time of detecting very low concentration analytes in an environment where thermal or other perturbations are likely to happen. Commercially available biosensors use expensive and bulky temperature controlling unit and additional reference channels to avoid the noise coming from the bulk solution. In this work, the design procedure of tuning the number of resonance modes of a multi-order,

multi-mode RWG was presented by changing the thickness of the RWG waveguide layer. A dual resonant RWG was designed in such a way that the two resonant modes had distinct electric field distribution so that one could act mostly as a bulk sensor and the other would more likely behave as a surface sensor. Exploiting the different nature of these two co-existing resonances, a new approach to decouple the bulk and surface properties was proposed to avoid the need of bulky temperature controlling unit and additional references. The proposed approach was validated by demonstrating the separation of bulk and surface contribution in a controlled experiment. Though a polarization based separation technique was proposed in SPR technology, the sensitivity ratio of bulk and surface was only 2.5 which was very low to act effectively whereas the presented dual resonance technique showed a sensitivity ratio of 10, 4 times better than the polarization technique. In addition, the combination of multi-resonances with the polarization variation would reveal the new features of bio-molecular binding kinetics.

## **7.2 Future work and directions**

In this thesis, single layer RWG sensor was studied thoroughly, but multi-layer RWG sensor can open the scope of further manipulation of resonant mode E-field to increase the sensitivity and efficiency of dual resonance approach. Inclusion of metal/nanoparticle on the RWG surface for subwavelength plasmonic confinement of electromagnetic field in the detection region seems also promising to study.

Multi-mode, multi-order resonant RWG approach with polarization variation can be studied further to make it a very useful tool for better understanding of bio-molecular interaction in proteomics by revealing additional information about binding kinetics instead of just quantifying the analyte concentration.

### **7.2.1 Smartphone based Bio-detection**

Incorporation of biosensing into smartphone platforms will be a potentially powerful development which would help to facilitate the goal of low-cost home-based tests to diagnose a medical condition. The system would automatically communicate results to a cloud-based monitoring system that would alert the physician when needed.

Label-free RWG based optical bio-sensing with its high sensitivity, low cost and high throughput can be a good candidate for integrating with the smartphone. Design, fabrication and characterization have already been shown in this thesis work. Now, the integration the developed sensor with the smartphone based read-out system and a compact liquid delivery system are needed to be addressed.

Here, I present the early prototype of smartphone based prospective portable bio-sensing platform. A commercially available 3D printed low-cost spectrometer add-on (Public lab store) is adapted to the camera of the smartphone as the wavelength readout system. The developed and already characterized RWG sensor is to be integrated into the smartphone spectrometer for optical reading-out of the resonance spectrum. Small changes in the refractive index of a fluidic media atop the sensor can be monitored in real time using the computation power of the smartphone.

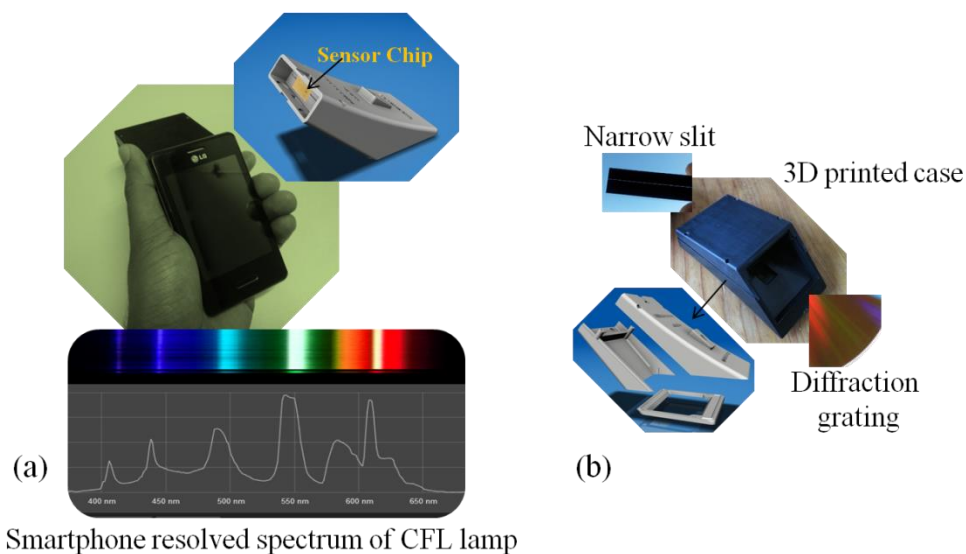


**Figure 7.2-1 Initial prototype of smartphone based optical bio-detection platform. (a) 3D printed add-on is attached to the smartphone camera to make a spectrometer, the spectrum of fluorescent tube is captured using this spectrometer but the resolution was not great (~5 nm), and (b) The commercially available (Public lab store) add-on device is composed of narrow slit, 3D printed plastic case and diffraction grating.**

Smartphone integrated low-cost portable biosensor systems will enable diagnostic technology that can be translated to resource-poor regions of the world for pathogen detection, disease diagnosis, and monitoring of nutritional status. Such a portable system,

deployed widely, would be capable of rapidly monitoring for the presence of environmental contaminants over large areas, or tracking the development of a medical condition throughout a large population.



# Publications

## Journal Articles

- [1] M. N. Hossain, J. Justice, P. Lovera, B. McCarthy, A. O’Riordan, and B. Corbett, "High aspect ratio nano-fabrication of photonic crystal structures on glass wafers using chrome as hard mask," *Nanotechnology*, vol. 25, p. 355301, 2014.  
<http://dx.doi.org/10.1088/0957-4484/25/35/355301>
- [2] M. N. Hossain, J. Justice, P. Lovera, A. O’Riordan, and B. Corbett, "Dual resonance approach to decoupling surface and bulk attributes in photonic crystal biosensor," *Optics Letters*, vol. 39, p. 6213, 2014.  
<http://dx.doi.org/10.1364/OL.39.006213>

## Conferences

- [3] M. N. Hossain, J. Justice, P. Lovera, M. Mitchell, A. Oriordan, and B. Corbett, "Two Color Approach to Separating Surface and Bulk Sensitivity in a Photonic Crystal Biosensor," p. FM4E.5, *Frontiers in Optics*, Florida, USA, 2013.  
<http://dx.doi.org/10.1364/FIO.2013.FM4E.5>
- [4] D. O'Mahony, M. N. Hossain, J. Justice, E. Pelucchi, A. O'Riordan, B. Roycroft, *et al.*, "High index contrast optical platform using gallium phosphide on sapphire: an alternative to SOI?," vol. 8431, p. 84311H, *Proc. SPIE 8431, Silicon Photonics and Photonic Integrated Circuits III*, 2012.  
<http://dx.doi.org/10.1117/12.922687>
- [5] M. N. Hossain, J. Azadi, and Brian Corbett, " Turn your smartphone into optical bio-detection platform & use micro LED arrays for bio-medical applications," *EvolveBiomed Conf.*, Apr. 2015, Dublin, Ireland.